University of Rome - La Sapienza

Physics department

PhD in Accelerator Physics

Machine induced background study and simulation optimization at the SuperKEKB accelerator

Candidate
Antonio Paladino

Supervisors
Prof. Francesco Forti
Prof. Carlos Marinas

Contents

Introduction

Although the initial development of particle Physics exploited natural sources, like cosmic rays and radioactive sources, it is only with particle accelerators that a systematic exploration of fundamental processes at the subatomic scale became possible. A significant breakthrough was achieved in the late 1950s, when the idea of the synchrotron was further developed by Bruno Touschek in Frascati, where he and his collaborators built on Ada, for "Anello di accumulazione", the Italian words for "storage ring". The success of the project and technological progress brought soon to the idea of beams colliding in opposite directions, with the big advantage that the available energy for the interaction in the center of mass scales linearly with energies, so if particles in two beams circulating in opposite directions have the same mass and the same energy E, the available energy in the center of mass would be 2E, whereas the available energy for a fixed target collision only scales with $\sqrt{\mathrm{E}}$.

Experiments at accelerators allowed to study and develop the Standard Model of fundamental interactions, which on one hand is the model that better describes our universe, but on the other hand cannot explain many other observations. For instance, the source of matter-antimatter asymmetry, or the origin of what are called dark matter and dark energy, that constitutes 95% of the total energy of the universe, cannot be explained in the Standard Model. To find hints of what is called New Physics, high energy Physics experiments at colliders took two different paths, the so called "*Energy frontier*" and "*Intensity frontier*". At the Energy frontier, accelerators like the Tevatron or the Large Hadron Collider are designed with beam energies as high as possible, to increase the available energy in the center of mass. At the Intensity frontier, New Physics is explored with accelerators that work at lower energies but that are able to provide a huge number of events to observe extremely rare processes in the decay of B and D mesons or τ leptons, or very subtle effects in the time dependence of more abundant decays.

Until 1964 it was known that weak interactions could violate separately parity (P), the transformation that flips the sign of the spatial coordinates, and charge conjugation (C), the transformation that swaps a particle with its anti-particle, but it was assumed that they were invariant under the application of both transformations, that is a CP transformation. In 1964 James Cronin and Val Fitch observed for the

first time, at Brookhaven National Laboratories, the violation of CP symmetry in the decay of K mesons. It was only in 1973 that Kobayashi and Maskawa were able to include the explanation of CP violation in the Standard Model, extending to three generations of quarks the previous theory by Cabibbo that was developed only with two generations of quarks.

In the 1980s it became clear that time dependent CP violation could be observed in $B^0 - \overline{B}^0$ system, provided that higher samples of B mesons would have been available. For this reason, the B-factories PEP-II at SLAC and KEKB at KEK were built, becoming the most important examples of accelerators exploring the Intensity frontier. CP violation in B meson decays was finally discovered in 2001 by the experiments BaBar and Belle, operating at SLAC and KEK respectively.

Already in 2004 the idea of an upgrade of KEKB to a machine with an even higher instantaneous luminosity started to be developed, and culminated in 2019 with the start of operations of SuperKEKB and the Belle II detector. One big challenge for such a high luminosity collider is machine induced backgrounds, so it is necessary to study all possible countermeasures to reduce them, including beam collimators. Collimators are sophisticated, costly and relatively big elements of the lattice, so their number and their position in the ring must be carefully evaluated. Simulations can be used to predict their effects and their optimal apertures. This work stems from the need to study how machine induced backgrounds can be mitigated by collimators, how much collimator apertures can be optimized, and how many collimators could/should be installed to effectively reduce backgrounds.

In this work, an introduction to B factories and a brief overview of KEKB and SuperKEKB accelerators and corresponding detectors will be given in chapter 1, then a more detailed and systematic description of the SuperKEKB accelerator will be given in chapter 2, describing the main concepts of the upgrade and what has been changed with respect to KEKB. In chapter 3 a theoretical overview to collimation is given, with a section dedicated to SuperKEKB collimators, that are essential for the studies described later. In chapter 4 a description of the main background sources in SuperKEKB, originated from single beam and from luminosity, is reported. Chapter 5 is dedicated to the description of the code used for the simulations and to the strategy used for collimators optimization with simulations. In the next three chapters collimators studies performed with simulations and data are reported: a collimators study in the commissioning run of 2018 is described in chapter 6, studies performed during the first run of 2019 are described in chapter 7, and studies done only on simulation for Fall 2019 optics and for the design machine parameters are described in chapter 8.

Chapter 1

Introduction to B factories

1.1 Introduction to B Factories

In the early 1980s physicists started to think about the possibility of using B meson decay to test the validity of the Cabibbo-Kobayashi-Maskawa (CKM) six-quark mechanism for CP violation. CP violation was expected to be observable in neutral B meson decays to CP eigenstates, such as $B^0 \to J/\Psi K_s^0$, but no such decays had been observed. The subsequent evidence of a long B meson lifetime from experiments at SLAC in 1983 and the discovery by the ARGUS experiment at DESY in 1987 of a substantial rate for $B^0 - \overline{B}^0$ mixing indicated that the CKM-matrix parameters were in an accessible range to be tested. It became clear that CP violation could be experimentally observed not only in neutral kaons, but also in the $B^0 - \overline{B}^0$ system. Moreover, the CP violation expected in the $B^0 - \overline{B}^0$ system was larger than the one seen in K decay. It was also shown by Bigi and Sanda that a measurement of CP violation in B decays to CP eigenstates could be interpreted without theoretical uncertainties. The problem, at that time, was that the available sample of B mesons was three orders of magnitude less than the one required to observe CP violation in B decays. The need for a larger statistics brought to the idea of the so called "B factories", e^+e^- colliders capable of producing 10^6 $B^0 - \overline{B}^0$ mesons pairs per day, which, compared with CESR at Cornell or DORIS II at DESY that were able to produce nearly 30 $B^0 - \overline{B}^0$ pairs per day, was an improvement of 5 orders of magnitude in less than 30 years. Together with the development of B factories, big progresses had been made in the capabilities of the detectors, especially in the data acquisition systems (to deal with the huge amount of data produced), in tracking and vertexing performances, in software and storage technology.

At the time of CESR and DORIS II, the most successful studies of B mesons were performed operating the colliders at the center-of-mass energy of the $\Upsilon(4S)$ resonance, which decays almost 100% of the time in B mesons pairs, providing a

Parameter	Units	PEP-II	KEKB
Beam energy	GeV	9.0 (e^-) - 3.1 (e^+)	8.0 (e^-) - 3.5 (e^+)
Beam current	A	1.8 (e^-) - 2.7 (e^+)	1.2 (e^-) - 1.6 (e^+)
σ_x^*	μm	140	80
σ_y^*	μm	3.0	1.0
σ_z	mm	8.5	5.0
Luminosity	$cm^{-2}s^{-1}$	1.2×10^{34}	2.1×10^{34}
n. of bunches		1732	1584
Bunch spacing	m	1.25	1.84
Crossing angle	mrad	0 (head-on)	$\pm$11 (crab-crossing)

Table 1.1: *Final machine parameters for PEP-II and KEKB. $\sigma_{x,y}^*$ are the beam sizes in the transverse directions, while σ_z is the longitudinal beam size.*

low-background environment to study. However, luminosities were low, of the order of 10^{32} $cm^{-2}s^{-1}$, too low to provide a statistically significant sample of B mesons for CP violation studies. In 1987 Pier Oddone proposed the concept of an asymmetric e^+e^- circular collider that would operate at the $\Upsilon(4S)$ resonance and produce B mesons pairs with a lab-frame boost sufficient for time-dependent measurements. Among the B factories projects that were proposed during the 1980s, only PEP-II at SLAC and KEKB at KEK were realized. Both projects included an instantaneous luminosity higher than 10^{33} $cm^{-2}s^{-1}$ and a boost of the center-of-mass sufficient to observe the time evolution of B mesons decays. PEP-II used a head-on collisions scheme, while KEKB used a scheme with a crossing angle of 22 mrad. The main machine parameters of PEP-II and KEKB are listed in table 1.1.

The similarities are not limited only to the machines, also detectors, BaBar and Belle, had similar operational performances and requirements:

- To reduce multiple scattering and keep good tracking performance, material budget, especially in the inner part of the detector, should be minimized. Therefore beryllium was used to build the beam pipe around the interaction point (IP) of the beams, and material budget was also minimized in the design of the tracking and vertexing detectors.

- Vertex detectors were built using silicon strip detectors, the best technology available at that time to determine with the required precision the decay vertex of B mesons.

- Tracking and low-momentum particle identification: both experiments used a drift chamber with helium based gas (80:20 of He:C_4H_{10} for BaBar and 50:50 of He:C_2H_6 for Belle) and aluminum wires, in order to minimise the multiple scattering and keep good tracking performance. Drift chambers were also used

to perform particle identification for low momentum charged particles with the required dE/dx resolution.

- For higher momentum particle identification BaBar used the Detector of Internally Reflected Cherenkov light (DIRC), while Belle used a Time-Of-Flight system and an aerogel-based Cherenkov detector.

- To precisely measure the energy of charged and neutral particles, the detectors used an electromagnetic calorimeter, using CsI(Tl) crystals.

- To verify the observation of CP violation in B decays, it would have been important to measure both CP eigenstates, detecting K^0_S and K^0_L. Given the lifetime difference between K^0_S and K^0_L, the former was expected to decay in the beam pipe or in the vertex detector, the latter was expected to travel much more, traversing all other sub-detectors, so the outer parts of detectors at the B factories had layers of an active detector with layers of an absorber material in between, to detect K^0_L mesons.

- The high luminosity of the machines meant a significant amount of data to be processed by the front-end electronics and the trigger system, and to be stored for later analysis, so the data flow and offline computing systems had to be improved to keep up with the data delivered by the colliders.

- Together with higher data sample, accelerators were also delivering higher machine-induced background to the detectors, so more countermeasures had to be developed to reduce the background on the detectors.

The excellent performances of PEP-II and KEKB allowed the respective BaBar and Belle detectors to verify the Cabibbo-Kobayashi-Maskawa (CKM) theory of CP violation, together with many other measurements and discoveries. More details and results can be found in "The Physics of the B Factories" [1].

1.2 The KEKB accelerator

The construction of the KEKB accelerator [2] started in 1994, using the existing TRISTAN tunnel, and ended in November 1998. KEKB was a two-ring electron-positron collider with asymmetric energies and a design luminosity of 10^{34} cm^{-2}s^{-1}. Both rings were 3016 m long and installed in a tunnel 11 meters below ground level. One ring was operated with 8 GeV electrons (HER - High Energy Ring) and the other was operated with 3.5 GeV positrons (LER - Low Energy Ring), with currents of 1.1 A and 2.6 A respectively. There was one interaction point (IP), where beams collided with a crossing angle of ± 11 mrad. Around the IP, the Belle detector (briefly

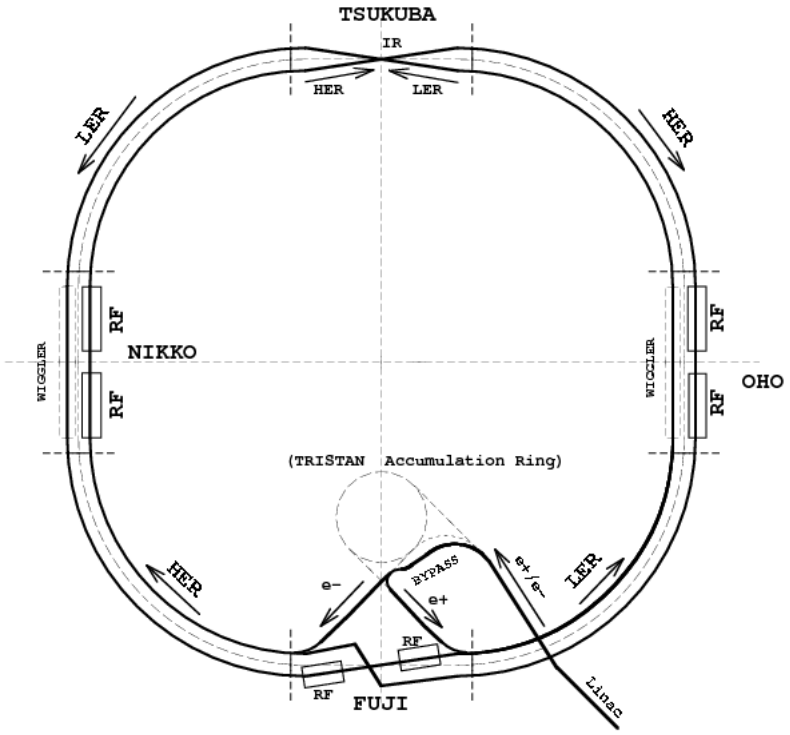

Figure 1.1: *Schematic view of the KEKB accelerator.*

described in section 1.2.1) was placed to record the interactions. Another cross-over point was located opposite to the IP, where the rings exchanged inner and outer positions, in order to keep both rings of the same length.

Electrons and positrons were directly injected from a linac-complex into the main ring at full energies. The Linac was updated for this purpose from the original 2.5 GeV to 8 GeV, with the positron production target installed at the 3.7 GeV point. In this way both beams could be injected at nominal energies in the KEKB rings, building a new 400 m tunnel for a beam transport line connecting directly the Linac to KEKB main ring. Thus RF cavities installed in the main ring had the only function to compensate for the energy loss due to synchrotron radiation. Fig. 1.1 shows the basic layout of the KEKB accelerator.

Beams were divided in 5000 bunches with a bunch spacing of 59 cm. The design beam size at the IP was 80 μm in the horizontal direction and 1.0 μm in the vertical direction. Many potential issues were coming from coupled-bunch instabilities (CBIs), against which many countermeasures were taken. First of all, the beam pipes were made of copper, that has a self-shielding capability against synchrotron light and a low photo-desorption coefficient. The LER vacuum chamber had also a round shape with a large radius of 94 mm, very effective against the growth rate of CBIs due to the resistive-wall impedance. Other sources of instabilities are the RF cavities, where a beam excites the fundamental mode and higher-order modes (HOMs). The fundamental mode is the lowest-frequency mode, used for accelera-

tion, whereas HOMs are modes with higher frequencies. The easiest way to mitigate coupled-bunch instabilities from HOMs is to use cavities with a high suppression of HOMs. KEKB used two types of such cavities: normal conducting ARES (Accelerator Resonantly coupled with Energy Storage) cavities, used in both LER and HER rings, and SuperConducting Cavities (SCC) for the HER. In large rings such as the KEKB ones, also the fundamental mode of a RF cavity may excite coupled-bunch instabilities, thus ARES cavities were equipped with a large energy-storage cell, so that the detuning of the cavity resonance frequency became smaller than the revolution frequency of the ring, avoiding the excitation of the fundamental mode instability.

The design of the interaction region was simplified by the finite crossing angle between the beams: no separation dipole magnets were required and bunches were quickly separated after the collision point, allowing the small bunch spacing of 59 cm. Two superconducting quadrupole magnets, fully immersed in the solenoidal 1.5 T magnetic field used by the Belle detector, were used to squeeze the beams at the IP to maximise luminosity.

Machine commissioning started in December 1998, while the data taking with the Belle detector started in June 1999 and lasted until June 2010. The design instantaneous luminosity of 10^{34} $\mathrm{cm^{-2}s^{-1}}$ was achieved already in 2003, and the highest achieved value was obtained in June 2009 with a value of 2.11×10^{34} $\mathrm{cm^{-2}s^{-1}}$. The total integrated luminosity recorded by Belle in the 11 years of operation was 1041 $\mathrm{fb^{-1}}$.

1.2.1 The Belle detector

The Belle Collaboration was officially established on October 7th, 1993, during a meeting at Osaka University. The Belle group initially counted 136 members from 39 institutions from 7 countries, and by 2012 (two years after the end of data taking) it grew up to 470 members from 72 institutions of 16 different countries.

The Belle collaboration was the result of a task force organized to study the physics potential of a high luminosity, asymmetric $\mathrm{e^+e^-}$ collider operating at the $\Upsilon(4S)$ resonance, in particular to test the CKM mechanism for CP violation. It was demonstrated that such tests could be done with a data sample of $\sim 10^7$ B mesons decays, corresponding to integrated luminosities at the Υ(4S) of the order of 100 $\mathrm{fb^{-1}}$, accumulated with a 4π detector with state-of-the-art capabilities. Fig. 1.2 shows the configuration of the Belle detector [3]. The detector was built around a 1.5 T superconducting solenoid and iron structure surrounding the KEKB beams at the Tsukuba interaction region. The beam crossing angle was $\pm$11 mrad. B mesons decay vertexes were measured by a Silicon Vertex Detector (SVD) lo-

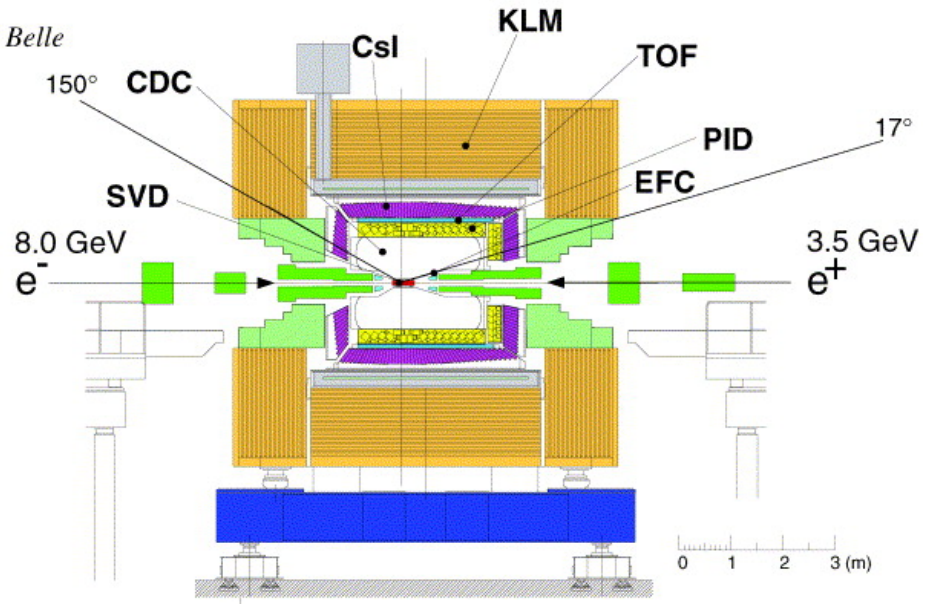

Figure 1.2: *Side view of the Belle detector.*

cated around the cylindrical beryllium beam pipe that surrounds the interaction point. Charged particles tracking was also provided by a wire Drift Chamber (CDC). Particle identification was done by dE/dx measurements in CDC, and by Aerogel Cherenkov Counters (ACC) and time-of-flight counters (TOF) located radially outside the CDC. Electromagnetic showers were detected in an array of CsI(Tl) crystals placed inside the solenoid coil. Muons and K_L mesons were identified by arrays of resistive plate counters interspersed in the iron yoke. The detector covered the θ region extending from 17° to 150°. A part of the otherwise uncovered small-angle region was instrumented with a pair of BGO crystal arrays (EFC) placed on the surfaces of the QCS cryostats in the forward and backward directions.

1.3 The SuperKEKB - Belle II upgrade

Most of the measurements done at B-factories like KEKB and PEP-II are limited by statistical errors, and one obvious way to improve the uncertainty on these measurements is to collect at least one order of magnitude bigger data samples. For this reason the upgrade of KEKB to SuperKEKB [5] [6] [7] has been developed, with a target instantaneous luminosity of 8×10^{35} cm^{-2}s^{-1}, a factor 40 higher than the one achieved at KEKB. As will be shown more systematically in section 2.1, there are two key factors that can be changed to arrive to such a challenging luminosity: the vertical beta function at the IP (β_y^*) and beam currents. Factors like the increase of the impedance, the electron cloud effect, the operating costs limit the increase in beam currents, so the biggest gain in luminosity can be achieved reducing β_y^*. For SuperKEKB it was decided to double the currents used in KEKB and gain the

remaining factor 20 reducing the vertical beta function at the IP. With such a small β_y^* a new collision scheme was necessary to avoid luminosity degradation due to the hourglass effect, thus it was decided to adopt the so called "nano-beam scheme", proposed for the first time by P. Raimondi for the SuperB project [8] [9]. Beam energies were also changed: LER beam energy has been changed from 3.5 GeV to 4.0 GeV to increase Touschek lifetime, while HER beam energy has been decreased from 8.0 GeV to 7.0 GeV to reduce losses due to synchrotron radiation. Many of the KEKB lattice components were reused, as well as the tunnel and the infrastructure, but the new requirements had an impact on many parts of the facility, that needed to be replaced and in some cases specifically developed for SuperKEKB. In particular:

- In the Low Energy Ring, the main dipole magnets were replaced with longer ones, and the wiggler sections were reformed adding new magnets, so to have twice as many wiggle pitches as before. The arc sections in the High Energy Ring were reused, some quadrupoles in the arc cells were adjusted and a wiggler section was added in one of the straight sections.

- For the new collision scheme with the extremely low β_y^*, a new final focus superconductive magnets system was designed and employed, which required state-of-the art design and technology. The beam lines in the final 300 meters before the interaction point were fully reconstructed for both rings, adding local chromaticity correction sections for both vertical and horizontal planes.

- To cope with the electron cloud effect in the LER observed already in KEKB and studied also in other machines, some countermeasures were taken, including beam pipes with antechambers and internal TiN coating, grooves in the internal surface of dipole magnets, clearing electrodes in wiggler magnets, solenoids in field-free regions.

- To increase beam currents, vacuum components were upgraded to have lower impedance and higher thermal strength. The RF system was reinforced to deliver high power to the beams, re-using the ARES and super conducting cavities after improving their input couplers and HOMs dampers.

- Beam instrumentation and control systems, including beam position monitors, beam size monitors, bunch-by-bunch feedback system, and collision feedback system, were upgraded to provide the higher performance required for the lower emittance beams and smaller beam size at the IP.

- The injector linac was upgraded to include a new low emittance RF electron gun, improvements to the positron source, and the implementation of pulse

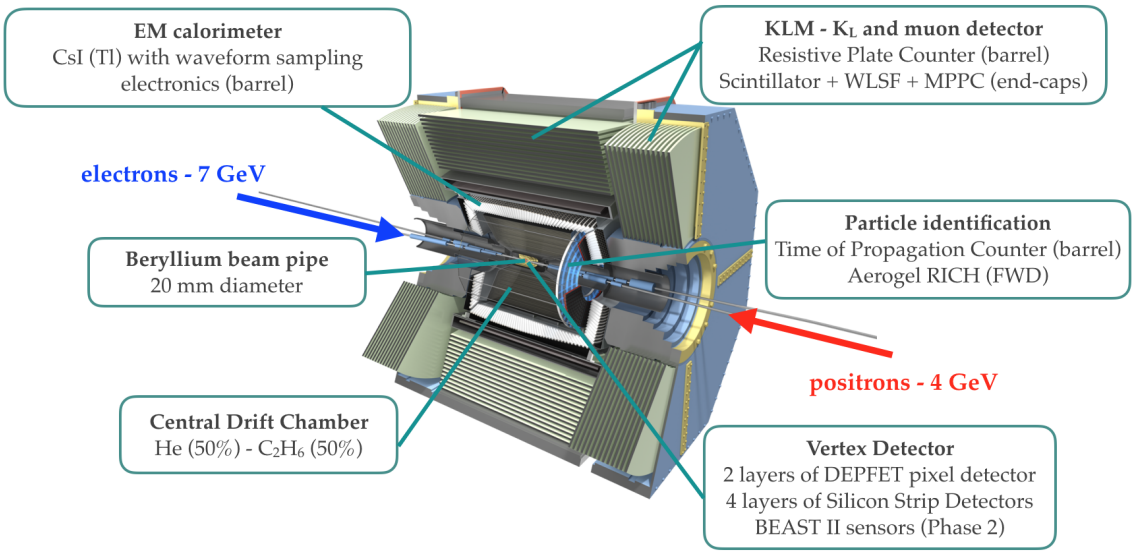

Figure 1.3: *Schematic view of the Belle II detector.*

magnets.

- A new 1.1 GeV damping ring was built and commissioned in 2018 to reduce positron beam emittance before the injection into the main ring.

A more complete description of the SuperKEKB machine is given in chapter 2.

1.3.1 The Belle II Detector

The design of a new machine capable of delivering an instantaneous luminosity 40 times higher than KEKB meant new requirements also for the detector, that needed a significant upgrade to cope with new machine conditions. The scheme of the upgraded detector, called Belle II, is shown in fig. 1.3. With the higher luminosity, the detector is expected to receive higher backgrounds and radiation, and the occupancies in the different sub-systems will be much higher than in Belle. In addition, a more efficient event selection and a reinforced data acquisition system are needed.

The VerteX Detector (VXD) region has been expanded, with the outer radius being 135 mm, and different technologies have been employed. The first two layers of the VXD consist of a PiXel Detector (PXD), made by DEPFET pixel sensors, whose first layer is located at a radius of 14 mm from the IP, right outside the beam pipe. Its performance is essential to improve the vertex position resolution. Around the PXD there is the Silicon Vertex Detector (SVD), made by four layers of double sided silicon strip detectors at radii from 39 mm to 135 mm, with a very fast readout chip and stand alone tracking capability. The full VXD is used for tracking charged particles and reconstruct the decay vertices of B mesons produced during collisions.

Outside the VXD there is the Central Drift Chamber (CDC), a wire drift chamber used for tracking charged particles and reconstruct their momenta, for identification of low momentum particles for which the outer PID sub-detectors are not efficient, and to provide a trigger signal for charged particles. The CDC inner radius is larger than before because of the expanded VXD volume, but since the outer PID sub-detectors are compact, the outer radius has been also increased. CDC has been equipped with new readout electronics to handle the higher trigger rate.

There are also two new particle identification systems, the Time Of Propagation (TOP) Cherenkov light detector in the barrel region and the Aerogel Ring-Imaging Cherenkov (ARICH) in the forward end-cap region, essential to discriminate pions from kaons. In the TOP, Cherenkov photons are internally reflected in long quartz bars of 20 mm thickness that surround the CDC outer wall, and collected by micro-channel plate (MCP) PhotoMultiplier Tubes (PMT); a focusing system is also used to reduce the chromaticity of Cherenkov light. The ARICH consists of 2 cm of an aerogel radiator, 20 cm of expansion volume to allow Cherenkov photons to form rings on an array of photon detectors, that are capable of detecting single photons in a high magnetic field, and a read-out system for the photon detector.

Around the TOP detector, the Electromagnetic Calorimeter (ECL) is placed. It consists of 8736 CsI(Tl) crystals of different shapes to fully cover the barrel and both end-caps regions. Each crystal is equipped with two photodiodes glued on the rear surface, providing two independent signals. The main task of the ECL is the detection of neutral particles, with high efficiency and precise determination of photon energy and angular coordinates. ECL also provides trigger signal and luminosity measurement. In the barrel region, the electronics has been upgraded to shorten the shaping time to 0.5 μs.

The last Belle II sub-detector, placed just around the superconducting solenoid, is the K_L and muon detector (KLM). Like the ECL, there are a barrel region and two end-cap regions, both made by iron plates alternated with active detector layers. The iron plates act as magnetic flux return for the solenoid and as absorber for the particles to be detected. In Belle, the detector layers were made entirely by resistive plate chambers (RPC), but their long dead time and the higher expected background rates made necessary an upgrade in the end-cap regions and in the first two layers of the barrel region, replacing the RPCs with scintillators.

The higher luminosity of SuperKEKB will increase the background levels for the Belle II detector. There are two factors to take into account with higher background levels: performance degradation due to high instantaneous rates and long term radiation damage. Some countermeasures were already taken during the design of Belle II sub-detectors to avoid problems due to radiation damage, with the expected background levels and an additional safety factor. Nonetheless, it was known that

lifetime of TOP PMTs had to be preserved until the replacement foreseen in 2021, so a safety limit on PMT rates was set, preventing the increase in beam currents. The high voltage of the CDC tripped several times due to high background levels, that caused also persistent currents in the outer layers. Regarding performances, PXD and SVD occupancies are crucial to assure a high efficiency of tracking performance. CDC tracking efficiency can also be affected by beam background, but a new software and standalone tracking in the VXD can improve the overall efficiency, so in the end the occupancy levels in the VXD are the important ones and must be kept low enough. These critical issues emerged during the first data taking period with the complete detector and accelerator, that took place in spring 2019. The different commissioning and running phases will be described in section 2.4.

Chapter 2

The SuperKEKB accelerator

The SuperKEKB complex is located in Tsukuba, Japan, inside the KEK Research Organization, and consists of a 7 GeV electron ring (HER), a 4 GeV positron ring (LER), an injector linear accelerator (linac), and a 1.1 GeV positron damping ring (DR), as shown in fig. 2.1. In this chapter, a description of the SuperKEKB accelerator is given. SuperKEKB collimators will be described in section 3, together with an introduction on beam halo and collimation.

2.1 Main concepts of the SuperKEKB upgrade

2.1.1 Luminosity

The most important requirement for the SuperKEKB accelerator is the instantaneous luminosity, which could be defined as the interaction rate per unit cross section for colliding particles. With this basic definition, the number of physics events can be expressed as:

$$evt = \int_0^T L\sigma dt \tag{2.1}$$

where L is the luminosity, σ is the cross section of a physical process, and T could be a running period of the machine or the whole duration of the experiment. Considering that the cross section is fixed by the physics of the processes occurring during the interaction between colliding particles, the way to increase the number of events, keeping fixed the duration of the experiment, is to increase the luminosity.

In the case of a collider, both beams are at the same time the target and the incoming beam. To find an analytical expression of the luminosity, considering the beams divided into bunches, the variables to be considered are the number of particles inside a bunch $N_{1,2}$, the three-dimensional particles density distribution $\rho_{1,2}(x, y, s)$, and the bunch length σ_z. Assuming head-on collision between the bunches travelling at the speed of light and Gaussian density distributions, once the

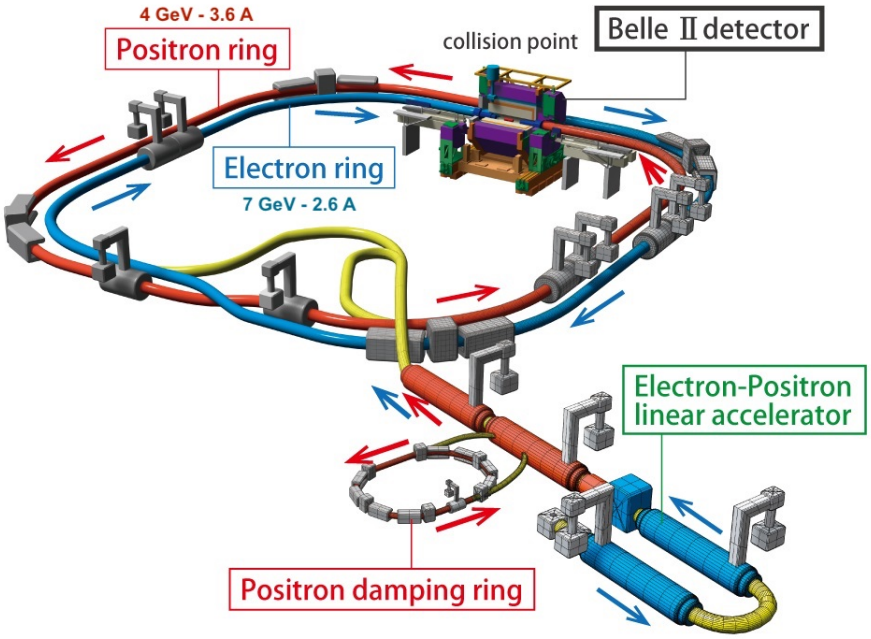

Figure 2.1: *Schematic view of the SuperKEKB facility.*

integrals of the density distributions are calculated, luminosity can be expressed as:

$$L = \frac{N_1 N_2 f n_b}{4\pi\sigma_x\sigma_y} \tag{2.2}$$

where n_b is the number of bunches in the beams and f is the revolution frequency. There is no dependence on the bunch length in this formula, because particle density distributions are assumed to be uncorrelated one with each other and beam sizes are assumed constant through the bunch length. Actually this is not true, because the betatron function has in general a parabolic shape. When the bunches interact at the point where the beta function has a minimum, also called "waist", the beam size given by $\sqrt{\beta(s)\cdot\varepsilon}$ is at the minimum and the luminosity is maximised, but away from the waist the beta function increases as:

$$\beta(s) = \beta^*(1 + \left(\frac{s}{\beta^*}\right)^2) \tag{2.3}$$

so the beam size increases and the luminosity decreases away from the bunch waist. This effect is called "*hourglass effect*" and becomes particularly important when the value of the beta function at the interaction point is similar to the bunch length. Therefore a condition to avoid the hourglass effect can be written as follows:

$$\beta_y^* \geq \sigma_z \tag{2.4}$$

There are other beam parameters that can influence luminosity, so equation 2.2

can be re-written as follows for an electron-positron collider:

$$L = \frac{\gamma_{\pm}}{2er_e}\left(1 + \frac{\sigma_y^*}{\sigma_x^*}\right)\left(\frac{I_{\pm}\xi_{y\pm}}{\beta_y^*}\right)\left(\frac{R_L}{R_{\xi_{y\pm}}}\right) \tag{2.5}$$

where "+" and "-" denote positrons and electrons respectively, $\sigma_{x,y}^*$ is the beam size at the IP in horizontal and vertical plane, I is the beam current, β_y^* is the vertical betatron function at the IP, $\xi_{y\pm}$ is the vertical beam-beam parameter, R_L and $R_{\xi_{y\pm}}$ are the reduction factors for luminosity and beam-beam parameter, r_e is the classical electron radius, γ is the Lorentz factor. It is assumed that the vertical beta function and the transverse beam size are the same for positrons and electron beams. In equation 2.5 there is no explicit dependance from the horizontal betatron function at the IP (β_x^*), the horizontal emittance (ε_x), the bunch length (σ_z) and the crossing angle between the beams; all these parameters are somehow included in the beam-beam parameter and in the reduction factors to take into account the hourglass effect and the finite crossing. From eq. 2.5 is clear that the luminosity is directly proportional to the beam-beam parameter and beam currents, while is inversely proportional to the vertical beta function at the IP.

The vertical beam-beam parameter is given by:

$$\xi_{y\pm} = \frac{r_e}{2\pi\gamma_{\pm}}\frac{N_{\mp}\beta_y^*}{\sigma_y^*(\sigma_x^* + \sigma_y^*)}R_{\xi_{y\pm}} \propto \frac{N_{\mp}}{\sigma_x^*}\sqrt{\frac{\beta_y^*}{\varepsilon_y}} \tag{2.6}$$

where N is the number of particles in a bunch. In principle, increasing the number of particles per bunch, the beam-beam parameter can be increased, and so could be the luminosity. However, there is a limit for the beam-beam parameter around $\sim$0.1, at this value a further increase in bunch population is compensated by an increase in the vertical emittance, so no more improvement is possible. However, there is still the possibility to improve luminosity keeping the ratio between β_y^* and ε_y, so that the beam-beam parameter can be kept at its limit squeezing the vertical beta function at the IP while reducing also the vertical emittance. This option is the key toward the β_y^* reduction in SuperKEKB by a factor 20 with respect to KEKB.

2.1.2 Nano-beam scheme

The huge reduction in β_y^*, as already anticipated in section 1.3, led to the need of a new collision scheme that could avoid luminosity degradation due to the hourglass effect, whose condition has been given by equation (2.4). The new collision scheme is called "nano-beam scheme", which is similar to the "crab waist" scheme proposed by P. Raimondi, with the difference that there are no crab sextupoles in the design

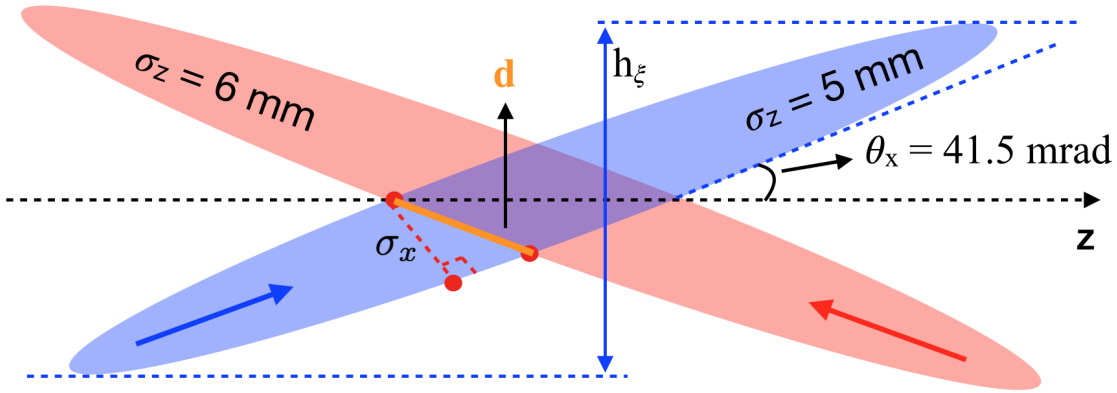

Figure 2.2: *Scheme of beam crossing in SuperKEKB.*

of the SuperKEKB final focus system. The idea is to use a large Piwinski angle:

$$\phi_{Piw} = \frac{\sigma_z}{\sigma_x^*} tan\theta_x \tag{2.7}$$

where θ_x is the half crossing angle between the beams. The advantage of this solution is that, with a large enough crossing angle, σ_z in the equation (2.4) can be replaced with the longitudinal size of the overlap region between the bunches, shown in fig. 2.2. So β_y^* has just to be greater than what can be called "effective bunch length" d:

$$\beta_y^* \geq d = \frac{\sigma_x^*}{sin(2\theta_x)} \tag{2.8}$$

As can be easily verified looking at the table 2.1, SuperKEKB design parameters fulfil this requirement, with a horizontal beam size small enough and a large crossing angle of 83 mrad. For example, for the LER:

$$\sigma_x^* = 10\mu\text{m} \qquad d_{LER} = \frac{\sigma_x^*}{sin(2\theta_x)} \approx 129\mu\text{m} \qquad \beta_y^* = 270\mu\text{m} > d_{LER} \tag{2.9}$$

whereas with $\sigma_z \simeq 6$ mm the condition (2.4) would be clearly violated.

Another effect of the nano-beam scheme regards the horizontal beam-beam parameter. Re-writing eq. (2.6) for the horizontal beam-beam parameter, it can be seen that it depends on the horizontal beam size at the IP. Considering the crossing angle, in the evaluation of the horizontal beam-beam parameter the horizontal beam spot is not just the nominal beam size, it's a wider region equal to:

$$h_\xi = \sigma_z \text{sin}\theta_x \tag{2.10}$$

as can be seen in fig. 2.2. This expression can be used to replace σ_x^* in the horizontal

beam-beam parameter formula, that becomes:

$$\xi_{x\pm} = \frac{r_e}{2\pi\gamma_\pm}\frac{N_\mp\beta^*_x}{\sigma^*_x(\sigma^*_x+\sigma^*_y)}R_{\xi_{x\pm}} \propto \frac{N_\mp\beta^*_x}{(\sigma_z \sin\theta_x)^2} \tag{2.11}$$

where, again, we assume that the beta function and the longitudinal beam size are the same for LER and HER. Therefore dynamic effects like dynamic beta function and dynamic emittance in the horizontal direction, that cause problems with the aperture, can be reduced with the nano-beam scheme thanks to the small horizontal beam-beam parameter.

2.1.3 Beam energies

Beam energies are determined by the physics of interest: being a B-factory, the most important center-of-mass energy is the one corresponding to the mass of the $\Upsilon(4S)$, that decays in a pair of $B\overline{B}$ mesons with a branching ratio of 0.96. Beam energies are 4 GeV for LER and 7 GeV for HER, which determines a boost of the center-of-mass frame of $\beta\gamma = 0.28$, necessary to resolve the distance between the decay vertices of B mesons. The boost is smaller than the KEKB one by almost a factor 2, but there is no impact on physics thanks to the first layer of the Belle II vertex detector which is at a radius smaller by more than a factor 2 compared to Belle/KEKB, compensating the uncertainty on the impact parameter. The boost reduction comes from the need to change beam energies to compensate some effects that would increase due to the increase in beam currents. LER beam energy has been increased from 3.5 GeV to 4.0 GeV to reduce Touschek losses, that scale with E^{-3}, and to decrease emittance growth due to intra-beam scattering. HER beam energy was decreased to reduce the horizontal emittance and the power consumption due to synchrotron radiation, that scales with E^4. The range of center-of-mass energies goes from the $\Upsilon(1S)$ to the $\Upsilon(6S)$, with a maximum at $E_{CM} = 11.24$ GeV due to the maximum beam energy of the injector linac.

Table 2.1 shows a comparison between machine parameters of KEKB and SuperKEKB. In SuperKEKB beam currents are doubled, the vertical beta function at the IP is reduced by a factor 1/20, the vertical beam-beam parameter has been limited to 0.09 considering the experience with KEKB. Emittances are also reduced and beams are basically flat, with three orders of magnitude difference between horizontal and vertical beam sizes. Low beta functions mean also a decrease in dynamic aperture, resulting in short beam lifetimes and strict requirements for injection.

		KEKB		SuperKEKB		
		LER	HER	LER	HER	Units
Beam energy	E	3.5	8.0	4.0	7.007	GeV
Circumference	C	3016.262		3016.315		m
Half crossing angle	θ_x	0 (11[a])		41.5		mrad
Piwinski angle	ϕ_{Piw}	0	0	24.6	19.3	
Horiz. emittance	ε_x	18	24	3.2	4.6	nm
Vert. emittance	ε_y	150	150	8.64	12.9	pm
Coupling		0.83	0.62	0.27	0.28	%
Beta function at IP	β_x^*/β_y^*	1200/5.9	1200/5.9	32/0.27	25/0.30	mm
Horiz. beam size	σ_x^*	147	170	10.1	10.7	μm
Vert. beam size	σ_y^*	940	940	48	62	nm
Horiz. betatron tune	ν_x	45.506	44.511	44.530	45.530	
Vert. betatron tune	ν_y	43.561	41.585	46.570	43.570	
Momentum compaction	α_p	3.3	3.4	3.20	4.55	10^{-4}
Energy spread	σ_ϵ	7.3	6.7	7.92	6.37	10^{-4}
Beam current	I	1.64	1.19	3.6	2.6	A
Number of bunches	n_b	1584		2500		
Particles/bunch	N	6.47	4.72	9.04	6.53	10^{10}
Energy loss / turn	U_0	1.64	3.48	1.76	2.43	MeV
Long. damping time	τ_z	21.5	23.2	22.8	29.0	msec
RF frequency	f_{RF}	508.9		508.9		MHz
Total cavity voltage	V_c	8.0	13.0	9.4	15.0	MV
Total beam power	P_b	~ 3	~ 4	8.3	7.5	MW
Synchrotron tune	ν_s	-0.0246	-0.0209	-0.0245	-0.0280	
Bunch length	σ_z	~ 7	~ 7	6.0	5.0	mm
Effective bunch length	d	-	-	129	122	μm
Horiz. beam-beam par.	ξ_x	0.127	0.102	0.0028	0.0012	
Vert. beam-beam par.	ξ_y	0.129	0.090	0.088	0.081	
Luminosity	L	2.108×10^{34}		8×10^{35}		$cm^{-2}s^{-1}$
Integrated luminosity	$\int L$	1.041		50		ab^{-1}

Table 2.1: *Machine parameters of KEKB and SuperKEKB. KEKB parameters are those achieved with crab crossing, where the effective crossing angle was 0. ([a]) refers to before the crab crossing was used in KEKB.*

2.2 Lattice design and hardware upgrades

The use of a new collision scheme led to a partial re-design of the machine optics and to the modification of some components, in order to achieve low horizontal and vertical emittances, low vertical beta functions at the interaction point and a good dynamic aperture to keep high Touschek lifetimes. On the other hand, to limit the cost and the amount of work needed for the upgrade, an additional requirement was to re-use as much as possible magnets from KEKB, and to use the KEKB tunnel with no additional infrastructures to be realised. In this section, an overview of the machine optics and the most important modifications is given.

2.2.1 New lattice design

Optics of the arc section

In an electron ring, the emittance can be expressed as [6] [11]:

$$\varepsilon_x = \frac{C_\gamma \gamma^2}{J_x} \frac{1}{2\pi\rho^2} \oint H(s)\, ds \tag{2.12}$$

where

$$C_\gamma = \frac{55}{32\sqrt{3}} \frac{\hbar}{mc} \tag{2.13}$$

$$H(s) = \gamma_x \eta_x^2 + 2\alpha_x \eta_x \eta_{p_x} + \beta_x \eta_{p_x}^2 \tag{2.14}$$

J_x is the damping partition number, ρ is the curvature of dipole magnets, α_x, β_x, γ_x are the horizontal Twiss parameters, η_x and η_{p_x} are the horizontal dispersions. These formulae are applicable in absence of X-Y and X-Z couplings. To have a small emittance in the design of an arc cell without X-Y and X-Z couplings, the integral of H in the dipole magnets must be reduced, the radius of curvature in the dipoles should be increased and the damping partition number should be maximised. With respect to KEKB, a decrease in the HER emittance is achieved decreasing the beam energy from 8 GeV to 7 GeV. In addition, wiggler magnets (described later in this section) are used to decrease the emittance in both beams.

For the new optics design, the basic cell structure of the arc sections was not modified, but many magnets and power supplies for the magnets had been replaced, rearranged or added. The main modification was the replacement of 100 old 0.89 m long dipole magnets in the LER arc sections with new 4.2 m long dipoles, that have a larger radius of curvature, to achieve the design value of the horizontal emittance. In the HER the old dipoles were reused, the horizontal emittance could be reduced enough adjusting the quadrupole magnets in the arc cells. Quadrupoles were mostly reused for both rings. In fig. 2.3 the design of the arc sections for LER and HER

are shown, with the plots of the betatron functions and the dispersion as a function of the longitudinal coordinate.

Optics of the straight sections

Also in straight sections some modifications were realised, especially on the wiggler magnets to help reducing the horizontal emittance. The LER wiggler sections in the Oho and Nikko straight sections were rearranged to double the wiggle pitches by adding new half-pole and single-pole wiggler magnets to the existing double-pole magnets. A new wiggler section in the HER was made recycling wiggler magnets from the LER. In fig. 2.4 the design of the wigglers section is shown for LER and HER. In the Tsukuba straight section, for about 150 meters on both sides of the interaction point, new beam lines for both rings were built.

Another element in the Nikko straight section is the "*chicane*", which consists of four dipole magnets. The HER circumference length is adjusted changing the RF frequency, but this will also change the LER circumference, that must be adjusted later independently. The chicane is used to perform this adjustment, with a variable range of $\pm$ 3 mm. The maximum bending angle is 38.83 mrad for each dipole magnet and the nominal angle is 27.46 mrad. After the Great East Japan earthquake in March 2011 the alignment of existing magnets was lost, and all the reference points of the magnet alignment system located in the tunnel became useless, so all alignment target were re-built, and all existing and new magnets were re-aligned. The high accuracy of the alignment was verified measuring the difference in the circumference between the two rings, that was found to be only 0.2 mm, well adjustable within the range of the chicane magnets of LER.

To improve optics control around the interaction region, it was proposed to use tilting sextupole magnets with variable angles to control the ratio of the skew sextupole filed component to the normal sextupole filed component [12]. To allow tilting sextupoles in a range of $\pm 30^\circ$ with a precision of 0.1 mrad, a table on which existing sextupoles had to be mounted was developed and realised. A total of 24 sets of sextupole magnets and tables were assembled and installed in the beam lines.

In the Fuji straight section, injection and abort systems are installed. To allow multi-turn injection, two injection kickers are used to make a local orbit bump to merge the stored and the injected beams. The horizontal phase advance between the two kickers is π. The abort system uses abort kickers in both rings to steer beams towards the absorbers, with the difference only in the way the beam size is increased: in the HER two sextupole magnets, connected by a $-I'$ matrix to cancel the non-linear kicks, are used, while in the LER pulse quadrupole magnets are used.

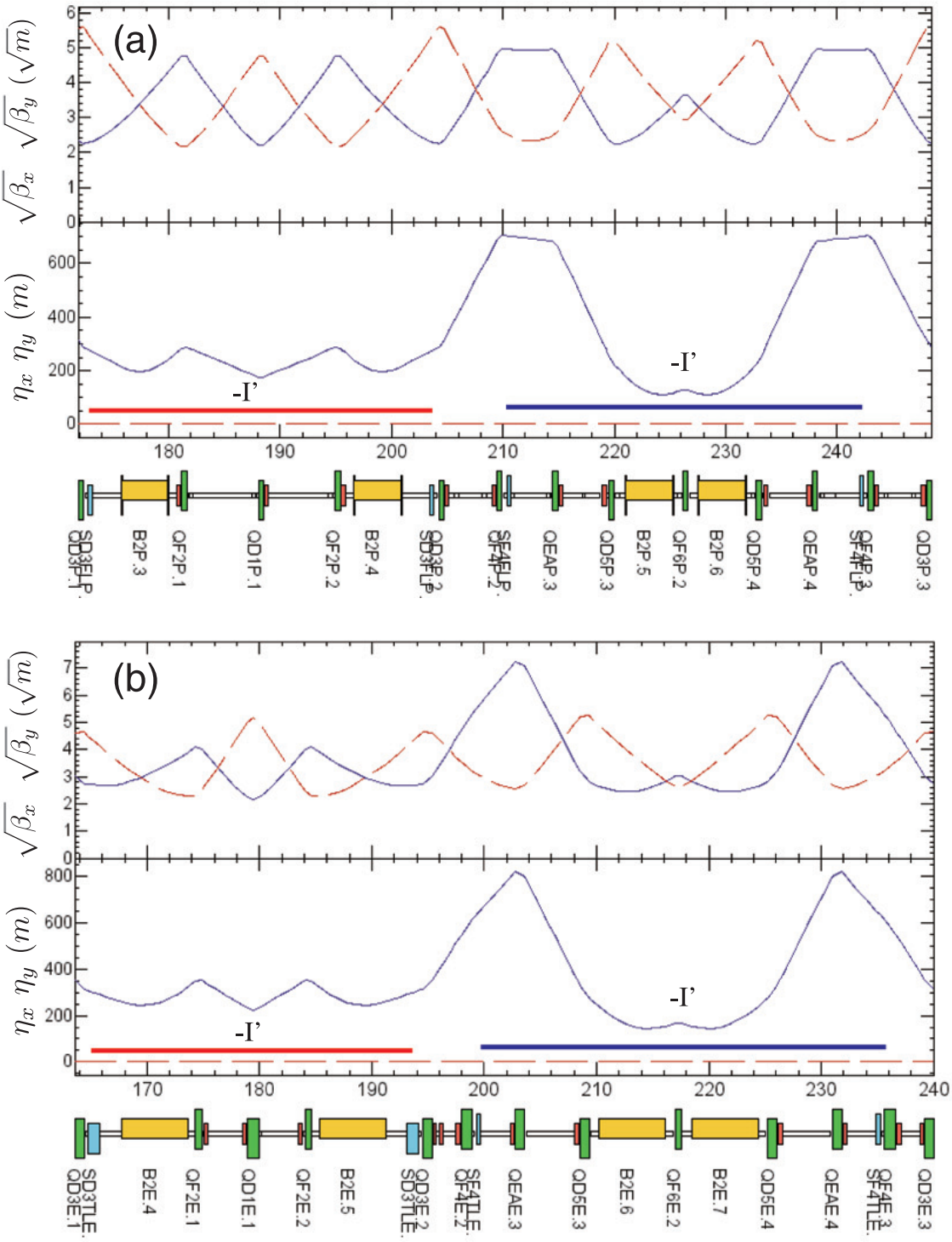

Figure 2.3: *Lattice design and optics of the basic arc section for LER (a) and HER (b).*

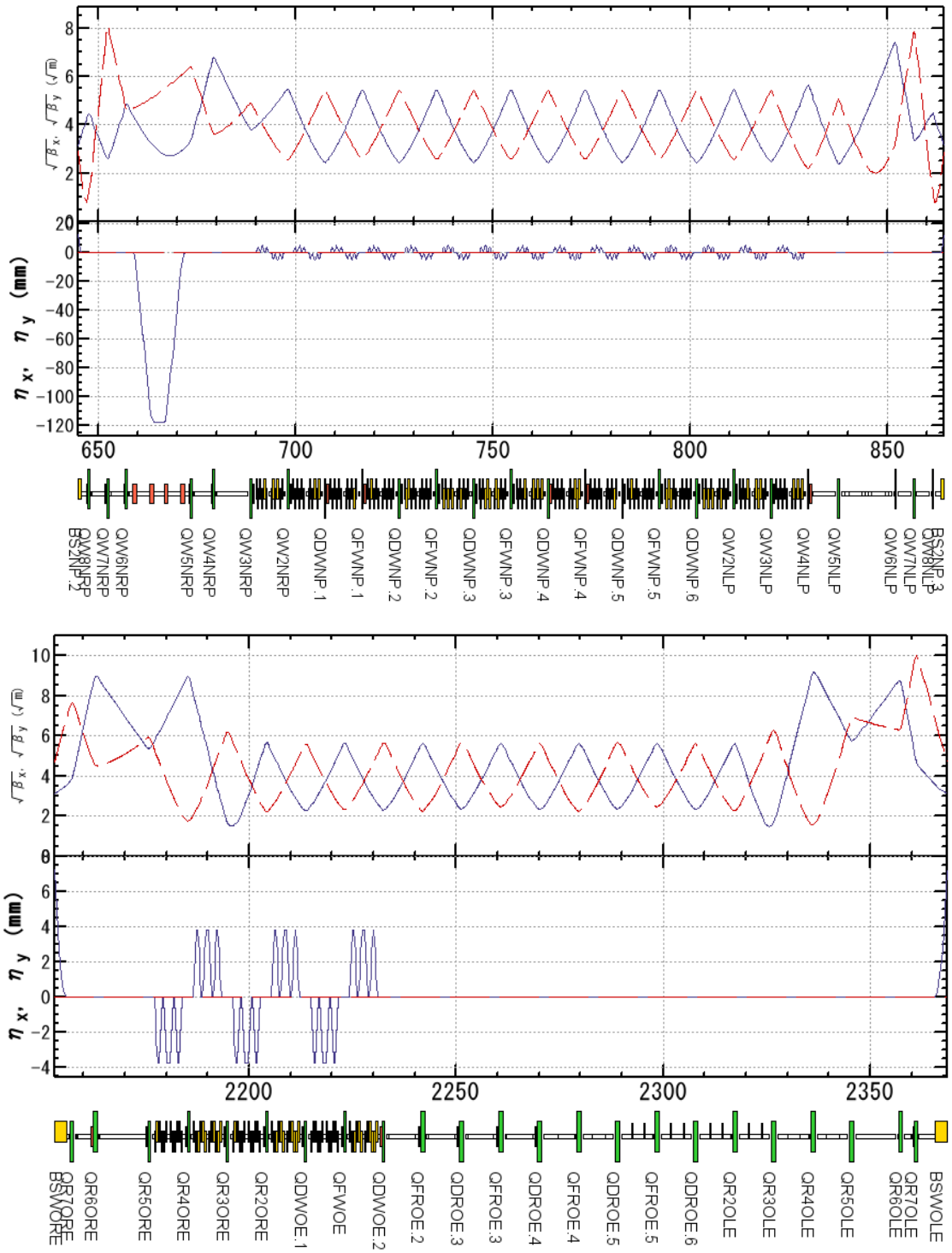

Figure 2.4: *Lattice design and optics of the wigglers section for LER (a) and HER (b).*

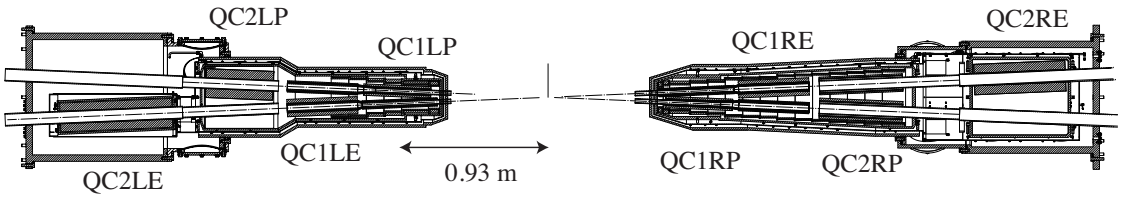

Figure 2.5: *Top view drawing of the SuperKEKB Final Focus system.*

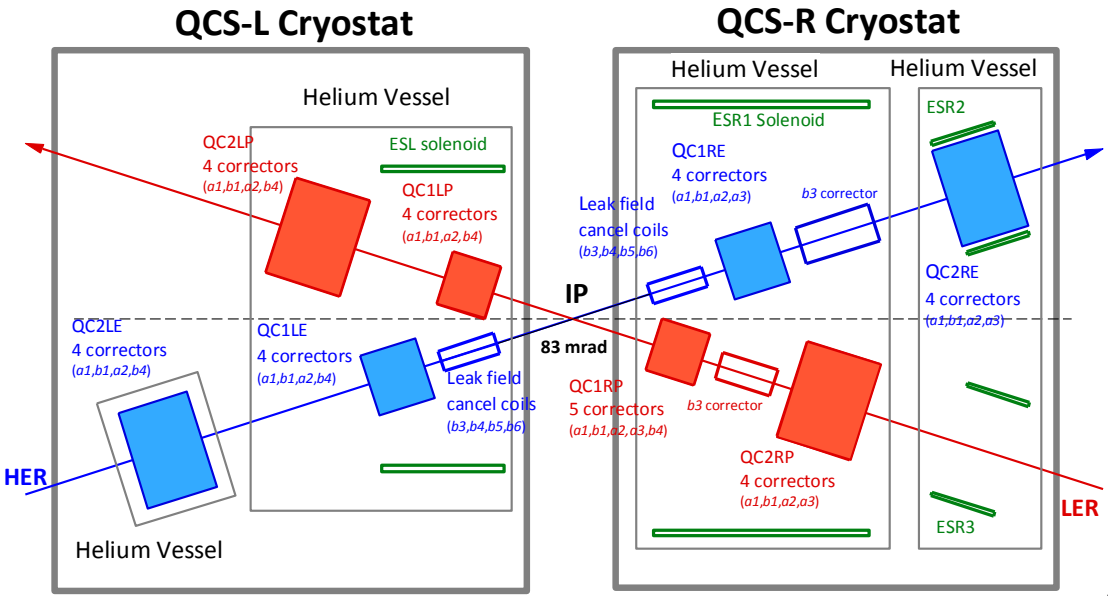

Figure 2.6: *SuperKEKB Final Focus system layout.*

Final Focus system

The Final Focus (FF) system has been designed to achieve an extremely low beta function at the IP. It's a very precise and complex system made of superconductive magnets. It consists of eight main quadrupoles, forty-three corrector magnets and four compensation solenoid coils, as shown in figs. 2.5 and 2.6. The main quadrupole magnets, QC1 and QC2, form a doublet for each beam. Every quadrupole has four or five corrector magnets, that are used to correct misalignments of the quadrupoles, adjust beam orbit and optimise dynamic aperture. QC1LP and QC1RP have no yokes, so their multipole components of leakage fields are canceled by corrector magnets on the HER beam line. Compensation solenoid coils are used to cancel the the Belle II 1.5 T solenoid magnetic field, so that $\int B_z ds = 0$ on each side of the IP. A rotation of FF magnets around the beam axis and skew quadrupole correctors are used to reduce as much as possible vertical dispersion and X-Y coupling. In addition, because of the crossing angle, beams axes are tilted with respect to the solenoid axis, causing an increase in the vertical emittance. Skew dipole correctors in QC1 and QC2 are used to adjust the vertical orbit to compensate this effect. The residual X-Y coupling and vertical dispersion are corrected using skew quadrupoles

and skew dipoles located between the FF and the Local Chromaticity Correction (LCC) sextupoles. The lattice design of the interaction region, that contains the FF system, is shown in fig. 2.7.

Local Chromaticity Correction

LCC consists of two identical sextupole magnets placed near the FF system, since approximately 80% of the natural chromaticity in the vertical direction is induced by the FF magnets. The transfer matrix between the two sextupoles is $-I'$ to compensate the non-linear kick due to the strong sextupole field. There are two kinds of sextupole magnets: one is for the vertical chromaticity correction, called Y-LCC, and the other is for the horizontal one, called X-LCC. The phase advance between QC1 and the Y-LCC is π in the vertical direction, while that between QC2 and X-LCC is 2π in the horizontal direction. Fig. 2.8 shows the lattice design of the LCC region.

Power supplies for the QCS magnets have very strict requirements: they must have high current stability, low current ripple, high current setting resolution and a quench protection system. Power supplies for QCS main magnets and corrector magnets were developed to meet these requirements. Tests on the full scale prototype of the power supply have shown a current stability within 1.9 ppm for 8 hours of operation, and that the output current decrease with a time constant of about 2.5 ms after a quench trigger signal was generated by a quench detector [13].

2.2.2 Vacuum system

Higher beam currents and the electron cloud effect set new requirements for the vacuum system of SuperKEKB: in positron and proton storage rings, electrons generated by photo-electric effect and ionization can accumulate in the beam pipe during multi-bunch operation, causing the formation of an "electron cloud" [14]. The production rate of photo-electrons depends on the synchrotron radiation and is many orders of magnitude higher that the production rate of electrons from ionization [15]. With LER parameters it takes just a few bunch passages until the number of electrons in the beam pipe, per unit length, is similar to the number of particles in a bunch. This electron cloud perturbs the beam causing instabilities, that in KEK were initially observed at the Photon Factory and then in the positron ring of KEKB. The observations in KEK included, among others, increase in vertical beam size, coupled oscillations, beam blow-up and a drop in specific luminosity. In SuperKEKB synchrotron power and photon density would be very high, especially in wigglers sections, and this would enhance the electron cloud effect, that must therefore be mitigated. In addition, the beam impedance of many components must

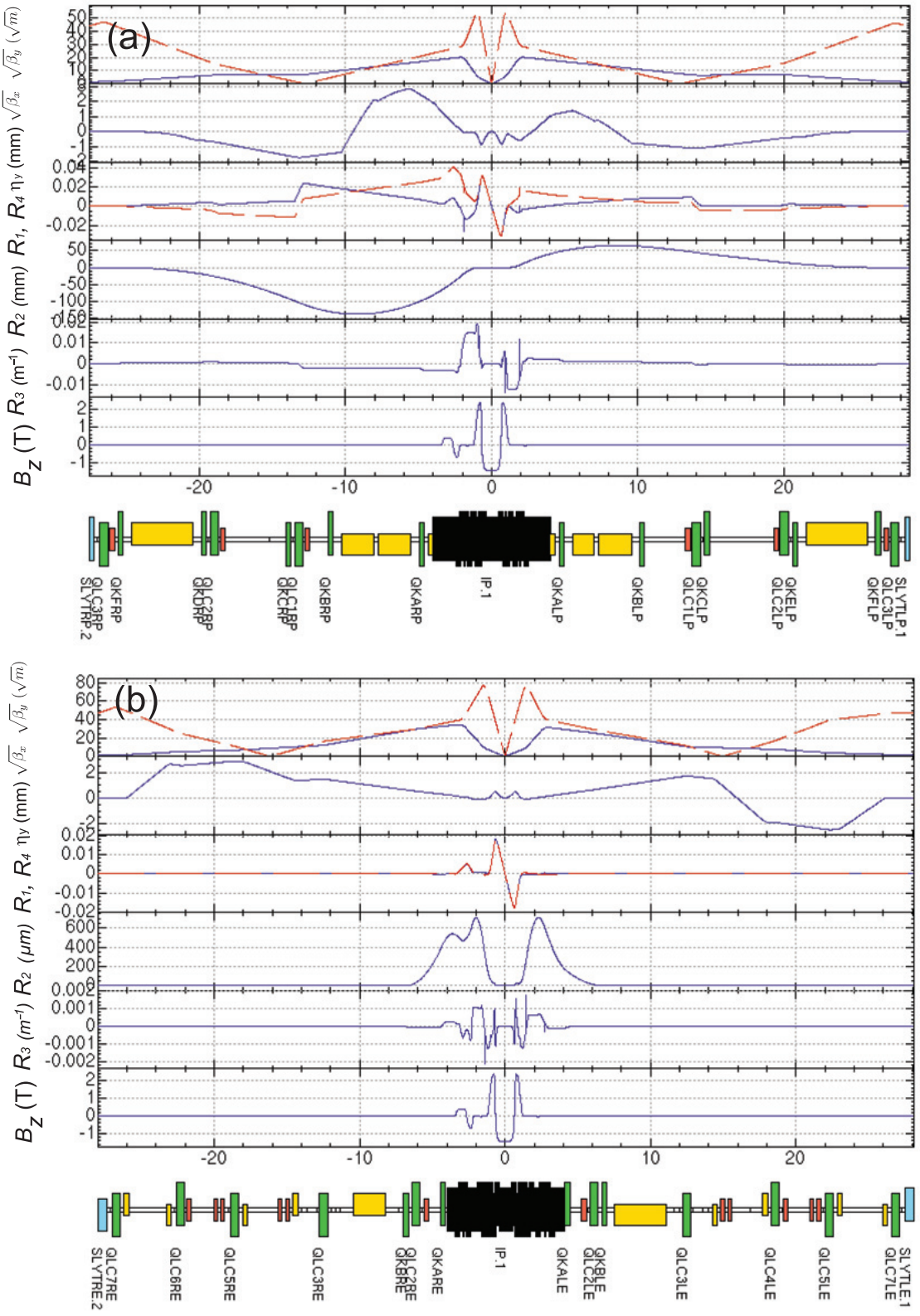

Figure 2.7: *Lattice design and optics of the interaction region for LER (a) and HER (b).*

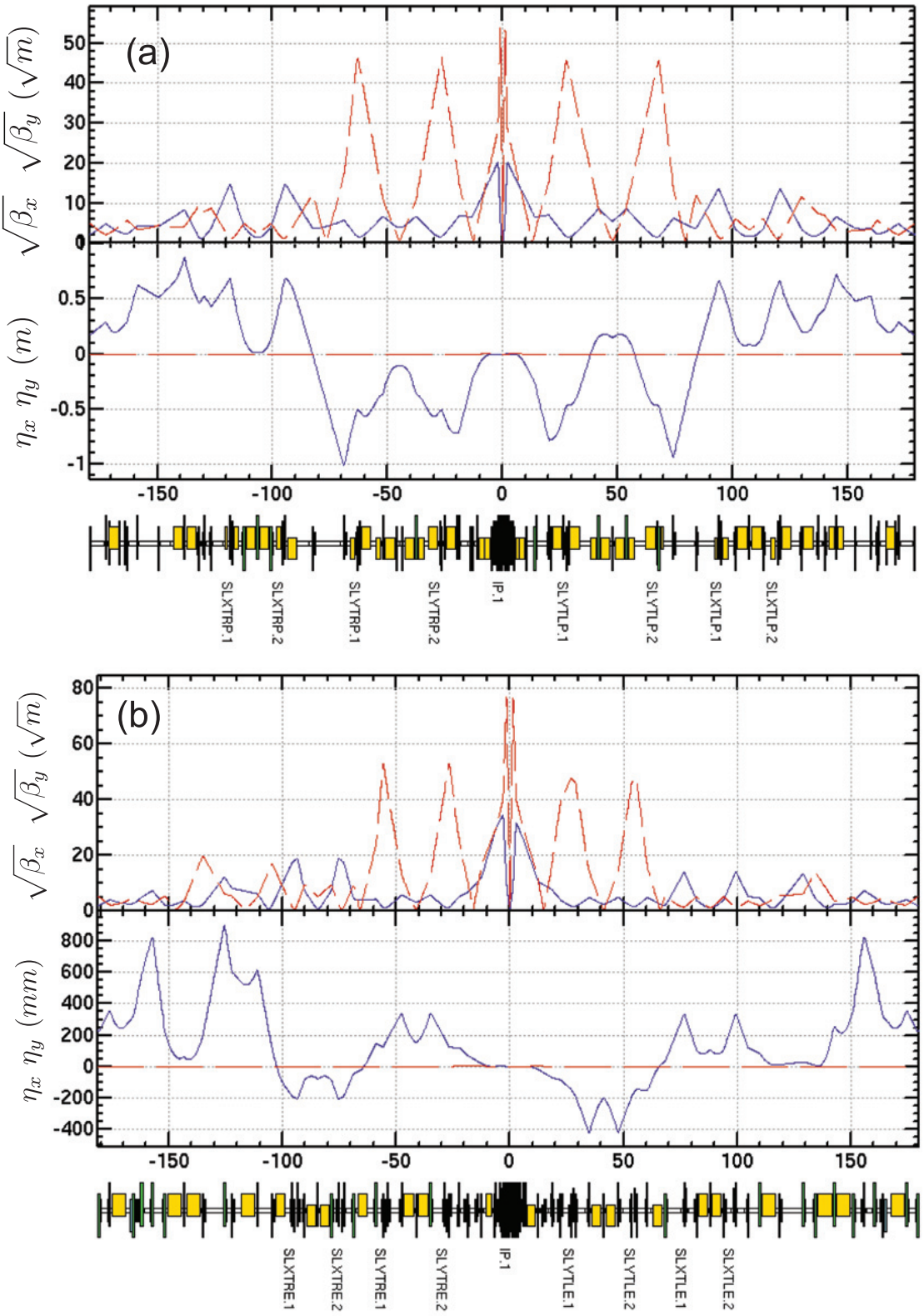

Figure 2.8: *Lattice design and optics of the local chromaticity correction section for LER (a) and HER (b).*

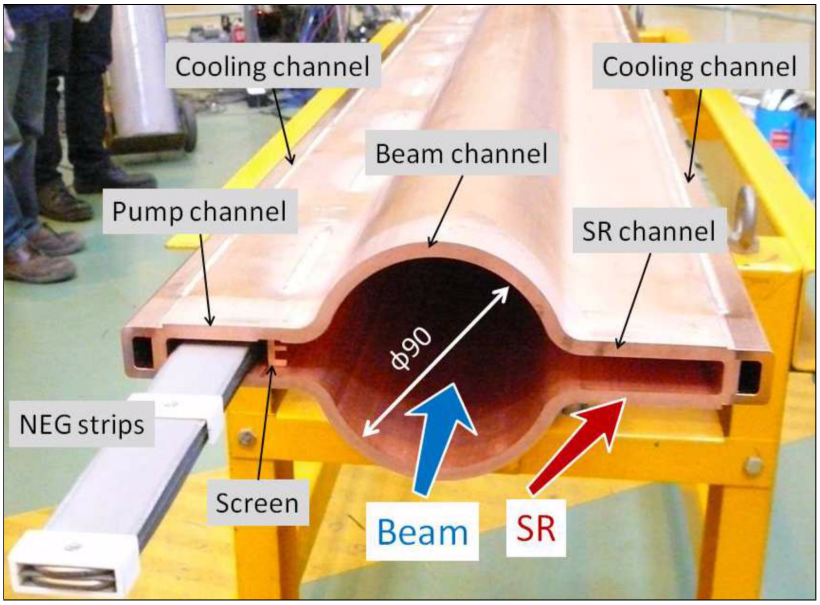

Figure 2.9: *Beam pipe with antechamber made of copper for the Tsukuba straight section.*

be minimised to suppress higher-order modes excitation.

One countermeasure adopted against the electron cloud effect is the use of antechamber beam pipes, together with bellow chambers with a "comb-type" RF shield structure to improve thermal strength. For a gapless connection and a highly reliable electric contact between these two components, a Matsumoto-Ohtsuka type (MO type) flange has been applied [16]. Bellows chambers, MO type flanges and gate valves have all cross-section with the same antechamber shape, to minimise impedance and heating due to beam-induced HOMs. Some of the new antechamber beam pipes were produced with aluminum coated with TiN [17], because they are easier to fabricate and have a lower cost. It was confirmed that an aluminum surface coated with TiN is as good as copper coated with TiN to suppress electron density due to multipactoring, the electron cloud density is approximately the same for both materials. Thus aluminum coated with TiN was adopted for new antechamber beam pipes in the LER arc sections. In both rings, beam pipes in the wiggler section, where the SR power is high, and in the Tsukuba straight section, where the contribution to the Belle II detector background is important, were replaced with antechamber beam pipes made of copper, shown in fig. 2.9. Beam pipes in the arc sections of the HER were reused.

There are also other countermeasures against the electron cloud effect: grooved surfaces and clearing electrodes were applied to dipole field regions. Beam pipes in the bending magnets in the arc sections were machined with grooves in the upper and lower inner surfaces. A method of forming a thin electrode on the inner surface using a thermal spray developed at KEK was applied to beam pipes in the wiggler magnets

[18]. Solenoid magnets and permanent magnets were installed already in KEKB to at least partially suppress the electron cloud effect. In addition, a new collimator for antechamber beam pipes was developed, based on the ones used in PEP II at SLAC, and two of them were installed before the start of Phase 1 commissioning. A more detailed description of this new type of collimator is given in section 3.4.2.

All these improvements to the vacuum system were tested successfully during the first commissioning run in 2016: new collimators worked as expected and the effectiveness of the antechambers and TiN coating of the beam pipes against electron cloud effect was confirmed [19].

2.2.3 RF system

If in KEKB coupled-bunch instabilities (CBIs) were a concern, in SuperKEKB the concern is even bigger. Longitudinal CBIs are caused by the accelerating mode of RF cavities, while the impedance of HOMs cavities can induce longitudinal and transverse CBIs. In KEKB two innovative heavily HOM-damped cavities with large stored energy were already used: the ARES cavity [28] and the Super Conducting Cavity (SCC) [29]. These cavities worked well for KEKB, but to be reused for SuperKEKB they needed reinforcements and improvements to meet the SuperKEKB beam parameters. In particular, in SuperKEKB currents are twice as much the KEKB ones while the RF voltage is about the same as that of KEKB. To increase the power delivered by ARES cavities, each cavity was coupled with one klystron, while in KEKB two ARES cavities were coupled to one klystron. With this one-to-one configuration, input couplers of the ARES cavities were upgraded to increase their power handling capability from 400 kW to over 700 kW.

Regarding SCC, the ferrite HOM dampers used in KEKB were considered marginal at around 2.0 A in the HER. To achieve the design beam current of 2.6 A in the HER, additional HOM dumpers made by SiC were installed between adjacent cavities, to reduce the HOM loads to existing ferrite dampers. The Q-factors of several SCCs were found to be severely degraded after the long-term operation in KEKB. To recover the cavity performance, a horizontal high pressure water rinsing system was developed and applied to cavities without disassembling them from their cryostat [30]. This method saves a lot of time and costs, and was applied already to some cavities, whose Q-factor recovered significantly.

2.2.4 Beam instrumentation and control systems

In KEKB both rings were equipped with beam position monitors (BPMs). In the LER of SuperKEKB, narrow-band detectors at 1 GHz for BPMs were replaced with new ones at 509 MHz, because the cut-off frequency of the new antechamber is lower

than 1 GHz. In the HER, where the old beam pipes were reused, the 1 GHz narrow-band detectors were also reused. New gated turn-by-turn detectors were developed and installed for BPMs at selected positions in both rings.

Two bunch-by-bunch feedback systems were developed in collaboration with SLAC and INFN [20]. The transverse bunch feedback system in LER and HER consists of position monitors, high speed signal processing using digital feedback filters, strip line kickers and wide-band high power amplifiers. The longitudinal feedback system with overdamped kickers was developed at DAΦNE and was implemented in the LER, together with a bunch current monitor (BCM) and a bunch oscillation recorder (BOR).

X-ray beam size monitors based on coded aperture imaging were developed for high-resolution, bunch-by-bunch measurement of small beam size [21]. They were installed in the LER and HER for vertical beam size measurements. Other beam monitoring systems include SR monitors for horizontal beam size measurement, streak cameras for bunch length measurement, a large angle bremsstrahlung monitor (LABM) [22] for measurement of polarisation components of radiation emitted by beam-beam collisions, and beam loss monitors. A collision feedback system was also prepared for the start of Phase 2 to maintain the optimal beam collision condition [23].

New control modules have been developed for the SuperKEKB control system, including upgraded version of power supply interface controller module for magnet power supplies, EPICS [24] embedded CPU module for programmable logic controller, and new event modules to deliver triggers to beam monitors at the damping ring. Beam abort system has been upgraded to protect the extract window against high beam current. The abort trigger system was also improved to achieve a faster response time, that is now of the order of 20 μs while in KEKB was of the order of 100 μs [25]. The beam abort system has also been improved integrating abort signals coming from diamond sensors installed around the beam pipe close to the interaction point. Diamond sensors, used to monitor the integrated radiation dose absorbed by the Belle II detector, can be used also to deliver a beam abort signal when the background conditions go beyond a set threshold. This additional abort signal was integrated in the beam abort system during Phase 2 commissioning not only to protect the detector against high background conditions, but also to prevent quenches of the FF superconductive magnets [26] [27]. With the experience of the first run of Phase 3 in 2019, where despite the fast beam abort signal delivered by diamond sensors a significant amount of radiation was delivered to the Belle II detector, a further reduction of the response time of the abort trigger system has been implemented.

2.3 Injection scheme in SuperKEKB

Beam injection will be an important background source for the Belle II detector, as will be discussed in section 4, so an overview of the injection system is given in this section.

Electron and positron beams are produced and treated in different ways. Electrons are produced with a new RF gun equipped with a high power laser and a Ir_2Ce photo cathode for high conversion efficiency; the target for operations with the final machine parameters is to produce high charge bunches of 5 nC with a small emittance. Electrons are accelerated up to 7 GeV and are directly injected into the HER. For the positrons, a thermionic gun is used to produce 10 nC bunches of electrons that are accelerated up to 3.2 GeV toward a 14 mm thick tungsten target from which positrons are produced. These positrons have a too large emittance to be injected directly in the main ring, so after being accelerated up to 1.1 GeV they are injected into the damping ring, where their emittance is reduced from 1.4 μm to 42.9 nm in the horizontal direction and from 1.4 μm to 3.12 nm in the vertical direction [6]. Positrons are then re-injected into the linac and accelerated to 4 GeV before being injected into the LER. In these scheme, electrons and positrons are accelerated with the same linac.

It is possible to distinguish between "normal" and "continuous" injection. The former is done manually by operators from time to time and is used to fill each ring up to the set current limit. The latter is performed automatically, setting the target current and the fraction of beam that is lost: when the beam current decreases by a certain (small) amount, a top-up injection is performed to bring the beam current to the limit, while collisions are still occurring. The need of using continuous injection comes from the short beam lifetimes expected for both beams, for which a normal injection operation would not be feasible. Continuous injection operation has been successfully tested for both beams during the first run of Phase 3 in 2019. With the use of continuous injection in SuperKEKB to keep a constant luminosity against the small beam lifetimes, the linac must be able to inject beams in LER and HER simultaneously, and to provide beams also to other facilities, like the Photon Factory (PF) and the Photon Factory Advanced Ring (PF-AR). For this reason the linac itself has been modified in order to behave as four independent accelerators, capable of injecting beams simultaneously into four different storage rings.

There are also two ways to technically perform injection: "*betatron phase-space injection*" and "*synchrotron phase-space injection*". Both are multi-turn injections, and they are done with a septum magnet that is used to merge the beams.

In the betatron phase-space injection two kickers are used to make an orbit bump of the stored beam in the horizontal direction, to bring the stored beam close

to the septum magnet. The injected beam is then steered into the stored beam to minimise the angle between the trajectories of injected and stored beams. Due to the finite width of the septum, the angle cannot be zero, so the injected beam will perform betatron oscillations around the stored beam, that are eventually damped by synchrotron radiation and bunch-by-bunch feedback system. The transverse damping time has been evaluated in 43 ms for the LER and 58 ms for the HER. The maximum repetition rate of the injection is 25 Hz, that correspond to a time interval of 40 ms, comparable with the damping time of the injected beam betatron oscillation. In addition, the injected beam performs coherent oscillations in the horizontal direction that shifts longitudinally the interaction point, which implies that the injected beam collides with the opposite beam at a larger beta function due to the hourglass effect, and receives a vertical kick. One possible solution could be the crab waist scheme, in which the waist position of the injected beam is adjusted by a kick from crab sextupoles magnets, so that in the collision point both beams are at their waist, but the use of crab waist sextupoles reduces significantly the dynamic aperture limiting the machine operation. During commissioning and the first run in 2019, beam lifetimes were not so small as it is expected with final machine parameters, so a lower injection rate was used and even in continuous injection mode there were minutes between one injection and the next, so the effects of betatron phase-space injection were somehow mitigated, but with the machine running at design parameters, this could be an important source of background or a limitation to instantaneous luminosity.

To overcome the difficulties of the betatron phase-space injection, the synchrotron phase-space injection is considered. Also in this case kickers are used to make a local bump orbit to bring the beam close to the septum magnet, then particles are injected with a negative energy offset δ_0 that should be within the momentum acceptance of the stored beam. The distance between the injected and the stored beam in the injection point is given by:

$$\Delta x = \eta_x \delta_0 \tag{2.15}$$

where η_x is the dispersion, so this means that the optics has to be changed introducing non-zero dispersion at the injection point. By adjusting the septum, the beam can be injected parallel to the circulating beam, it will follow the closed orbit of circulating particles and it will have the given energy offset. Hence the injected beam, having no angle with the stored beam, will not perform betatron oscillations around it. The injected beam instead will oscillate in the longitudinal plane at the synchrotron tune (ν_s) and slowly damp into the circulating beam. The main advantage of synchrotron injection is that there are no injection oscillations in the straight sections, where the dispersion is zero. At LEP it has been observed that

longitudinal oscillations damping time is a factor 2 lower than transverse oscillations damping time, and that transverse oscillations of beams injected with synchrotron phase-space injection are smaller and follow the dispersion function [31]. Given the betatron function of the stored beam at the injection point and the septum thickness, it is possible to evaluate the necessary dispersion as a function of the betatron function of the injected beam, in order to satisfy the condition 2.15. This kind of injection has not been tried yet in SuperKEKB, because the non-zero dispersion requires modifications in the machine optics and the momentum acceptance of the ring should be large enough, but it will be taken into consideration if drawbacks of betatron phase-space injection will become severe.

2.4 SuperKEKB commissioning and operation

The commissioning of SuperKEKB was divided into three different phases:

- **Phase 1** - It was performed between February and June 2016. The upgrades in the lattice of the machine were completed, but the final focus system was missing. The beams were kept separated even in the interaction region, so no collisions happened. The Belle II detector was not positioned around the interaction point, it was still under construction.

- **Phase 2** - Performed between February and July 2018. The final focus system was in place and the interaction region assembly was finalised. Additional collimators were installed in LER. Also the damping ring was commissioned during Phase 2. The detector was rolled in around the interaction point, with all sub-detectors assembled except the VXD, of which only a small slice in the horizontal plane was installed. The remaining part of the VXD volume was instrumented, as shown in fig 2.10, with part of the BEAST II detector system, designed to measure the machine induced background on the Belle II detector. Inside the VXD volume, BEAST II detectors were:

  - FANGS: hybrid silicon pixel detectors.
  - CLAWS: plastic scintillators with SiPM readout.
  - PLUME: two-layers CMOS pixel sensors.

  while outside the VXD volume other BEAST II detectors were used:

  - Diamond sensors for ionizing radiation dose monitoring in the interaction region (used also for the beam abort system).
  - PIN diodes for ionizing radiation dose monitoring around QCS magnets.

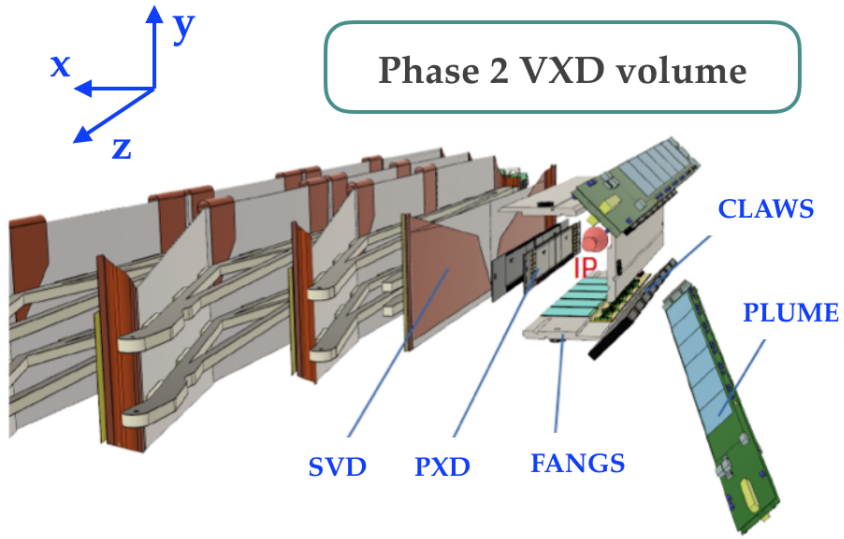

Figure 2.10: *Detectors inside the VXD volume during Phase 2 operations.*

  - ^{3}He detectors for thermal neutron flux measurements.
  - TPC detectors for fast neutron flux and direction measurements.

  First collisions happened on April 26th. From the detector point of view, the purpose of the Phase 2 operation, together with the commissioning of SuperKEKB in its final configuration, was to verify that the level of backgrounds in the interaction region were compatible with the expectations.

- **Phase 3** - The first Phase 3 run started in February 2019 with detector operation, while the machine started on March 11th, quickly resuming operations with the same optics used in the end of Phase 2. The Belle II detector was in its final configuration, with the full VXD installed in November 2018, while the machine was essentially the same as in Phase 2, with one additional horizontal collimator installed in the HER and four additional collimators installed in the LER (one vertical and three horizontal). Operations lasted until July 2nd, with an interruption of about 4 weeks due to a fire accident developed near the Linac building. The first Phase 3 run is also called "early Phase 3" run, and so it will be referred throughout the rest of the document.

Table 2.2 shows the achievements in the main machine parameters for the Phase 2 and early Phase 3 runs. Parameters are referring to stable operations that were used for physics run and/or for background studies. Achievements reached only during machine studies are not reported, with the exception of the delivered luminosity, that was reached by the machine, but with the Belle II detector turned OFF.

The main achievement in Phase 2 was the verification of the nano-beam scheme, as well as first collision with the machine in its final configuration. The vertical beta

Parameter	Units	Phase 2		Early Phase 3	
		LER	HER	LER	HER
β_x^*	mm	200	100	200	100
β_y^*	mm	3	3	3	3
n_b		789		1576	
I	mA	340	285	650	600
ε_x	nm	2.1	4.6	2.1	4.6
ε_y	pm	160	85	85	55
σ_x^*	μm	20	21	20	21
σ_y^*	nm	700	500	500	400
ξ_y		0.0277	0.0186	0.0266	0.0165
ε_x	nm	1.7	4.6	1.7	4.6
L (recorded)	$\mathrm{cm}^{-2}\mathrm{s}^{-1}$	2.5×10^{33}		5.5×10^{33}	
L (delivered)		2.5×10^{33}		1.23×10^{34}	
$\int$L	fb$^-$1	0.5		6.5	

Table 2.2: *Comparison between the achieved SuperKEKB parameters at the end of Phase 2 and at the end of the first run of Phase 3.*
The "recorded" luminosity has been achieved with the Belle II detector ON taking physics data, while the "delivered" luminosity has been achieved by the machine, but with the Belle II detector OFF.

function was squeezed as planned, reaching a value of $\beta_y^* = 3$ mm for both beams, already a factor 2 better than the nominal vertical beta function in KEKB. All horizontal collimators were studied, and together with the diamonds abort system they were able to significantly reduce the number of QCS quenches in the last part of Phase 2. The damping ring was successfully commissioned and operated.

In early Phase 3 collisions were quickly resumed in March 2019, and the collision scheme at $\beta_y^* = 3$ mm was verified and used for most of the physics runs. There were two big achievements during early Phase 3: a big reduction of injection background, and, as a consequence, the use of continuous injection for both beams, that allowed the Belle II detector to collect 6.5 fb^{-1} of data, limited mostly by the fire accident that caused the machine to be OFF for four weeks.

Chapter 3

Collimation in high energy colliders and in SuperKEKB

3.1 General concept of beam halo and collimation

Particle beams in accelerators are characterized by a high-density particle distribution, called "beam core", and a low-density particle distribution called "beam halo". The latter is composed by particles with a large betatron amplitude or with a large momentum error, and their beam dynamics behaviour is quite different from the beam core. Beam halo particles can be lost, hitting accelerator components. This can cause beam quality degradation, activation or damage of accelerator components, and beam induced background on particle detectors, whose lifetime and performance can be seriously affected. There are many reasons for beam halo formation: beam-gas scattering and intra-beam scattering, that will be described in section 4, collective instabilities like wakefields, that will be described in section 3.2, and optics related effects, like optics mismatches, dispersion, magnet field errors due to small misalignments and power supply jitter. In general, the particle distribution in the beam halo is not known and it's different in every machine. Usually the beam core for a Gaussian particles distribution is considered to be around $\pm$3-4 σ, therefore particles outside this interval can be considered as part of beam halo, but for high intensity beams the definition based on Twiss parameters or beam size is not enough. In the case of high intensity beams, which are space charge dominated, another definition of beam halo has been proposed [32], using parameters like the "percentage of halo particles" or the "percentage of halo size" that better describe the importance and the evolution of a high intensity beam.

In any case, controlling the effects of beam halo is essential to assure safety and performance of the machine and the detectors. The main purpose of a collimation system is to reduce the beam induced background created in the interaction region,

to protect the detector from synchrotron radiation and from EM showers produced by lost particles that hit accelerator components. The design of a collimation system is a compromise between different parameters: the location inside the machine depending on the optics parameters, the aperture that should clean efficiently the beam halo without introducing wakefields or other instabilities, the re-generation of beam halo due to scattering on the collimators, the robustness of collimators absorbing material.

An important parameter of a collimation system is the "*collimation depth*", which determines the physical aperture of a collimator. The collimation depth depends on the transverse position of halo particles, that in general is given by a betatron component and a dispersion component, as for the geometric beam size definition. The collimation depth is defined as the transverse half aperture in units of the transverse beam size:

$$n_{x,y}(s) = \frac{a_{x,y}}{\sigma_{x,y}(s)} = \frac{a_{x,y}}{\sqrt{\beta_{x,y}(s) \cdot \varepsilon_{x,y} + (\eta_{x,y}(s) \cdot \sigma_\delta)^2}} \tag{3.1}$$

The denominator of the r.h.s. of equation (3.1)is the definition of the beam size:

$$\sigma_{x,y}(s) = \sqrt{\beta_{x,y}(s) \cdot \varepsilon_{x,y} + (\eta_{x,y}(s) \cdot \sigma_\delta)^2} \tag{3.2}$$

where $\beta_{x,y}$ is the betatron function, $\varepsilon_{x,y}$ is the beam emittance, $\eta_{x,y}$ is the dispersion function, that represents the variation in the deflection of a particle in a magnetic or electric field due to the energy spread σ_δ of a particle, defined as ΔE/E. Thus the product $\eta \cdot \sigma_\delta$ is the offset of the reference trajectory from the ideal path for particles that have a relative energy deviation from the ideal energy. The dispersion depends on the longitudinal coordinate s and in general is defined for both horizontal and vertical directions, but because of bending dipoles acting only in the horizontal direction, the dispersion is orders of magnitude higher in the horizontal plane, and vertical dispersion is usually neglected.

The first term of the r.h.s. of equation (3.2) is the betatron component, while the second term is the dispersion component. Particles in the beam halo will have a large betatron amplitude with respect to the reference orbit or a large energy deviation with respect to the nominal energy. In general, two collimation systems are required to absorb these two kind of halo particles: the "*betatron collimation system*" and the "*energy collimation system*". The specific characteristics of these two systems will be described in the following paragraphs. Collimation systems can be different depending on the type of accelerator: in linear colliders, a collimation system is usually made by couples of spoilers and absorbers, the former with the function of increasing the angular divergence of halo particles by Coulomb scattering to

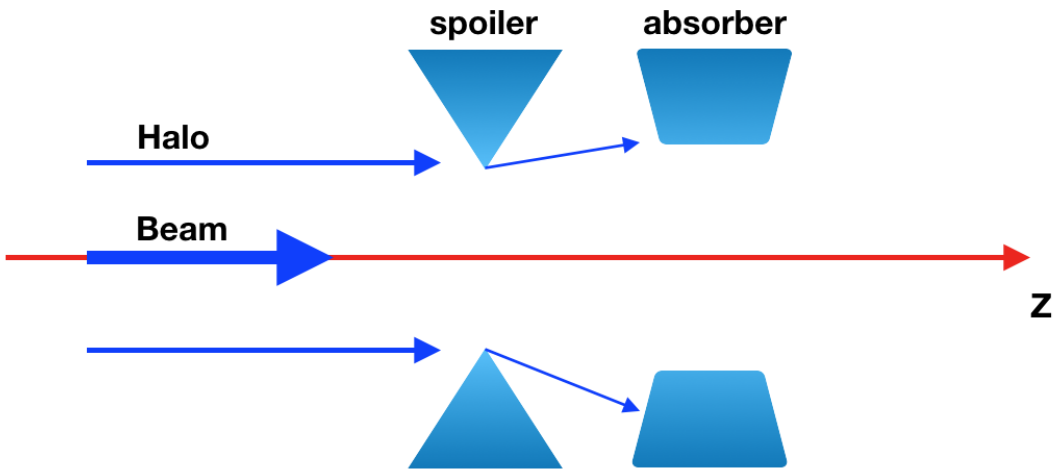

Figure 3.1: *Scheme of a typical collimation system in a linear accelerator.*

decrease the transverse density of particles, the latter with the function of absorbing the halo particles minimizing the emission of secondary particles. An example of a spoiler/absorber system is shown in fig. 3.1. In circular colliders beams pass through collimators at every turn, and the collimation system is a multi-stage system made of many collimators, where the first collimator can absorb halo particles and the downstream ones are used to absorb the secondary halo particles produced by Coulomb scattering in the first collimator. A scheme of a collimation system for circular colliders is shown in fig. 3.2.

3.1.1 The betatron collimation system

The betatron collimation system is responsible of reducing the betatron transverse component of the beam halo. As anticipated in the previous paragraph, for this collimation system the "*betatron collimation depth*" is a very important parameter. In equation (3.1) the general expression for the beam size (3.2) was used, but a pure betatron collimation system is located in a region where the dispersion is negligible in order to collimate only the geometric component of the beam halo, so the dispersion term in the square root of the beam size expression can be omitted and equation (3.1) becomes:

$$n_{x,y} = \frac{a_{x,y}}{\sigma_{x,y}} = \frac{a_{x,y}}{\sqrt{\beta_{x,y}(s) \cdot \varepsilon_{x,y}}} \tag{3.3}$$

The betatron collimation depth can be considered as the aperture needed to avoid that synchrotron radiation photons produced by halo particles, or halo particles themselves, are intercepted by the interaction region components with the smallest aperture.

For collimators, a location with high $\beta_{x,y}$ is preferable, because the beam size

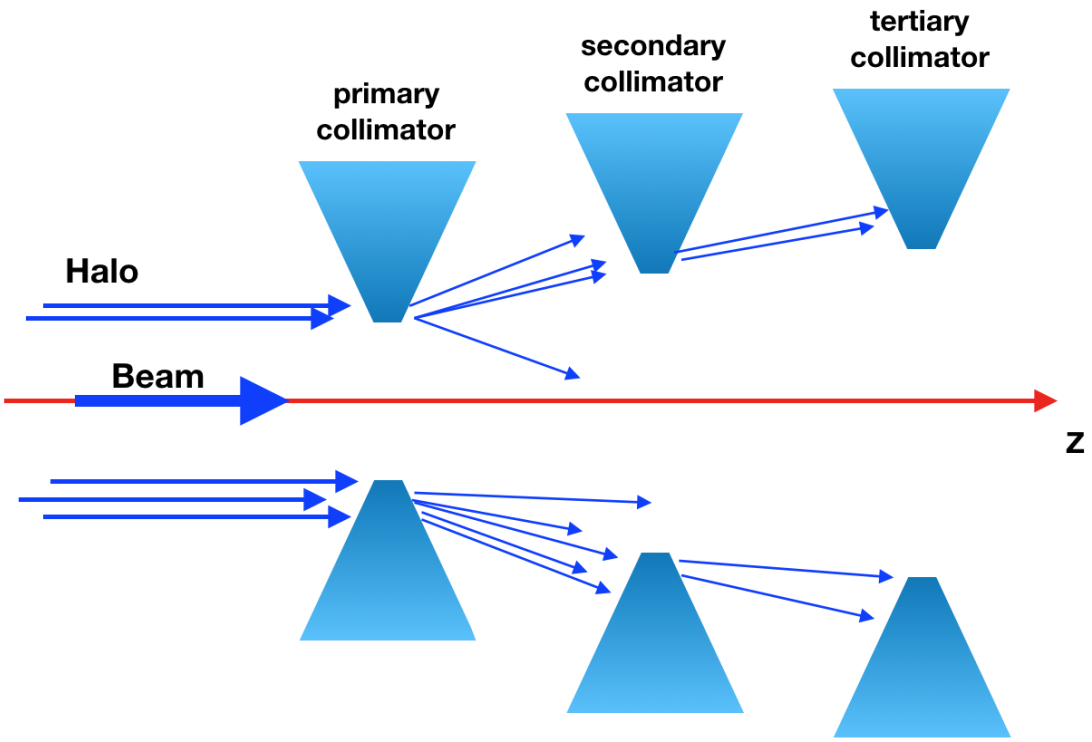

Figure 3.2: *Schematic collimation system in a circular accelerator.*

would be larger and the same collimation depth would be achieved with a larger collimator aperture, which induces smaller wakefields, as it will be explained in section 3.2. Moreover, a larger beam size implies a lower particle density interacting with the material of the collimator, which is better for the safety of the collimator itself.

An estimation of the betatron collimation depth and of the position of collimators in the machine can be done using the transport matrix formalism, as follows. Let's consider a circular accelerator, only one dimension in the phase space, halo particles on energy, so with $\sigma_\delta = 0$, and two collimators, the primary and the secondary ones; let n_1 and n_2 be the apertures of the two collimators, expressed in units of the transverse beam size; let $\boldsymbol{X_0} = (X_0, X_0') = (n_1, 0)$ be the transverse amplitude vector of the beam halo, with X_0 and X_0' being the normalized horizontal amplitude and divergence: $X_0 \equiv x_0/\sqrt{\beta_{x,0}\varepsilon_x}$ and $X_0' \equiv (\alpha_{x,0}x_0 + \beta_{x,0}x_0')/\sqrt{\beta_{x,0}\varepsilon_x}$, where α_x is the Twiss parameter defined as $\alpha_x = -\beta_x'/2$. Here the divergence is zero because it is assumed that the impact point of particles is the surface of the collimator jaw. It is also assumed that the optics in the region between the collimators is linear and uncoupled. When particles hit the surface of the collimator head, they receive an angular kick so that $X_1' = K$. Thus the new coordinates after the interaction of halo particles with the collimator are given by $\boldsymbol{X_1} = (n_1, K)$. The secondary collimator is placed downstream the primary one, and at its location the coordinate vector can

be derived using the transport matrix written as a function of the Twiss parameters at the two collimators locations:

$$\boldsymbol{X_2} = \boldsymbol{R}(\Delta\mu)\boldsymbol{X_1} \tag{3.4}$$

where $\Delta\mu$ is the phase advance between the two collimators. The general expression of $\boldsymbol{R}(\Delta\mu)$ is given by:

$$\boldsymbol{R}(\Delta\mu) = \begin{bmatrix} \sqrt{\frac{\beta_{x,2}}{\beta_{x,1}}}(cos\Delta\mu_x + \alpha_{x,1}sin\Delta\mu_x) & \sqrt{\beta_{x,2}\beta_{x,1}}sin\Delta\mu_x \\ \frac{(\alpha_{x,1}-\alpha_{x,2})\Delta\mu_x-(1+\alpha_{x,1}\alpha_{x,2})sin\Delta\mu_x}{\sqrt{\beta_{x,2}\beta_{x,1}}} & \sqrt{\frac{\beta_{x,1}}{\beta_{x,2}}}(cos\Delta\mu_x - \alpha_{x,1}sin\Delta\mu_x) \end{bmatrix} \tag{3.5}$$

Considering that X_0 and X_0' are normalized to $\sqrt{\beta_x\varepsilon_x}$ and that the collimators are at a location where β_x is maximum, so that $\alpha_x = 0$, the expression of $\boldsymbol{R}(\Delta\mu)$ becomes:

$$\boldsymbol{R}(\Delta\mu) = \begin{bmatrix} cos\Delta\mu_x & sin\Delta\mu_x \\ -sin\Delta\mu_x & cos\Delta\mu_x \end{bmatrix} \tag{3.6}$$

From equations (3.4) and (3.6) it follows that:

$$X_2 = cos\Delta\mu_x X_1 + sin\Delta\mu_x X_1' \tag{3.7}$$

As described in [33], it's possible to choose the phase advance $\Delta\mu$ to minimize the halo amplitude escaping from the second collimator, and this happens when:

$$\Delta\mu = \arccos\left(\pm\frac{n_1}{n_2}\right) \tag{3.8}$$

In other words, once n_1 and n_2 are fixed, $\Delta\mu$ is the phase advance at which the secondary collimator should be placed to minimize the halo particles escaping from it.

So far n_2 has been considered as the aperture of the secondary collimator. Let's assume that n_2 is not the aperture of a collimator, but the aperture of a machine component, that could be for instance the beam pipe in the superconductive magnets of the final focus system in SuperKEKB. In this case, the aperture n_2 is fixed, and equation (3.8) can be used to find the optimal phase advance to place the primary collimator in order to shadow the beam pipe from halo particles. Setting $n_1 = n_2$, that means setting the collimator width as the aperture of the beam pipe, from equation (3.8) the result is that:

$$\Delta\mu = n\pi \tag{3.9}$$

Placing a collimator at a phase advance $\Delta\mu = n\pi$ is the best choice to protect a machine component that has the same aperture of the collimator jaws. In this

example n_2 is the required collimation depth for the collimation system.

The minimum kick that particles should get from the primary collimator to be absorbed by the secondary collimator is given by [33]:

$$K_c = \sqrt{n_2^2 - n_1^2} \tag{3.10}$$

3.1.2 The energy collimation system

The energy collimation system is required to reduce also the dispersion component of beam halo. The energy collimation depth is therefore defined using equation (3.1), keeping the dispersion term that is neglected in the case of the betatron collimation depth:

$$n_{x,y} = \frac{a_{x,y}}{\sigma_{x,y}} = \frac{a_{x,y}}{\sqrt{\beta_{x,y}(s) \cdot \varepsilon_{x,y} + (\eta_{x,y}(s) \cdot \sigma_\delta)^2}} \tag{3.11}$$

Clearly the energy collimation system has to be placed in a region where the dispersion is not negligible. Considering again a two collimators system with apertures n_1 and n_2, it would be preferable to place the first collimator where the dispersion is maximum and dominates with respect to the betatron component. Also for this case, the transport matrix formalism can be used to estimate the collimation depth. The equation (3.4) is still valid, but this time the dispersion contribution has to be considered, so $\boldsymbol{R}(\Delta\mu)$ becomes a 3×3 matrix:

$$\boldsymbol{R}(\Delta\mu) = \begin{bmatrix} cos\Delta\mu_x & sin\Delta\mu_x & \eta_{x,2} \\ -sin\Delta\mu_x & cos\Delta\mu_x & \eta'_{x,2} \\ 0 & 0 & 1 \end{bmatrix} \tag{3.12}$$

where also η_x and η'_x are normalized to the beam size. The transverse coordinate vector now has three components: $\boldsymbol{X_0} = [X_0, X'_0, (\Delta p/p)_0]$. Using equation (3.4), the amplitude at the second collimator becomes:

$$X_2 = cos\Delta\mu_x X_1 + sin\Delta\mu_x X'_1 + \eta_{x,2}(\Delta p/p)_1 \tag{3.13}$$

which is similar to equation (3.7), with an additional dispersion term. Let σ_δ be a relative momentum deviation, and n_b the betatron amplitude component at the same location. The normalized dispersion at the first collimator satisfies the following equation:

$$\eta_x \sigma_\delta + n_b = n_1 \quad \Longrightarrow \quad \eta_x = \frac{n_1 - n_b}{\sigma_\delta} \tag{3.14}$$

Considering a two collimators system, as done in the previous paragraph, after passing through the first collimator, particles receive a transverse kick, with the largest angle that passes beyond the secondary collimator given by the kick written

in equation (3.10). The largest betatron amplitude that goes through the secondary collimator is given by [33]:

$$A_x^{max} = \sqrt{X_2^2 + X_2'^2} = \sqrt{(n_1 - \eta_x \sigma_\delta)^2 + K_c^2} \tag{3.15}$$

so A_x^{max} represents the required energy collimation depth to absorb particles with dispersion η_x at the primary collimator.

Similarly to what has been said for pure betatron collimation systems, the optimal position for the energy collimation system would be where both betatron function and dispersion are close to a maximum, so that beam halo could be intercepted with a wider collimator aperture, that induces smaller wake fields at the collimators jaws.

3.1.3 Collimation efficiency

It's possible to quantify the efficiency of a collimation system defining the "*single collimation system efficiency*", η^i, as the ratio between halo particles absorbed by the collimation system and the total losses in the ring:

$$\eta^i = \frac{N^i}{N_{tot}} \tag{3.16}$$

If there are many collimation systems in a ring, the "*total collimation system efficiency*" is the ratio between the sum of the particles absorbed by all collimation systems and the total losses in the ring:

$$\eta^{tot} = \frac{\sum_i N^i}{N_{tot}} \tag{3.17}$$

Another parameter that is possible to define is the "*local collimation efficiency*":

$$\eta^i_{loc} = 1 - \frac{N^i_{coll}}{N^i_{no-coll}} \tag{3.18}$$

where N^i_{coll} are the particles lost for a given background source with the collimation system in place, while $N^i_{no-coll}$ are the particles lost for the same background source without the collimation system, or, more practically, with the collimator fully open.

3.2 Wake field effect in collimation systems

When charged particles travel across accelerator components, they induce electromagnetic fields. If the accelerator beam pipe was perfectly smooth and conductive, there would be no electromagnetic fields induced on the structure, but if the beam

pipe walls have a finite resistance or if there is a subtle change in the shape of the beam pipe, such fields are induced in the structure and can influence next bunches. Studying these fields would require to solve Maxwell's equations in a given structure using the beam current as the source of the fields, and this, depending on the component traversed by beam particles, could result to be quite complex. Because of the complexity of the equations to be solved, computer codes have been developed to solve the problem numerically. The effect of induced EM fields is a change in particles energy that can cause significant modifications in the dynamics of particle motion, leading to beam instabilities that must be understood and mitigated as much as possible.

In general, self-induced EM fields acting on a beam particle depend on the whole charge distribution. However, knowing the fields in a given structure generated by a single charge and using the superposition principle, it's possible to reconstruct the fields produced by any charge distribution. Let q_0 be a charge traveling at the speed of light with its trajectory parallel to the axis of the accelerator structure, and let q be a test charge moving at the same velocity on a trajectory parallel to the one of q_0. If $\boldsymbol{E}$ and $\boldsymbol{B}$ are the electric and magnetic fields generated by q_0, the Lorentz force acting on q is [34]:

$$\boldsymbol{F} = q\big[E_z\hat{z} + (E_x - vB_y)\hat{x} + (E_y + vB_x)\hat{y}\big] \equiv \boldsymbol{F}_{\shortparallel} + \boldsymbol{F}_{\perp} \tag{3.19}$$

where $\boldsymbol{F}_{\shortparallel}$ is a longitudinal force that changes the energy of q, while $\boldsymbol{F}_{\perp}$ is the transverse force that deflects its trajectory. The integral of these two forces over the length L of the structure gives the energy change of the particle q due to the fields generated by q_0. Normalizing the energy change to the charges q and q_0, the expressions of the so called longitudinal and transverse "*wake fields*" are obtained [34]:

$$\text{Longitudinal wake field}\big[V/C\big] \qquad w_{\shortparallel}(z) = -\frac{1}{qq_0}\int_0^L F_{\shortparallel}\mathrm{d}s \tag{3.20}$$

$$\text{Transverse wake field}\big[V/Cm\big] \qquad w_{\perp}(z) = \frac{1}{r_0}\frac{1}{qq_0}\int_0^L F_{\perp}\mathrm{d}s \tag{3.21}$$

where the minus sign in equation (3.20) means that q loses energy under the influence of a positive wake field generated by q_0, and r_0 in equation (3.21) is the transverse position of q_0 with respect to the reference orbit. For the transverse case, a positive wake field corresponds to a defocusing force. The effect of the whole charge distribution in a bunch on the test particle would be given by the integral of the wake fields of equations (3.20) and (3.21) multiplied by the longitudinal charge distribution $\rho(z)$:

$$W_{\shortparallel}(z) = \int_{-\infty}^{+\infty} w_{\shortparallel}(z)\rho(z)\mathrm{d}z \tag{3.22}$$

$$W_{\perp}(z) = \int_{-\infty}^{+\infty} w_{\perp}(z)\rho(z)\mathrm{d}z \tag{3.23}$$

In the last equations it is assumed that, for the causality principle, the wake fields are null for particles behind the test particle, which is affected by the field generated by the particles ahead. The last step is to understand the effect of the wake fields generated by the entire charge distribution in a bunch on the whole bunch itself. So the wake fields of equations (3.22) and (3.23), multiplied by the charge distribution, must be integrated again, to obtain finally:

$$k_{\shortparallel}(z) = \int_{-\infty}^{+\infty} W_{\shortparallel}(z)\rho(z)\mathrm{d}z \tag{3.24}$$

$$k_{\perp}(z) = \int_{-\infty}^{+\infty} W_{\perp}(z)\rho(z)\mathrm{d}z \tag{3.25}$$

$k_{\shortparallel}$ and $k_{\perp}$ are called, respectively, "*longitudinal loss factor*" and "*transverse kick factor*". It is possible to define the loss and kick factors for the full ring of an accelerator, or for a specific component in a beam line. For example, beam collimators may have movable jaws, that represent a change in the structure of the vacuum components traversed by beams, so wake fields are induced on the jaws, whose loss and kick factors will depend on their aperture. The knowledge of these factors is important to determine possible instabilities induced to the bunches, and possible heating effect which become significant since the higher order modes are deposited in vacuum chamber components in the form of heat.

Wake fields are used to study beam dynamics in the time domain. Switching to the frequency domain, the Fourier transforms of the wake fields are called "*coupling impedances*" and are given by [34]:

$$\text{Longitudinal impedance}\big[\Omega\big] \qquad Z_{\shortparallel}(\omega) = \frac{1}{v}\int_{-\infty}^{\infty} w_{\shortparallel}(z)e^{i\frac{\omega z}{v}}\mathrm{d}z \tag{3.26}$$

$$\text{Transverse impedance}\big[\Omega/m\big] \qquad Z_{\perp}(\omega) = -\frac{1}{v}\int_{-\infty}^{\infty} w_{\perp}(z)e^{i\frac{\omega z}{v}}\mathrm{d}z \tag{3.27}$$

In frequency domain, all vacuum chamber components can be characterized by impedances. There can be a strong coupling between each of these components and the vacuum chamber, if the impedance and the beam have a significant component at the same frequency. The induced voltage $V(\omega)$ from this interaction is proportional to the bunch current $I(\omega)$, with the impedance $Z(\omega)$ being the proportionality factor that describes the coupling between the beam and the test particle through the vacuum chamber [41]:

$$V(\omega) = -Z(\omega)I(\omega) \tag{3.28}$$

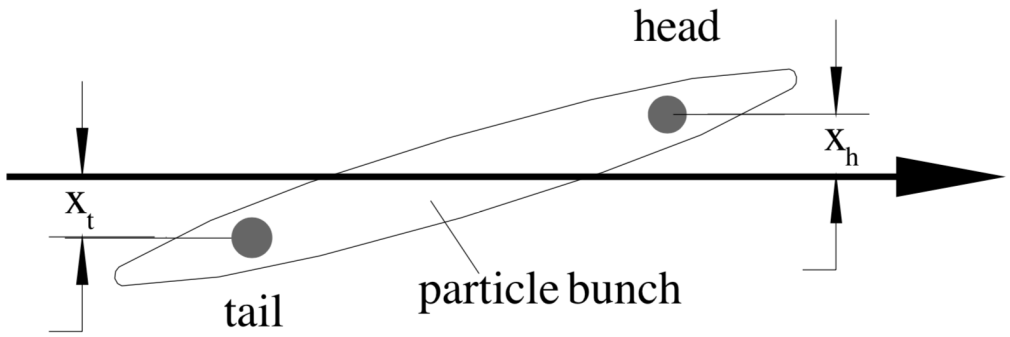

Figure 3.3: *Scheme of the two-particle model used for the fast head-tail instability.*

where the minus sign denotes a loss of energy. The coupling impedance of an accelerator component may be narrow band with a high quality factor $Q \gg 1$, like in accelerating cavities, or broad band with $Q \approx 1$, usually when there is a sudden change in the beam pipe cross section, as happens where collimators jaws are placed. Wake fields generated by broad band impedance components last for a very short time, they decay before the next bunch arrives and are therefore responsible for longitudinal and transverse single bunch instabilities.

3.2.1 The fast head-tail instability

At high frequencies, there is an effect of transverse wake fields generated by the head of a particle bunch on particles in the tail of the same bunch. Such interaction occurs for broad band impedances where the bunch generates a short wake including a broad spectrum of frequencies. Initially all these fields add up and act back coherently on particles in the tail of the bunch, but they quickly decoher and vanish before the next bunch arrives, so this is a single-bunch effect.

This kind of instability can happen in linear as well as in circular accelerators. The dynamics in a linac is different from that in a circular accelerator: in the former case the length of the accelerator is too short to have appreciable synchrotron oscillations, while in the latter case particles in the head of a bunch will oscillate between head and tail in the course of synchrotron oscillations, disturbing the coherence between head and tail, and the instability becomes much weaker. On the other hand, particles in circular accelerators are expected to circulate for a long time and even a reduced effect may still be strong enough.

The instability can be described using a two-particles model [34] [41], in which the bunch is divided in two macro-particles carrying each one half of the bunch current. A scheme of the model can be observed in fig. 3.3. The head particle will generate a transverse wake field acting on the tail particle and proportional to the transverse displacement x_h. While the head particle performs free betatron oscil-

lations around the reference orbit, the tail particle behaves like a driven oscillator, with free oscillations and forced ones that grow with s. The oscillation amplitude of the tail particle can increase up to the dynamic aperture, then it's lost.

The fast-head tail instability, also called Transverse Mode Coupling Instability (TMCI), clearly depends on the strength of the wake fields, from which the kick factor is obtained. Given that collimators have movable jaws, the strength of the wake fields, and so the effect of the instability, depends on collimators aperture. Studies on the TMCI as a function of the collimators aperture may be conducted to find aperture limits, as will be shown in section 3.4.2.

3.3 Material analysis for collimation systems

A collimation system should be able to sustain the heat load of the travelling beam without being damaged, and should survive the direct impact of the beam. An estimation of the maximum temperature rise sustainable by the collimator can be given considering the characteristics of the jaws material and the mechanisms that cause the temperature rise.

The temperature rise of collimators jaws depends on the material, and in particular on three different characteristic temperatures of each material [35]:

- **Melting temperature**: is the temperature at which the material changes state, from solid to liquid, at atmospheric pressure. The maximum allowed temperature rise that the material can undergo is given by: $\Delta T_l = 0.7 \cdot T_l - T_r$, where T_l is the melting temperature, T_r the room temperature (293.15° K) and 0.7 is an empirical factor.

- **Mechanical fracture temperature**: is the temperature at which the material breaks. The temperature rise that causes the mechanical failure is given by: $\Delta T_f = \epsilon \sigma_{uts} / \alpha_T Y$, where ϵ is an empirical factor, σ_{uts} is the maximum tension supported by the material, α_T is the thermal expansion coefficient and Y is the Young's modulus.

- **Vapor pressure temperature**: is the temperature at which the surface of the material evaporates. This is usually a higher temperature than the other two already described.

To choose the material for collimators jaws, Δ_l and Δ_f are used, together with the material conductivity and the radiation length. The choice of the material is a compromise between these parameters, for instance copper has the highest conductivity, so it would be the best choice to minimize wake fields, but it has low Δ_l and Δ_f, so it's not optimal since it can easily suffer damage due to temperature

Material	Melting temperature T_l [$10^{-6}/^\circ$ K]	Radiation length X_0 [g/cm^2]	Expansion coefficient α_T	Electric Conductivity σ [S/m]
C	4098	42.7	1.1	1.0×10^5
Ti	1941	16.2	8.7	2.4×10^7
Cu	1358	12.9	16.6	5.9×10^7
W	3695	6.8	8.5	2.0×10^7

Table 3.1: *Parameters for some materials taken into consideration for collimators head.*

rise. Some parameters of materials considered to build collimators jaws are shown in table 3.1.

There are basically three different rise temperature mechanisms on collimators jaws:

- **Electric field breakdown**: this mechanism is based on the interaction of the electric field carried by the beam with collimators jaws. The electric field, if high enough, can produce an electric discharge that can cause heat damage on the surface of the jaws, increasing the wake fields induced by the beam due to the deformation of the collimators jaw.

- **Image current heating**: the basic principle is that EM fields carried by the beam produce image currents on the jaws surface, which cause temperature increase. But there are different cases depending on the collimator aperture d [35] [36]:

  - $d \gg \sigma$: in this case the beam is far from the jaws, so it can be approximated as a point-like beam. The energy density deposited by the beam of charge Q and bunch length σ_z is given by [35]:

$$E_{D,bunch} = \frac{Z_0 c Q^2}{2\pi\sigma_z^2 4\pi r^2} \tag{3.29}$$

    where r is the beam pipe radius.

  - $d \geq \sigma$: the approximation used in the point above is not valid anymore, the beam cannot be considered as point-like, and the deposited energy is estimated to be a factor 4 higher than the one written in equation (3.29).

  - $d < \sigma$: in this case part of the beam hits the collimator jaws, which causes heating by beam-matter interaction, that is described in the next bullet. For what concerns heating due to image current, the energy den-

sity deposition is given by [35]:

$$E_{D,bunch} = \frac{Z_0 c Q^2 f_{max}^2(\sigma_y/\sigma_x)}{2\pi\sigma_z^2 4\pi\sigma_x/\sigma_y} \tag{3.30}$$

where $f_{max}(v) = \sqrt{1/2\pi v}\ ln(1+\pi v)$.

The previous estimations of image current heating are valid only for one bunch. To have the effect of the full beam, the diffusion distance, which takes into account how much of the energy deposited is dissipated when the next bunch arrives, must be considered. The diffusion distance is defined as $x_{heat} = \sqrt{K t_{beam}/c_p}$, where K is the thermal diffusion coefficient, c_p is the specific heat capacity and t_{train} is the duration of the bunch train. In this way the energy density deposition for a beam with multiple bunches becomes:

$$E_{D,beam} = E_{D,single} N_p \frac{\delta_e}{x_{heat}\sqrt{\pi}} \tag{3.31}$$

where N_p is the number of bunches and δ_e the effective skin depth that characterizes the layer of material where the energy is deposited.

- **Direct beam-matter interaction**: if the beam penetrates into the jaws, beam particles interact with jaws material, releasing energy inside them. The interaction depends on the type of particles the beam is made of. Considering electron beams, the kind of interaction depends on the energy of the particles: at low energies, less than 10 MeV, electrons lose energy primarily by ionization, whit less contributions given by bremsstrahlung or Moller scattering; above 10 MeV bremsstrahlung dominates, so photons are produced inside the material and an electromagnetic shower is generated. The energy released crossing a thickness z of the material is given by:

$$E(z) = E_0 e^{-\frac{z}{X_0}} \tag{3.32}$$

where X_0 is the radiation length of the material, defined as the distance traveled by a particle after reducing its energy by a factor $1/e$.

It's important to underline that in case the beam goes through collimators jaws, a big amount of energy is released due to the mechanisms described above, and this could cause serious damage to collimators jaws, especially if the material has a high Z and so the energy release is confined in a very short length.

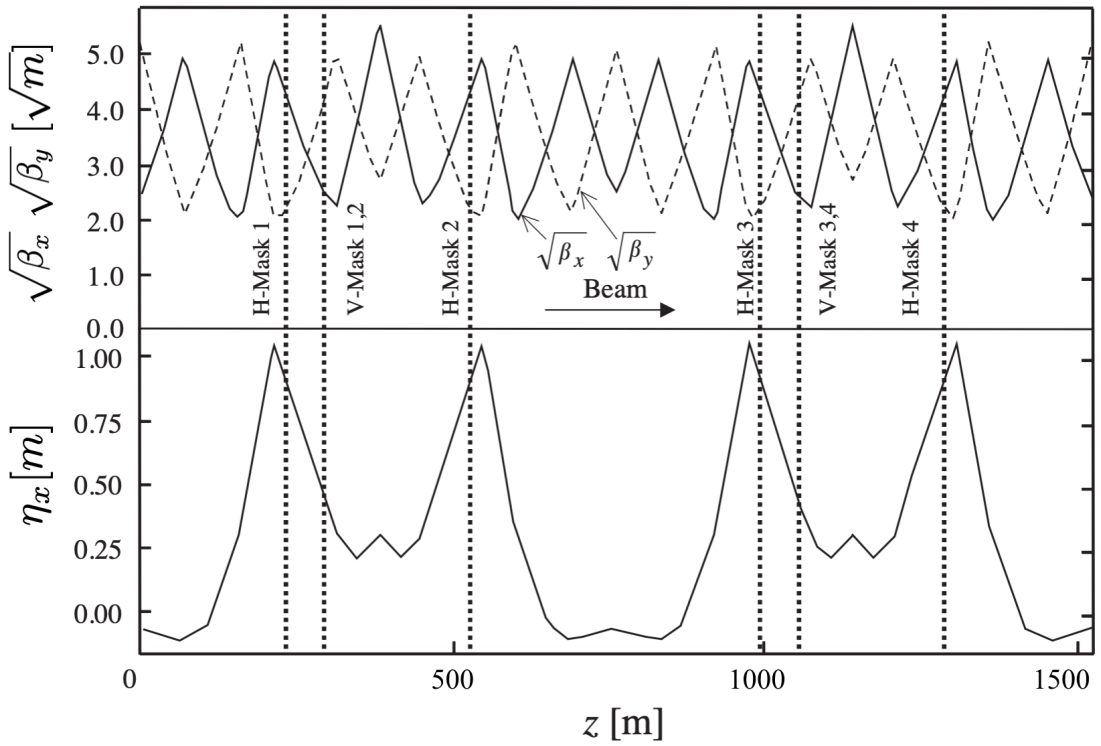

Figure 3.4: *Location of some KEKB collimators in the lattice diagram. Horizontal and vertical beta functions are shown on the top, dispersion is shown on the bottom.*

3.4 Collimation system in SuperKEKB

To reduce beam halo particles, the SuperKEKB accelerator is equipped with collimators. Beam halo particles may hit the beam pipe and, given that their energy is much higher than 10 MeV (as discussed in section 3.3), they produce showers that can hit the Belle II detector, affecting its lifetime and performance. All events recorded by the detector that are not coming from interesting collision events are referred to as "machine induced background". The different mechanisms to generate backgrounds are described in detail in chapter 4. Two different types of collimators are used in SuperKEKB, old collimators designed for KEKB [37] and new ones adopted in the Tsukuba straight section and in the LER [38]. In the following sections, both designs are described.

3.4.1 KEKB type collimators

In KEKB, 16 collimators were installed in each ring, in the arc sections on the upstream side of the Belle detector. Fig. 3.4 shows how the collimators for one ring are placed as a function of the betatron functions and horizontal dispersion: in the vertical direction, as described in section 3.1.1, dispersion can be neglected and collimators can be considered as pure betatron collimation systems, so they

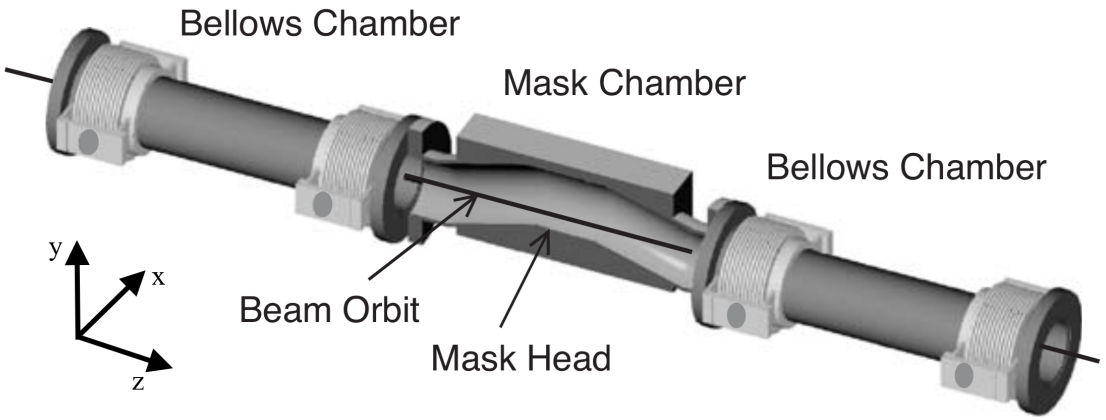

Figure 3.5: *Conceptual drawing of a vertical KEKB-type collimator.*

are placed where the vertical betatron function (dashed line in the figure) has a maximum; in the horizontal direction dispersion cannot be neglected, so collimators are treated as energy collimation systems and the considerations done in section 3.1.2 for equation (**??**) are applied, so collimators are placed where both horizontal betatron function and dispersion have a maximum. Half of the collimators were vertical and had one movable jaw on the top or on the bottom, while the horizontal ones had one movable jaw only on the inside part of the ring, to avoid synchrotron radiation on the horizontal plane. Collimator heads were very close to circulating beams, so intense HOMs could be generated there, heating vacuum components and exciting beam instabilities. Collimators design and RF technologies employed in KEKB were supposed to deal with high HOMs and high currents.

The conceptual drawing of a vertical KEKB-type collimator is shown in fig. 3.5. The collimator has a mask chamber with a constant cross section that matches the shape of the KEKB beam pipe, 50 mm high and 104 mm wide. The mask chamber is coupled to the beam pipe on both sides with bellows chambers made of stainless steel, that can absorb the movement of the mask. These bellows have the same RF shield structure as other bellows used in KEKB, with lots of fingers of 5.5 mm width, a length of 20 mm and a thickness of 0.2 mm, with a gap of 0.5 mm between each finger. A full set of one mask chamber and two bellows chambers have a length of 2.0 m. The mask chamber is made of aluminum alloy, while the head of the collimator was made by titanium. The choice of the material came considering in particular the melting temperature T_l and the radiation length: copper (Cu), titanium (Ti) and carbon (C) were considered. After many tests, it was decided to use 40 mm long titanium heads for collimators. C has a very long radiation length, about one order of magnitude higher that the other two materials, and this would have required too long heads, while Cu has a melting temperature of 1080° C against the 1800° C of Ti. The problem of titanium is the high electrical resistivity compared to copper, that

might excite beam instability when the beam is close to the head. For this reason, collimators heads were coated by 10 μm of copper. To reduce the gas desorption rate of inner surfaces of the mask chamber, all components were cleaned with acid to remove the oxide layer formed during machining, and then they were assembled in a clean room. Mask chambers and bellows chambers were also pre-baked at 150° C for 24 hours before being installed.

The position of each collimator head was controlled by the distributed control system called EPICS. The head moves at a speed of 0.5 mm/s and is positioned with an accuracy of 0.1 mm. The full stroke is 20 mm, $\pm$10 mm around the nominal position. The position of the head is monitored by a linear potentiometer with a linearity error less than 0.2%. There are four mechanical limit switches and two stoppers to constraint the movement. Each bellows chamber has a thermometer to monitor the temperature during beam operation, and a flow sensor to monitor the water cooling system. If any sensor detects an anomaly, an alarm is raised and a beam abort is triggered.

The most important feature of this design is that there are no trapped HOMs around the mask head. HOMs are excited only if the beam circulates well off the reference orbit, but even in this case, they are not trapped inside the mask chamber, they can travel along the beam pipe. And there are also no trapped HOMs between adjacent collimators. One problem that cannot be avoided is heating the bellows near the collimator head due to the TE HOM, this mode can heat up other vacuum components, like vacuum pumps for instance. Heating was one of the main problems that was considered in the design of the SuperKEKB type collimator.

3.4.2 SuperKEKB type collimators

With the upgrade of KEKB to SuperKEKB, some collimators of the old machine were reused, but in some cases a new collimator design was necessary, especially where the old beam pipe was replaced by the new one with antechambers, meaning most of the LER and the Tsukuba straight section, as mentioned in section 2.2.2. The positioning of collimators in SuperKEKB as a function of the betatron function and dispersion is shown in fig. 3.6 for the D12 sector of the HER (old KEKB-type collimators) and in fig. 3.7 for the D06 sector of the LER (new SuperKEKB-type). As for KEKB, horizontal collimators are positioned where the horizontal betatron function and the horizontal dispersion are close to a maximum, while vertical collimators are placed where the vertical betatron function is close to a maximum. New collimators were designed to fit the antechamber scheme and to minimise even more excitation of HOMs and heating of vacuum components. Both horizontal and vertical collimators were re-designed, as shown in fig. 3.8. SuperKEKB collimator

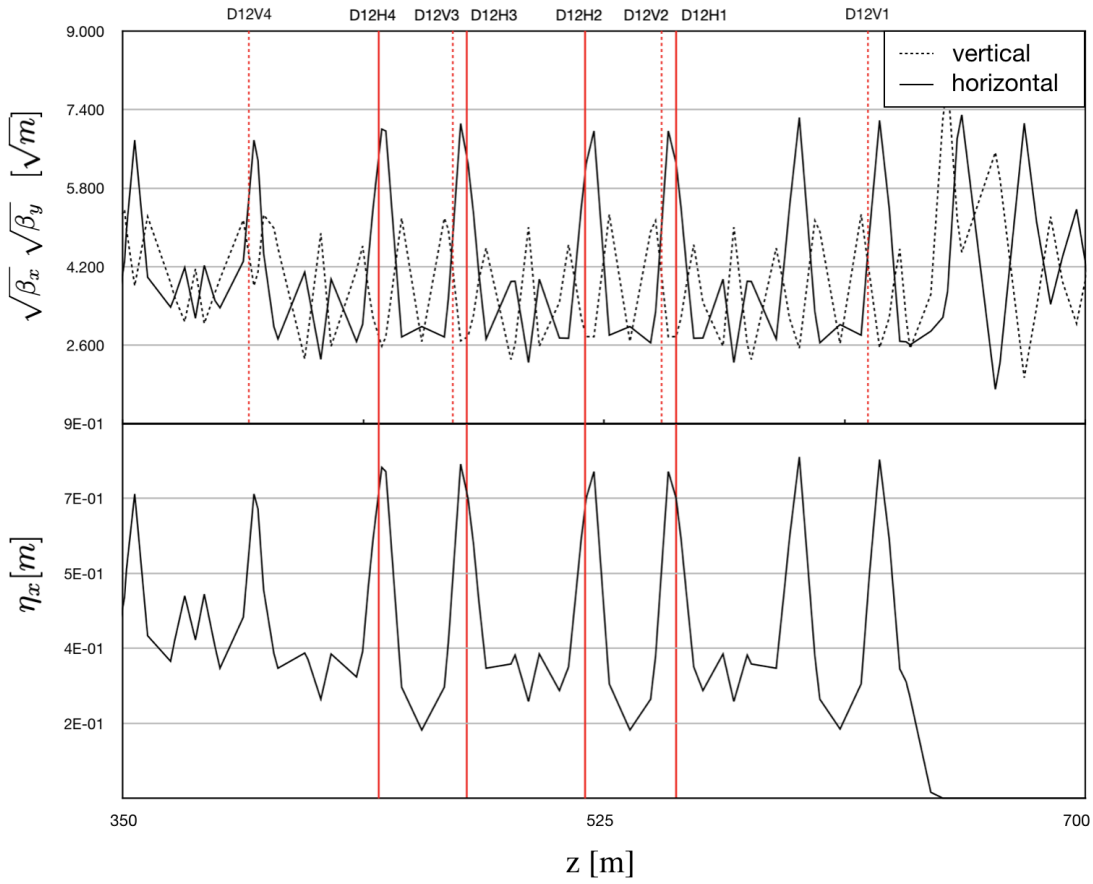

Figure 3.6: *Location of some HER collimators in SuperKEKB, sector D12. These collimators are of the KEKB-type*

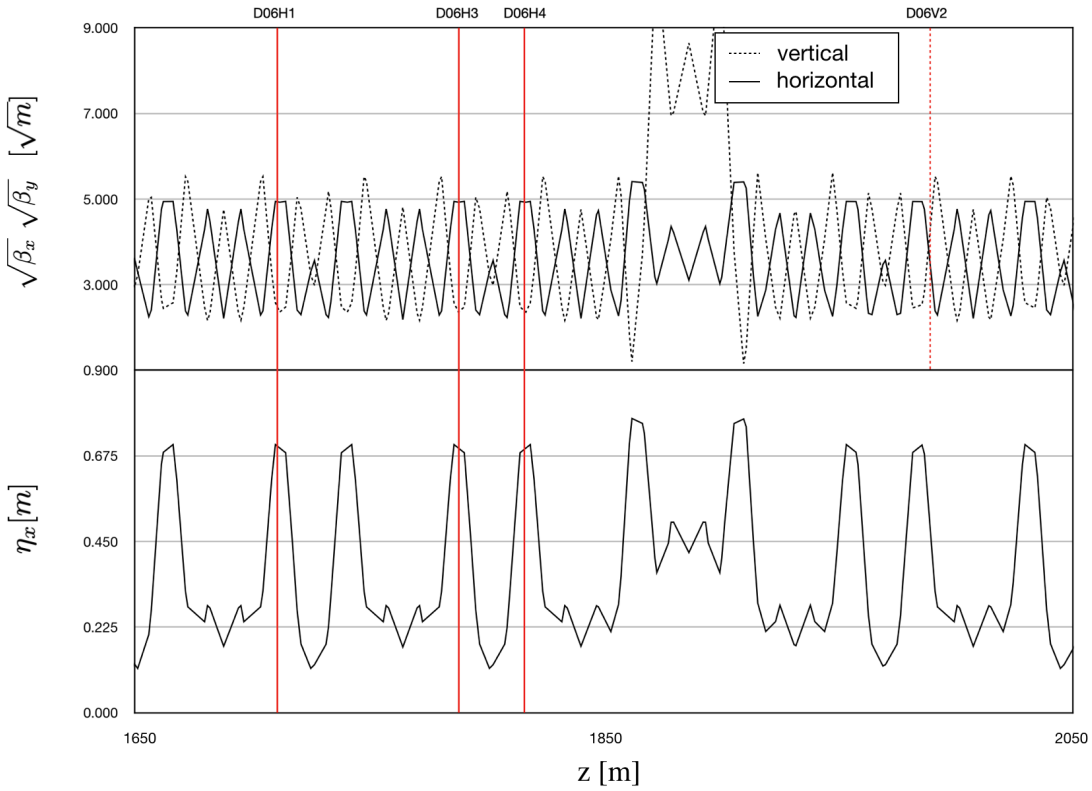

Figure 3.7: *Location of some LER collimators in SuperKEKB, sector D06. These collimators are of the SuperKEKB-type.*

chambers are tapered from the end to the center to avoid HOMs excitation, and in the vertical collimators also the antechamber is tapered to the center of the collimator head. Collimators have two independently movable jaws, so horizontal ones can scrape the beam from the inside and the outside, while vertical ones can scrape the beam from top and bottom at the same time. A part of each horizontal movable jaw is placed inside the antechamber, while in the vertical collimators the parts where movable jaws are inserted are not tapered; in both cases the total impedance is lower than in KEKB collimators. The chambers and the jaws are made of oxygen-free copper. Matsumoto-Ohtsuka flanges and racetrack shaped flanges that couple collimators with the rest of the vacuum components are made of chromium copper and stainless steel respectively. Each jaw has a cooling channel inside it to improve heat dispersion. The head material has been changed from titanium to tungsten, because of the higher melting temperature and shorter radiation length of titanium, as shown in table 3.1. Finger type RF shield are also attached to the jaws, because there is a cavity behind it where HOMs can be trapped.

A study on KEKB-type and SuperKEKB-type collimators impedance has been done using GdfidL electromagnetic field simulator [39]. As described in section 3.2, a longitudinal loss factor and a transverse kick factor are used to characterize the effect of collimators impedance on the beam. Equations (3.26) and (3.27) can be

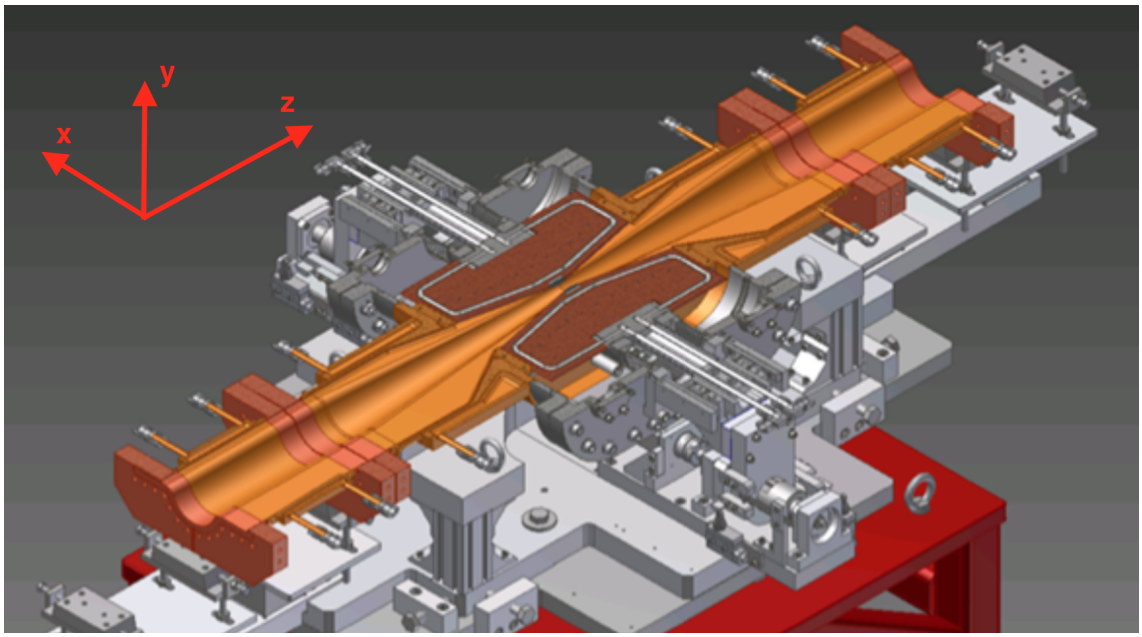

(a) *horizontal*

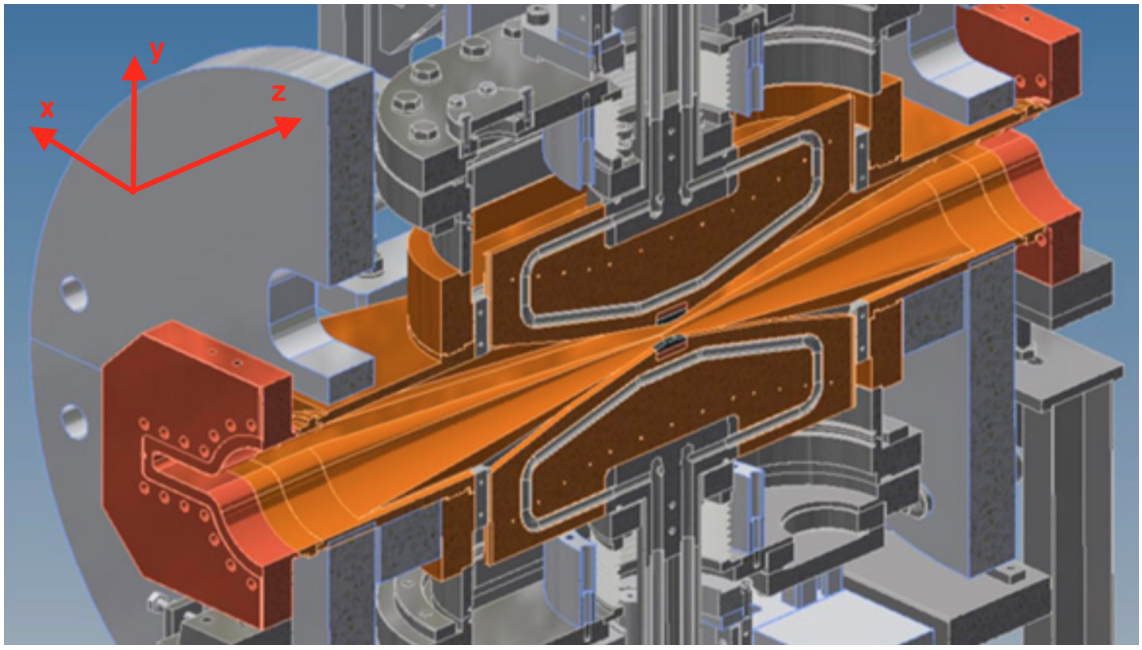

(b) *vertical*

Figure 3.8: *SuperKEKB type collimators, horizontal and vertical.*

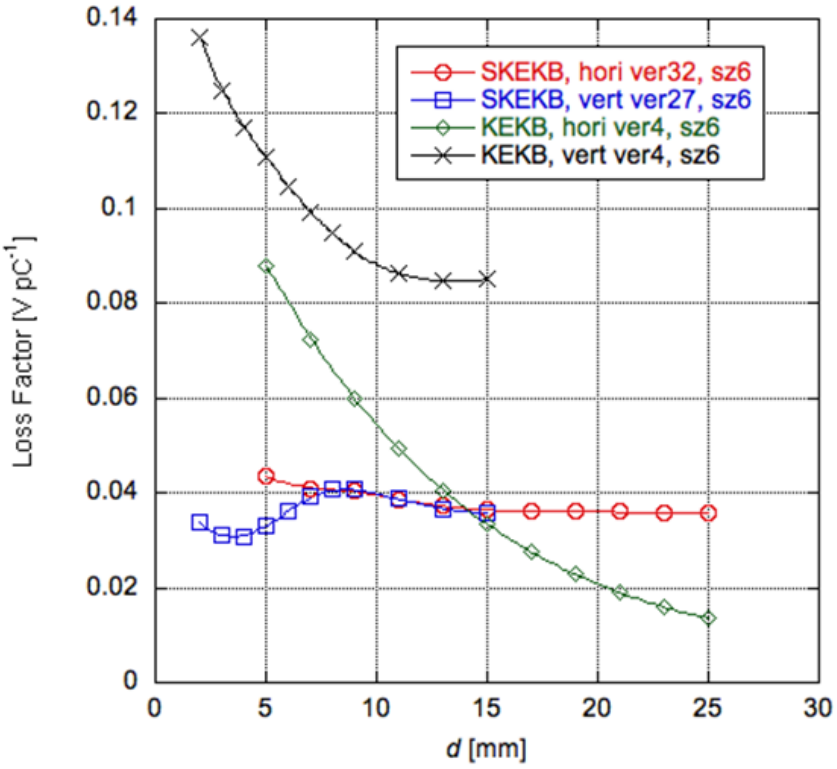

(a) *loss factor*

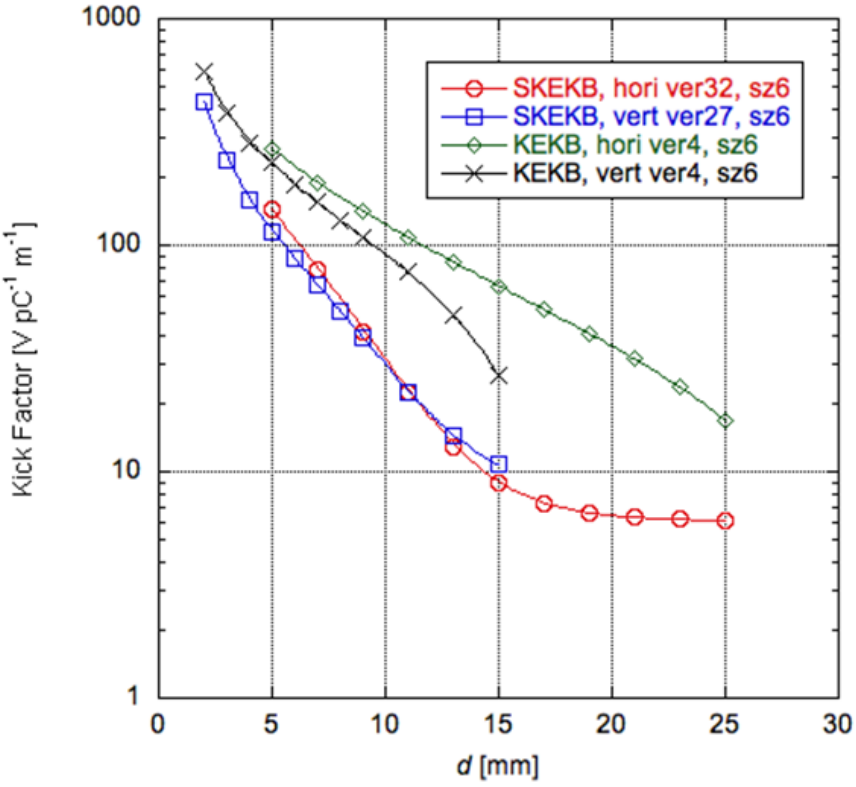

(b) *kick factor*

Figure 3.9: *Loss factor and kick factor of KEKB-type and SuperKEKB-type collimators evaluated with GdfidL.*

used to evaluate the loss factor and the kick factor as a function of collimators aperture. Fig. 3.9 shows loss factors (a) and kick factors (b) for both types of horizontal and vertical collimators, estimated using a bunch length of 6 mm. Kick factors are evaluated with a beam offset from the reference orbit of 1.0 mm in horizontal direction and 0.5 mm in vertical direction. Loss factors and kick factors of SuperKEKB-type collimators are less than the KEKB ones, with the exception of the loss factor of the horizontal KEKB collimator, which is slightly lower than the SuperKEKB one with an aperture of 15 mm, which is anyway very wide compared to the expected apertures at nominal SuperKEKB parameters. The kick factor was used to evaluate the bunch current at which the Transverse Mode Coupling Instability (TMCI) can occur for each beam [40]:

$$I_{thr} = \frac{C_1 f_s E/e}{\sigma_z \sum_i \beta_i \kappa_{\perp i}} \tag{3.33}$$

where C_1 is ≈8, f_s is the synchrotron frequency, E/e is the beam potential, σ_z is the bunch length, β_i is the beta function at each collimator, and κ_i is the kick factor of each collimator. At the nominal SuperKEKB parameters, an optimised collimator configuration was used to evaluate the bunch current threshold [38]: to avoid TMCI instability, for LER bunch current thresholds were 1.67 mA/bunch and 10.43 mA/bunch for horizontal and vertical directions respectively, while for HER the thresholds were 1.94 mA/bunch and 2.34 mA/bunch for horizontal and vertical directions respectively. The design bunch current are 1.44 mA/bunch for LER and 1.04 mA/bunch for HER. From this number, a minimum aperture was indicatively set for collimators to avoid TMCI. Suggested minimum apertures were 8 mm for horizontal collimators and 2 mm for vertical ones in LER, 7 mm and 2 mm for horizontal and vertical collimators respectively for HER. These values were taken into consideration for the collimator studies that will be described in section 5.4.

Chapter 4

Background sources in SuperKEKB

Modern e^+e^- colliders are subject to many sources of background, that can be divided in single beam backgrounds and luminosity backgrounds. The challenging machine parameters that should be used to achieve SuperKEKB design luminosity will make background conditions particularly harsh. In this chapter, an overview of the most important background sources of both kind for SuperKEKB is given.

4.1 Single beam background sources

4.1.1 Touschek effect

Touschek effect is a kind of Coulomb scattering between particles in the same bunch, where two particles exchange energy and transform a small transverse momentum into a large longitudinal momentum. The amplification of the momentum in the longitudinal direction is a relativistic effect due to the Lorentz factor γ. Both scattered particles are immediately lost, one with too much energy, the other with too less. The difference with intra-beam scattering is that the Touschek effect is a single scattering which leads to the immediate loss of the two particles involved, while the intra-beam scattering is a multiple scattering phenomenon that happens in all directions and causes an increase in beam size.

A general formula for the particles loss rate due to the Touschek effect has been derived by Piwinski [42]. For SuperKEKB the same formula can be simplified in the approximation of flat beams and can be written as follows:

$$R = \frac{N}{\tau} = \frac{1}{L_{ring}} \oint r \, ds \tag{4.1}$$

where N is the number of particles in a bunch, τ is the lifetime, L_{ring} is the ring

circumference, and r is the local loss rate, defined as:

$$r(u_a, \varepsilon_x, \beta_x, \eta_x, \varepsilon_y, \beta_y) = \frac{r_e^2 c \beta_x N^2}{8\pi\gamma^3 \beta \sigma_{x\beta}\sigma_{y\beta}\sigma_z \sigma_x u_a} C(u_a) \tag{4.2}$$

with:

$$C(u_a) = -\frac{3}{2}e^{-u_a} + \int_{u_a}^{\infty} \left(1 + \frac{3}{2}u_a + \frac{u_a}{2} ln \frac{u}{u_a}\right) e^{-u} \frac{du}{u} \tag{4.3}$$

$$u_a = \left(\frac{\delta_a \beta_x}{\gamma \sigma_{x\beta}}\right)^2 \tag{4.4}$$

$$\sigma_x = \sqrt{\varepsilon_x \beta_x + (\eta_x \sigma_\delta)^2} \tag{4.5}$$

$$\sigma_{x\beta} = \sqrt{\varepsilon_x \beta_x} \qquad \sigma_{y\beta} = \sqrt{\varepsilon_y \beta_y} \tag{4.6}$$

In the above equations, γ is the normalised energy, δ_a is the momentum acceptance of the ring, σ_δ is the energy spread, η_x is the horizontal dispersion.

Without going into the details of the integration, it's possible to express the rate as a function of some of the relevant quantities that characterize a beam. The Touschek loss rate results proportional to the number of bunches in the ring and to the second power of the bunch current, while is inversely proportional to the beam size and the third power of beam energy:

$$R \propto \frac{I_b^2}{n_b \sigma_x \sigma_y \sigma_z E^3} \tag{4.7}$$

Based on these dependences, a simple scaling based on beam size and beam energies predicts a higher Touschek background in SuperKEKB with respect to KEKB by a factor $\sim$20.

4.1.2 Beam-gas interactions

Another beam background source is due to interaction between beam particles and residual gas molecule in the beam pipe. In total, there are four different processes of beam-gas interaction:

1. **Elastic scattering on nuclei**. Beam particles are scattered by gas atoms nuclei, receiving an angular kick that affects the transverse motion. If the amplitude of the kick makes the particle exceeds the vacuum chamber aperture, the particle gets lost, with the loss that mostly occurs in the vertical plane.

2. **Bremsstrahlung on nuclei**. It's an inelastic scattering process that leads to energy loss by the beam particle. The particle is lost if its energy deviation is larger than the RF acceptance of the ring. This process is independent of particle energy.

3. **Elastic scattering on electrons**. The high energy beam particle can transfer part of its energy to the electrons of the residual gas. The beam particle is lost if its energy deviation exceeds the RF acceptance. This process is inversely proportional to the beam energy.

4. **Inelastic scattering on electrons**. In this process photons are emitted, but in this case the process has a dependance on the particle energy, as $ln(\gamma)$.

The most important processes are 1 and 2, with the elastic scattering on nuclei being more dominant at low energies and the bremsstrahlung increasing at higher energies. However, the elastic scattering strongly depends on the aperture of the vacuum system, and for small aperture, as it is especially in the interaction region of SuperKEKB, it becomes comparable to bremsstrahlung even at high energies.

Beam-gas interactions depend on the pressure of the residual gas in the beam chamber, which as a matter of fact depends not only on the vacuum system, but also on the beam current. The residual gas pressure can be written as:

$$P = P_0 + \lambda I \tag{4.8}$$

where P_0 is the static pressure that is achieved with no beams, I is the beam current, and λ is the outgassing coefficient related to the gas desorption process, that can be summarised in two points:

- synchrotron radiation hits the inner surface of beam pipe walls and causes the emission of photoelectrons;

- photoelectrons are emitted over a large solid angle and can hit beam pipe walls causing a molecule to come out of the material.

This process will clearly increase with beam current, increasing the residual gas pressure in the beam pipe. The pressure, thus, is not static, but it changes once beams start circulating in the machine. Static pressure as low as 10^{-11} Torr can be achieved with a good vacuum system, but once beams will circulate in the machine, dynamic pressure will be higher by 2 or 3 orders of magnitude. To reduce λ the vacuum chamber needs proper cleaning, baking and enough vacuum scrubbing, in order to reach high currents keeping the beam-gas background to acceptable levels.

The residual gas pressure can also affect beam size, because of small energy deviations and transverse deflections from beam-gas interactions. This effect does not affect lifetime, but it's still a noise contribution that affects the damping of particle motion and causes emittance blow up, in particular for the vertical transverse emittance.

4.1.3 Synchrotron radiation

Synchrotron radiation is the emission of photons when a charged particle is accelerated. When a particle is at rest, the electric field lines extends radially from the particle, and there is no magnetic field component. When a particle is in uniform motion, a reference frame can be defined in which the particle is at rest (rest frame of the particle) and the field lines are still extending radially from the particle, with no magnetic field component. When a particle is accelerated in the longitudinal direction, assuming that the acceleration happens from a point A to a point B, starting at a time $t = 0$ and lasting for a time ΔT, the particle moves in its rest frames and electric field lines become distorted, still connecting to the unperturbed field lines that are at a distance $c\Delta T$ or larger. In this case, because the particle moves in its rest frame, an azimuthal magnetic field component is created, and there is emission of radiation from the accelerated particle. The radiation is emitted normal to the direction of acceleration. But acceleration can happen also in the direction transverse to the direction of motion of the charged particle. In this case the distortion of the field lines creates transverse field components with the maximum distortion in the direction of motion of the particle. The radiation is emitted mainly in the forward direction, tangential to the particle motion, with an angle proportional to $1/\gamma$. The transverse acceleration describes perfectly what happens when a particle goes through magnets in the accelerator.

The instantaneous synchrotron radiation power can be written as:

$$P(\mathrm{GeV/s}) = c\frac{C_\gamma}{2\pi}\frac{E^4}{\rho^2} \tag{4.9}$$

where $C_\gamma = 8.8575 \times 10^{-5}$ m·GeV^{-3} is called "Sand's radiation constant" for electrons [41], and ρ is the curvature radius of the bending magnet. The intensity of the radiation is therefore proportional to the fourth power of the beam energy and inversely proportional to the square of the curvature radius. The spectrum of synchrotron radiation from relativistic particles in a circular accelerator is composed of harmonics of the particle revolution frequency, and extends mainly up to the critical frequency:

$$\omega_c = C_c\frac{E^3}{\rho} \tag{4.10}$$

where $C_c = 3.37 \times 10^{18}$ m·s·GeV^3 is calculated for electrons [41]. Beyond the critical frequency, the intensity of synchrotron radiation drops significantly. In practice, the energy of synchrotron radiation photons in SuperKEKB is expected to be between a few keV to tens of keV.

Synchrotron radiation was considered with extreme attention in the design of SuperKEKB, because it was the primary cause of the damage that occurred to the

inner layer of the Belle SVD, severely damaged by ∼2 keV photons from the HER. To mitigate synchrotron radiation background in the Belle II detector, particular care was taken in the design of the beam pipe in the interaction region of SuperKEKB: ridge structures on the inner surface of incoming pipes prevent scattered photons from reaching the interaction point, and to absorb photons that would otherwise reach the inner layers of the Belle II VXD, the inner surface of the Phase 2 beryllium beam pipe has been coated with a 6μm gold layer, while the final beam pipe for Phase 3 has been coated with a 10μm gold layer.

4.1.4 Injection background

As described in section 2.3, so far in SuperKEKB the betatron phase-space injection technique was used. With this method, the injected beam performs betatron oscillations around the stored beam, until the perturbation is fully damped, which can take up to a few tens of milliseconds. When injected particles are passing through the interaction region, they are influenced by the strong fields of the final focus quadrupole magnets, therefore if they are on the edges of the transverse phase space, they can be easily lost inside the interaction region, becoming a source of background that can potentially affect the performance of the inner components of the Belle II detector. This mechanism will occur every time injection is performed, so with the use of continuous injection, especially when the machine will run at the design values and the beam lifetimes will be small, the detector would almost constantly be affected by injection background.

During Phase 2 and the first run of Phase 3, running conditions changed many times, and this often caused problems having clean beam injections, resulting in high background levels in the interaction region. During Phase 2 the CLAWS detector and diamond sensors were used to monitor the amplitude and the duration of injection background and to provide to the machine group important information on the injection conditions. During Phase 3, although the CLAWS detector was not available anymore in the VerteX Detector volume, many studies were devoted to improve injection efficiency and to lower injection background, before start using continuous injection with both beams.

4.2 Luminosity background sources

In this section, the two relevant background sources that scale with luminosity are described. Since luminosity has been two orders of magnitude below the design value, these sources were not dominant in the first commissioning phases of KEKB, but they will be more and more relevant as soon as the luminosity will increase.

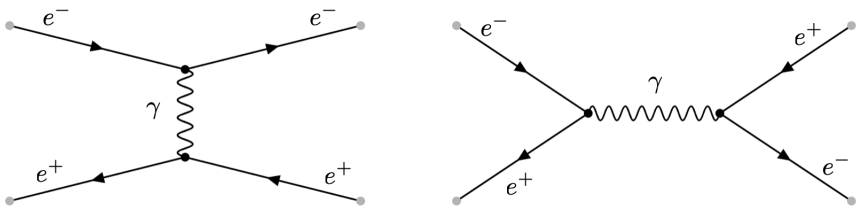

Figure 4.1: *Feynman diagram of the Bhabha scattering processes, t channel on the left, s channel on the right.*

4.2.1 Radiative Bhabha scattering

The Bhabha scattering [43] is the scattering of an electron-positron pair in which also the final state is an electron-positron pair, and the interaction happens with the exchange of a photon, as shown in fig. 4.1. In the radiative process, particles loose energy through the emission of a photon, as shown in fig. 4.2, that propagates nearly along the direction of motion of the particles. There are two main mechanisms that contribute as background sources for the detector in the radiative Bhabha scattering:

1. In a beam of particles, photons are emitted along the beam axis and interact later with the iron of the accelerator magnets. In this second interaction of photons with the iron, there is a huge production of low energy gamma rays and neutrons thanks to the giant photo-nuclear resonance mechanism. Low energy gamma rays are a big background source for the CDC and the TOP counter, while the neutrons are the main background source for the KLM sub-detector.

2. Primary particles, after energy loss due to the photon emission, will be off-energy and, once passing through the first QCS magnet, that is focussing in the vertical direction but defocussing in the horizontal direction, can be lost in the QCS magnet and produce electromagnetic showers. This second mechanism is dominant in SuperKEKB with respect to the previous one.

Shielding material to stop these neutrons is added in the accelerator tunnel and wherever is possible near the Belle II detector. In addition, primary particles can be scattered at large enough angles and enter in the active volume of the detector, generating hits in some sub-detectors.

With the 40 times higher luminosity of SuperKEKB with respect to KEKB, radiative Bhabha scattering should be higher in SuperKEKB by around the same factor, but actually there is a difference in the final focus system design that helps mitigating this background source: as described in section 2.2.1, KEKB had same final focus quadrupoles for both incoming and outgoing beams, so particles that lost energy through the Bhabha scattering were over-bent by QCS magnets, producing

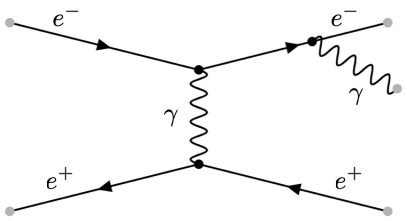

Figure 4.2: *Feynman diagram of radiative Bhabha scattering process.*

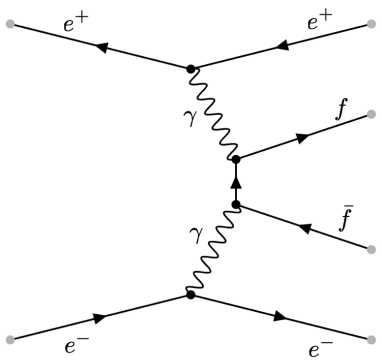

Figure 4.3: *Feynman diagram of the two-photons process.*

electromagnetic showers hitting the walls of the magnets. Radiative Bhabha losses within ± 65 cm of the IP are particularly dangerous because it's not possible to put enough shielding material in that region to prevent showers from entering the detector acceptance region.

In SuperKEKB final focus quadrupoles are not shared by incoming and outgoing beams, which are pretty on the magnets' axes, so only those particles that lose a considerable amount of energy are over-bent and therefore lost in the walls of the magnets, where they produce showers. This means that radiative Bhabha scattering is partially mitigated by the final focus design, although it still represents the most important source of background at nominal currents for some Belle II sub-detectors.

4.2.2 Two-photons process

The other important luminosity dependent background source is the two photon process, in which a low momentum pair of electron and positron is created with the mechanism shown in the Feynman diagram in fig. 4.3. The two low momentum particles can spiral in the solenoidal magnetic field and hit the inner detectors layers several times, while the primary particles, having lost a large amount of energy or being scattered at large angles, can be lost inside the detector, as for the radiative Bhabha process.

Chapter 5

The background simulation

5.1 The SAD simulation package

SAD (Strategic Accelerator Design) is an integrated code [46] [47] developed at the KEK laboratory, based on Fortran and C languages. It was used already for simulations of KEKB, and before it for other facilities in KEK. It can be used to model the machine lattice and simulate the motion of particles with six canonical variables: x, y, z, p_x, p_y, δ, where x, y and z are the coordinates in the transverse and longitudinal directions, p_x and p_y are the canonical momenta normalised by the design momentum p_0, δ is the relative total-momentum deviation from the design momentum p_0.

SAD can be used to model the lattice of an accelerator and to evaluate the characteristics of the lattice components needed for the machine. It can perform optics calculation and matching in 5D and 6D, and can do matching for geometry and off-momentum particles. It can be used for rings (closed orbits) or for linacs and transfer lines. The code can calculate the emittance of the machine like an electron ring enabling synchrotron radiation, intra-beam scattering and space charge. And it can also perform full 6D tracking of macro-particles, with the possibility of enabling or disabling functions like radio frequency in cavities, synchrotron radiation with or without quantum excitation, strong-weak beam-beam interaction, space charge, radiative Bhabha scattering and so on. The full 6D tracking of macro-particles has been used in the collimators studies that will be described in this chapter and whose results will be reported in the next chapters.

5.2 The SAD model of SuperKEKB

The starting point of the simulation model is the definition of a certain number of basic elements, like drift spaces, dipole magnets, quadrupoles, RF cavities and

all other elements of a lattice. The definition consist in indicating the length of each element and its properties, like the bending angle in a dipole magnet or the magnetic field gradient in a quadrupole. These basic elements can be used then to define larger objects, also called "cells", like for instance a sequence of a focusing quadrupole, a drift space, a defocusing quadrupole and another drift space (the so called "FODO"). All these definitions are performed in the SAD MAIN mode. Once a cell is defined, the SAD FFS mode comes into play: given the main machine parameters, all optics functions are calculated and matched imposing the necessary conditions. In the FODO example previously mentioned, periodic conditions of the orbit and optics must be imposed if a ring with a closed orbit has to be built. Once the parameters of the cell components are adjusted to match all conditions, more cells can be used one next to the other to create large sections of the machine. Together with all other cells that can be defined, a full ring with a closed orbit can be implemented. Once the ring is modelled, it is possible to make 6D full symplectic tracking of particles along the ring. In order to simulate processes that involve interaction between particles of the same bunch, a multi-particle tracking is necessary to follow the behaviour of charged particles along the orbit. On the other hand, computational resources impose a constraint on the number of particles that can be tracked in the simulation: performing a simulation with $\mathcal{O}(\sim 10^{10})$ particles in a bunch for $\mathcal{O}(\sim 10^{3})$ turns would require enormous computational resources and too much time. To overcome this constraint, the tracking simulation is done using a small number of "macro-particles", whose position and momenta are generated with a Gaussian distribution, and then scaling the results to the real number of particles in a bunch. In the SAD SuperKEKB background simulations, Touschek and beam-gas scattering are evaluated, with two processes considered for the beam-gas, Coulomb scattering and bremsstrahlung. In order to simulate the beam-gas scattering, a constant residual gas pressure along the ring of 1 nTorr is assumed. These physical processes are defined in a library file, and a description of how they are implemented is given in section 5.2.1.

To perform particle tracking along the ring, the SuperKEKB lattice is divided in slices of 1 m in the longitudinal direction. The interaction region, which extends for ± 4 m from the IP, is divided in thinner slices of 10 mm length. IR slices contain the information on the magnetic field of Belle II, the compensation solenoids, the QCS magnets and higher order multipole fields up to 44 poles for normal and skew fields. With all the information of machine optics, SAD tracks a particle from one slice to the next one, until the maximum number of turns set in the simulation is reached or until a particle reaches the physical limit of the beam pipe aperture, which means that the particle is lost. When this happens, its six canonical variables are stored into an output file, which is reprocessed to produce a ROOT format file that can

be analysed later and that is also used as an input for other simulations, like the background simulation performed with GEANT4 and briefly described in the next section.

There is one important point to be explained regarding how the loss point of the particle is evaluated: when a particle is lost in the IR, its tracking stops and its variables are saved in the output file, but due to the discrete slicing of the interaction, in general the particle is not lost exactly on the inner surface of the beam pipe, it's already inside it. This should be avoided because GEANT4 simulates the interaction of the particle with any medium the particle goes through, so if the particle is already inside the beam pipe wall, a fraction of the interaction with the beam pipe wall material is not accounted. For this reason a script is used to reprocess the SAD output files in order to shift the lost particles position exactly on the inner surface of the beam pipe, as shown in fig. 5.1. In particular, it should be noted that the particle is not traced back to the real loss position, it's just shifted perpendicularly toward the inner edge of the beam pipe wall. The loss position obtained with this procedure is not exactly the real one, but the fine 10 mm slicing and the consideration that the angle of incidence of particles is very small make this kind of approximation valid. However, a back-tracking of the particle to the real loss position would be the best choice, and it is one of the possible improvements of the simulation that will be taken into consideration in the future.

Using the SuperKEKB lattice defined in SAD, many different kind of simulations can be done enabling different options. The background simulation consist of a 6D tracking simulation, with RF cavities, synchrotron radiation and intra-beam scattering enabled. There are three different processes simulated (Touschek scattering, beam-gas Coulomb scattering and beam-gas bremsstrahlung), each one simulated in a separate job of the simulation. In a single job, the initial number of macro-particles to be tracked along the beam line is 250, for a maximum of 1000 turns. In order to increase statistics of the data, the simulation of each background process is done for 50 jobs, so 150 jobs are done for each ring, which makes a total of 300 jobs for a single full simulation.

In order to submit jobs to the computational grid, a bash script automatically select a ring (LER or HER), sets the background flag, submits 50 jobs per flag, and then repeat the same procedure for the other ring. To complete all the jobs, around 24 hours are necessary. A full sample output consists of $\sim$3.5 GB of data coming directly from SAD, plus $\sim$1.5 GB for the ROOT files produced from the SAD output files.

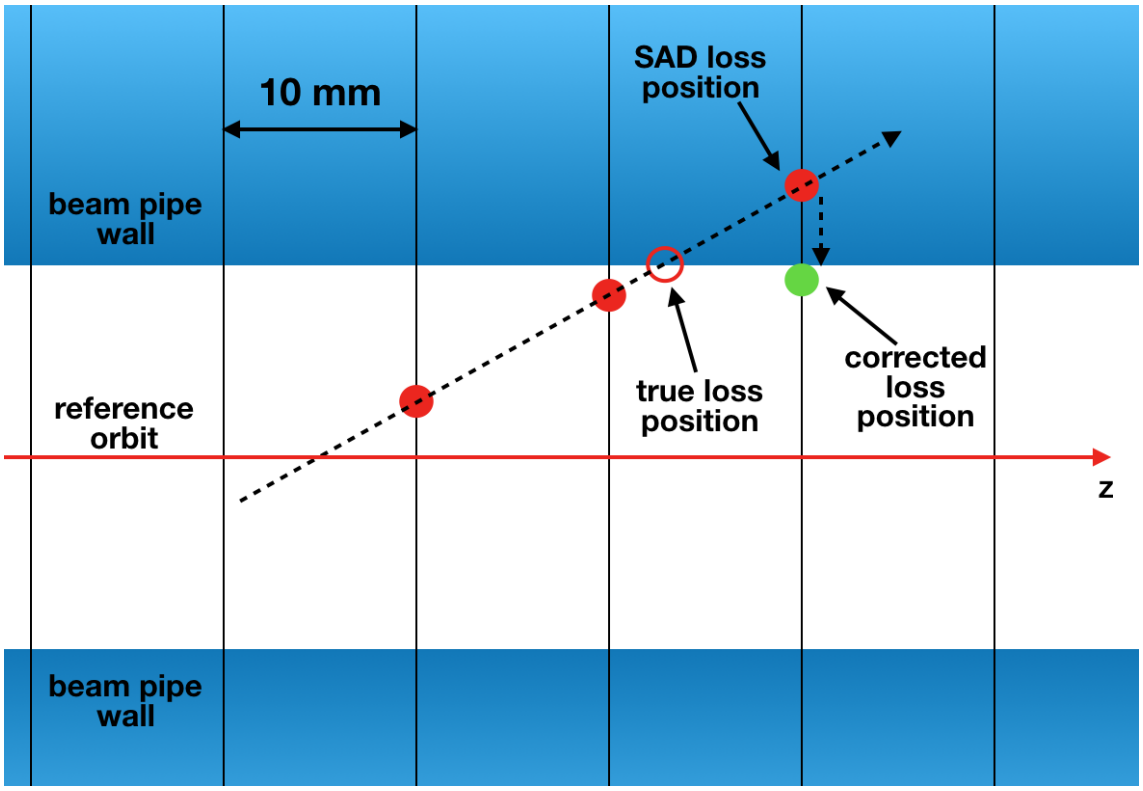

Figure 5.1: *Schematic drawing of how particles lost in the interaction region are given by SAD, and how the position is corrected to provide a correct input for the GEANT4 simulation.*

5.2.1 Touschek and beam-gas scatterings implementation

To simulate Touschek and beam-gas background sources, it is necessary to define how particles interact with other particles of the bunch or with residual gas molecules. For all three processes, cross sections are defined below.

- **Beam-gas Coulomb** - The probability of elastic scattering, including the screening effect of atomic electrons and for small angles, is given by [49]:

$$\left(\frac{d\sigma}{d\Omega}\right)_C = 4Z^2 R_e^2 \left(\frac{m_e c}{\beta p}\right)^2 \frac{1}{(\theta^2 + \theta_0^2)^2} \tag{5.1}$$

  with $\theta_0 \approx \alpha Z^{1/3}(m_e c/p)$, Z the atomic number of the residual gas atoms, $\alpha = 1/137$.

- **Beam-gas bremsstrahlung** - The probability of inelastic interaction on nuclei is given by [50]:

$$\left(\frac{d\sigma}{du}\right)_B = 4\alpha r_e^2 Z(Z+1)\frac{4}{3u}(1 - u + 0.75u^2)\ln\left(\frac{184.5}{Z^{1/3}}\right) \tag{5.2}$$

where $u = k/E$ is the fraction of energy lost by radiation, with k being the energy of the photon emitted in the bremsstrahlung event.

- **Touschek** - The probability of scattering of one particle with another particle in the bunch in the solid angle $d\Omega$ is given by the Møller scattering cross-section in the center-of-mass frame [51]:

$$\left(\frac{d\sigma}{d\Omega}\right)_T = \frac{r_e^2}{4\gamma^2}\left(\left(1+\frac{1}{\beta^2}\right)^2\left(\frac{4}{\sin^4\Phi}-\frac{3}{\sin^2\Phi}\right)+\frac{4}{\sin^2\Phi}+1\right) \tag{5.3}$$

For each macro-particle, at first the cross section is calculated, then an interaction rate is determined using the number of particles in a bunch and/or residual gas pressure, that are specified in the code. The interaction rate is then associated to the macro-particle as a parameter. If the macro-particle is lost somewhere in the ring, the associated rate is saved together with positions and momenta of the macro-particle. The rate is then multiplied by the number of bunches in the ring in order to calculate the loss rate, which is given in MHz.

The loss rate can be evaluated in a region of the ring, like the interaction region or the location of a collimator, or in the whole ring: specifying the interval in s where the rate has to be evaluated, all particles lost inside that interval will be considered, and the loss rate will be the sum of the rates associated to each macro-particle lost in the specified interval.

5.3 The GEANT4 model of BEAST II and Belle II

ROOT files generated from the SAD output are passed to the GEANT4 simulation [44] [45] inside the basf2 software [48], to simulate the effect of background in the detector volume. During the simulation, GEANT4 transports each primary particle step-by-step inside the detector, simulating the interaction with the material, creating secondary particles and producing simulated hits in all detector components. Simulated background hits are produced for all background sources described in the previous chapter, with the exception of synchrotron radiation, that is not included. To simulate the interaction of particles with the material of the interaction region and to generate hits on the sub-detector, the Belle II detector geometry is implemented by C++ code, including the materials of all sub-detectors and environment components. Fig. 5.2 shows the full Belle II geometry implemented in GEANT4, while fig. 5.3 and fig. 5.4 show the geometries of the VXD volume as implemented in Phase 2 and early Phase 3, respectively. These simulated background samples are used to add background to the simulated physics events. This process is called

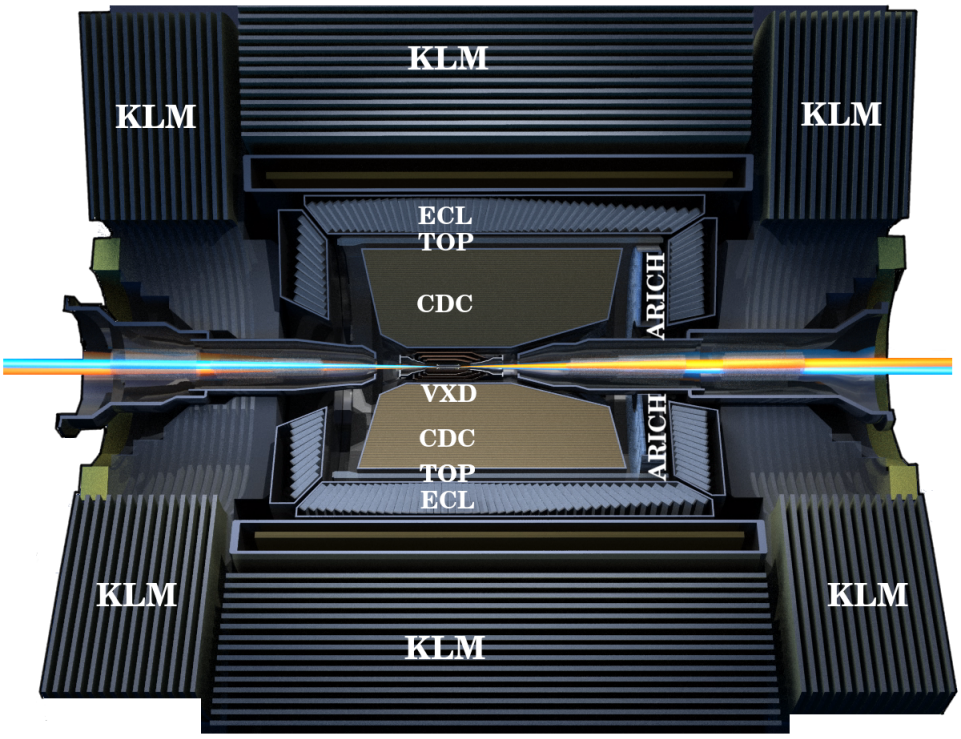

Figure 5.2: *Schematic view of the Belle II detector geometry implemented in GEANT4.*

"*background mixing*": an average number of background events of a given type is added to a single simulated physics event, with the average number determined from the rate of the particular background sample and the time window in which the background is mixed. The number of background events added is then generated with a Poisson distribution. To simulate contributions from a different bunch, the background events are shifted in time randomly within the time window. Hits in the sub-detectors are then digitised, so in the end a number of digitised hits is obtained for a single $B\overline{B}$ event without background and for the event with the background mixed.

5.4 Collimators optimization strategy

The conversion from macro-particle loss to loss rate allows to estimate the loss rate in the whole ring as a function of s, where s is the longitudinal coordinate parallel to the direction of motion of particles in the standard curvilinear coordinate system (x, y, s). In particular, for the optimisation of collimators apertures, the most important locations are the points where collimators are installed and the interaction region. The overall losses are considered for the estimation of the beam lifetime, which is calculated simply as the ratio between the initial number of particles in the beam and the loss rate. This approximation is valid since the maximum number of

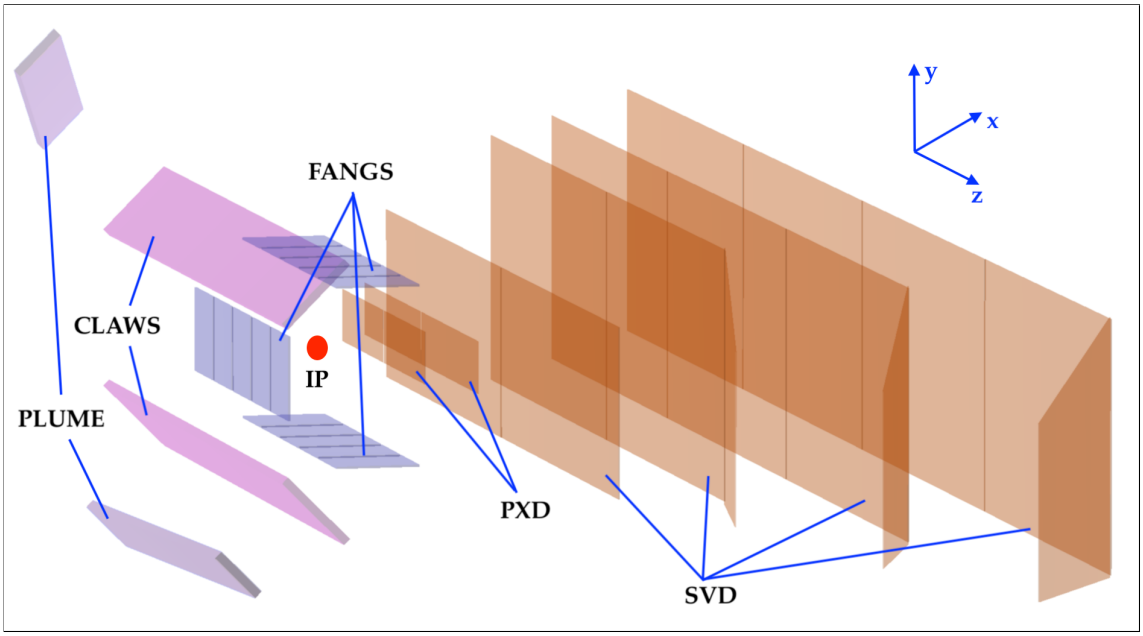

Figure 5.3: *Schematic view of the Phase 2 VXD volume geometry implemented in GEANT4.*

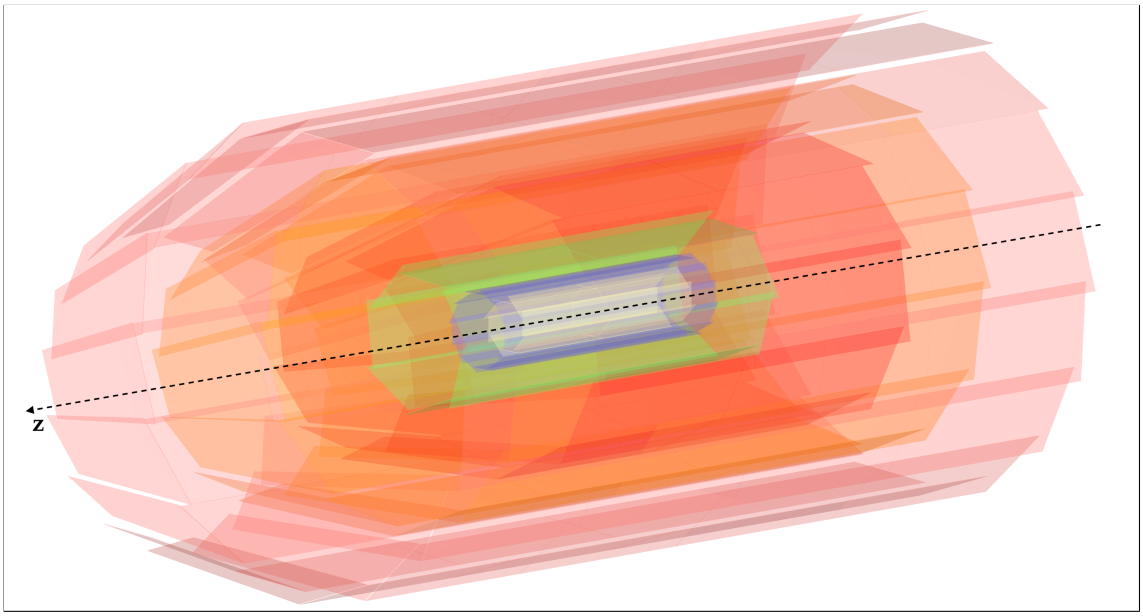

Figure 5.4: *Schematic view of the Phase 3 VXD volume geometry implemented in GEANT4.*

	Full sim		Fast sim	
	LER	HER	LER	HER
IR losses - Coulomb (MHz)	28.5	0.4	32.3	0.5
IR losses - Bremsstrahlung (MHz)	0.9	1.1	0.9	1.0
IR losses - Touschek (MHz)	49.6	8.9	45.6	8.4
IR losses - tot (MHz)	79.0	10.4	78.8	9.9
Lifetime - tot (s)	815	3564	801	3521

Table 5.1: *Comparison on IR losses and lifetimes between full and fast simulations. The biggest difference is in the total IR losses in HER, which differ by less than 5%.*

turns in the simulation corresponds to a few milliseconds, which is small enough to approximate the lifetime to the simple ratio:

$$\tau = \frac{N \cdot n_b}{R} \tag{5.4}$$

A full simulation, as previously described, takes around 24 hours to be completed, and since the number of simulations to be performed for the collimators study is large, a fast simulation is used, to save time, computing resources and disk space. With the fast simulation, only 25 macro-particles are used in the simulation, and only 20 jobs per background source are submitted, making the simulation much shorter ($\sim$3 hours against 24) and the data sample smaller ($\sim$450 MB against $\sim$5 GB). The statistics in these simulations is lower than in full simulations, but the number of macro-particles and of jobs to be run have been previously studied and it was verified that such statistics is a good compromise between reliable results and shortness of the simulation. A comparison between IR losses and lifetime obtained with the two types of simulations is shown in table 5.1.

The starting point of the optimisation procedure is the simulation with all collimators fully open. It's important to underline that a fully open collimator is not the same as excluding the collimator from the ring, since the aperture of the fully open collimator is smaller than the beam pipe radius, so even fully open collimators may have, even if small, an impact on the loss rate, especially if the beta function at the collimator location is rather big. A Gaussian distribution of particles is assumed in both horizontal and vertical directions, so collimators are assumed to absorb beam halo particles in the tails of the distributions. The fast simulation with collimators fully open gives the baseline of IR loss rate (background) and overall loss rate (lifetime). Then each collimator is closed independently in steps, with a fast simulation performed for each step of each collimator. For SuperKEKB type collimators, only one jaw at a time is closed, so the optimal aperture for both jaws is evaluated in-

Collimator setting	Overall losses (MHz)	IR losses (MHz)
Fully open	778	576
PMD02V1_4	778	576
PMD02V1_8	778	562
PMD02V1_12	778	450
PMD02V1_13	778	356
PMD02V1_14	927	258
PMD02V1_15	1273	220
PMD02V1_16	1915	199
PMD02V1_17	3331	178

Table 5.2: *Example of overall and IR losses when the bottom movable jaw of collimator PMD02V1 is closed in steps during the simulated collimator study for Phase 2. The increasing number in the first column indicates how many millimetres the jaw is closed from the fully open position.*

dependently. A data analysis script is used to analyse all simulation samples and extract from each simulation the information relative to IR losses and overall losses. In this way, a table like the one shown in table 5.2 is constructed, where losses for different collimator apertures can be compared.

As it can be seen from table 5.2 and from fig. 5.5, the first step has no impact on both losses, then the overall losses stay constant while IR losses decreases, meaning that those particles that were lost in the interaction region are now stopped by the collimator, without affecting beam lifetime. At some point overall losses start increasing, with IR losses still going down, so the collimator is now absorbing not only particles that are lost in the interaction region, but its effect is still important for the IR background reduction. When an increase in ring losses is compensated by a decrease in IR background, the collimator can still be closed by another step. If the decrease in IR losses is less than the increase in the overall losses, then the collimator is not working in the most efficient way and the previous step is considered the optimal one. In fig. 5.5, the optimal step corresponds to the vertical dashed line at the aperture of 6 mm. The same procedure is applied to all collimators of each ring.

After finding the optimal aperture for each collimator, a fast simulation with all collimators set in their optimal aperture is done, to see the effect of all collimators closed at the same time. The goal is to reduce IR losses for each ring below 100 MHz, a value that is considered reasonably safe for radiation damage and for detector performance. If the small simulation with the optimised collimator setting gives values of IR losses below 100 MHz, the optimisation procedure is considered finished and the collimator setting is considered as the ideal setting, otherwise a second iteration

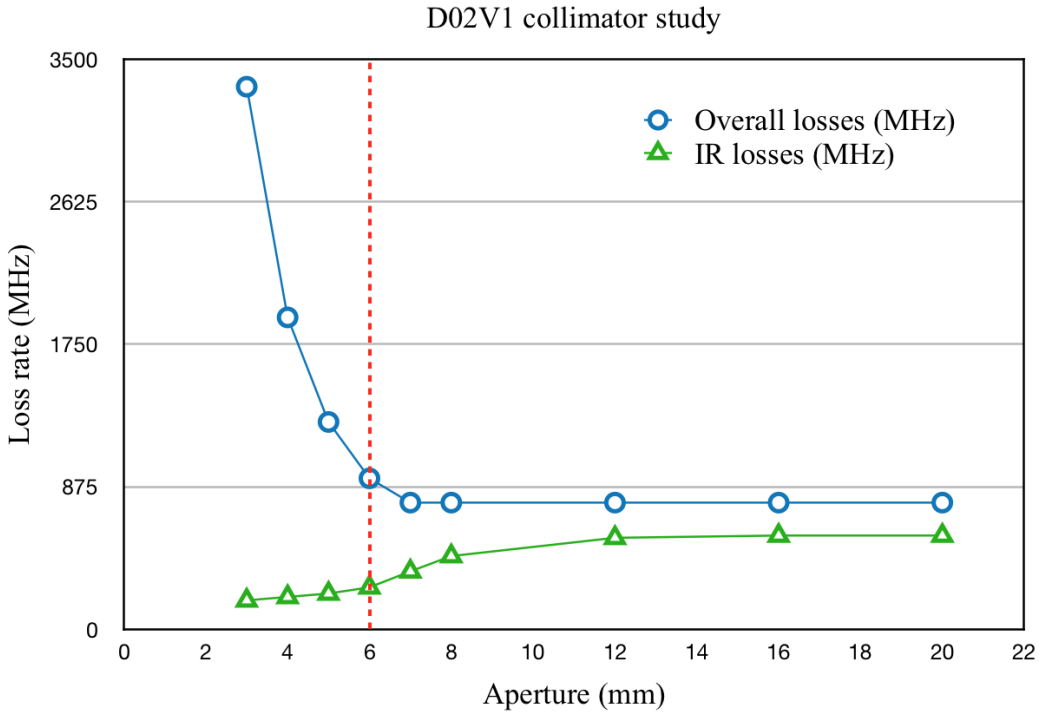

Figure 5.5: *Overall and IR losses for collimator D02V1 in the first iteration of a collimator study for Phase 2.*

of the described procedure is needed. Collimators are again closed in steps, but this time starting from the last optimised configuration. From the second iteration the requirement that the reduction in IR losses should correspond to a similar increase in overall losses is less strict, and the decision on the optimal collimator aperture is left to the judgement of the operator, who has to find the best compromise between the reduction in IR losses and the increase in overall losses. The operator should also consider two limits when closing collimators:

1. Losses on a single collimator should not exceed 100 GHz, that is the sustainable limit for the collimator, beyond this loss rate the collimator can suffer damage that would compromise it and affect beam conditions.

2. Collimators should not be closed more than the limits suggested by the study on the Transverse Mode Coupling Instability (TMCI), already explained in section 3.4.2. According to the results, apertures should not be smaller than 2 mm for all vertical collimators in both rings, while for horizontal collimators 7 mm is the limit set for HER, 8 mm the limit set for LER.

The optimization is considered completed when IR losses are less than 100 MHz. When an optimal collimators setting that satisfies all requirements is found, a full simulation is done to verify with higher statistics the results obtained with the fast simulation. The optimal collimator setting becomes a reference for operations with

the machine, and gives indications on the potential background reduction in the interaction region.

In the described optimization procedure, for each iteration collimators are optimized individually, not considering the impact that upstream collimators can have on downstream ones. The reason for using this simplified procedure is that this work has been done for Phase 2 and Early Phase 3, when the machine was still in a commissioning phase, with low currents and optics still far from the design ones, which means also that it is easier to reduce backgrounds below the 100 MHz level. The goodness of the optimization procedure was judged looking how much IR losses obtained with all collimators fully open were reduced with the optimized setting: in one of the preliminary study for Phase 2, for instance, IR losses were reduced from 642 MHz (fully open setting) to 51 MHz (optimized setting) for LER, and from 491 MHz (fully open setting) to 20 MHz (optimized setting) for HER. Another confirmation "a posteriori" came from simulations that are performed with collimators settings achieved during real operations: results from these simulations gave IR losses always higher than IR losses obtained in simulations with optimized settings. The advantage of this procedure is that collimators apertures can be studied in parallel for all collimators, reducing the time needed for the entire study and the computational resources used. In chapter 8, where studies for final Phase 3 parameters and optics will be presented, it will be clear that this procedure must be improved, and a possible new procedure will be proposed for future studies.

The study is clearly depending on machine optics, especially on the nominal values of vertical and horizontal betatron functions, dispersion, and on the number and location of installed collimators. Studies that will be presented in the following chapters are done for different optics and with a different number of collimators, so each time a study will be presented, a collimator map, the used optics and main beam parameters will be given.

Chapter 6

Phase 2 collimator studies

6.1 Collimator study on simulation for Phase 2

The first study performed with SAD background simulation was done during Phase 2 in 2018, after the machine established collisions and found a stable optics. The betatron function was gradually changed since collisions were established, going from $\beta_x^* = 200$ mm and $\beta_y^* = 8$ mm for both beams to the values shown in table 6.1 that were used for the background studies, and that are also assumed for the simulation studies reported in this chapter.

The optics files for the simulation were provided by the machine group and had the lattice components parameters that were used during real operation, so that the simulated lattice is as much as possible close to the real one.

6.1.1 Collimators aperture and betatron phase

It is known that once the lattice optics is defined, also the emittance is defined, and it does not depend on the position inside the ring, while the beta function, instead, is a function of s. The physical dimension of the beam, as shown in section 3.1, can

Parameter	Units	LER	HER
β_x^*	mm	200	100
β_y^*	mm	3	3
ε_x	nm	1.7	4.6
ε_y	pm	17	46
n_b		789	
I	mA	300	250
P	nTorr	1	

Table 6.1: *Parameters of Phase 2 used for background simulations.*

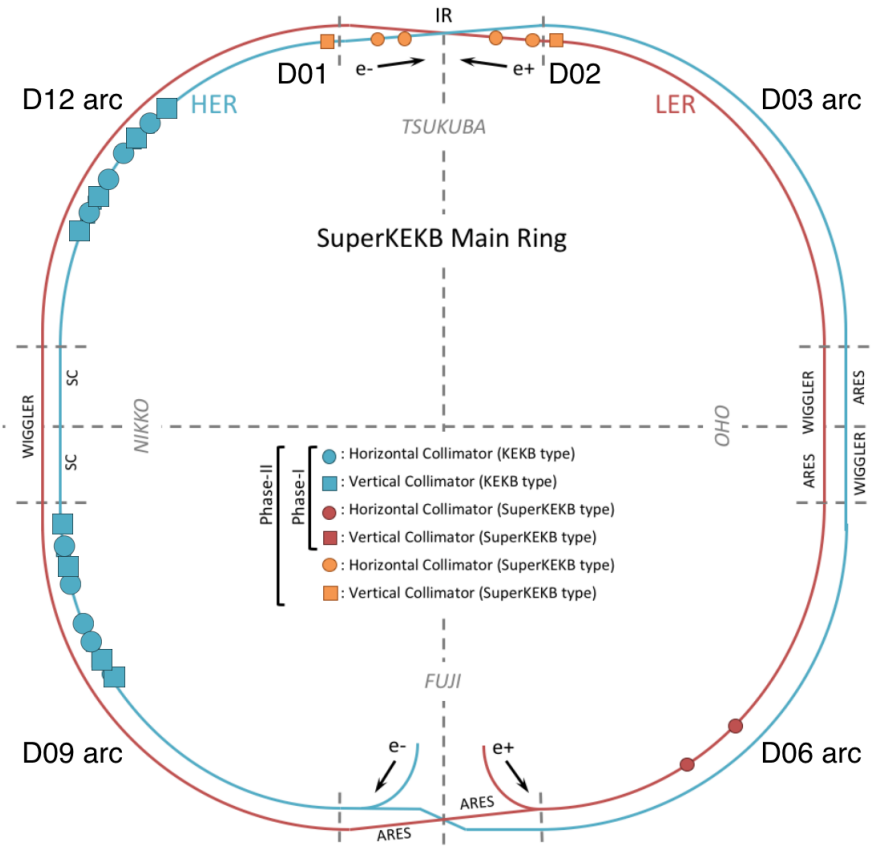

Figure 6.1: *Map of collimators installed in Phase 2.*

be estimated in horizontal and vertical directions according to equation (3.2):

$$\sigma_x(s) = \sqrt{\beta_x(s) \cdot \varepsilon_x + (\eta_x(s) \cdot \sigma_\delta)^2} \tag{6.1}$$

In SuperKEKB the energy spreads σ_δ, and thus ΔE, for both beams are:

$$\sigma_\delta(LER) = 8.1 \times 10^{-4} \qquad \Delta\mathrm{E}_{LER} = 8.1 \times 10^{-4} \cdot 4 \times 10^3 \mathrm{MeV} \simeq 3.2\mathrm{MeV} \tag{6.2}$$

$$\sigma_\delta(HER) = 6.4 \times 10^{-4} \qquad \Delta\mathrm{E}_{HER} = 6.4 \times 10^{-4} \cdot 7 \times 10^3 \mathrm{MeV} \simeq 4.5\mathrm{MeV} \tag{6.3}$$

Normalizing vacuum components apertures to the beam size σ is important because it allows a direct comparison of apertures in different positions of the ring. In particular, the components of final focus system, especially the beam pipe inside the QCS super conductive magnets, have the smallest physical apertures of the rings, which implies that if the beta function or dispersion are close to a maximum at QCS location, a lot of beam losses will happen on the QCS magnets, generating a lot of background in the interaction region and being a potential cause of QCS quenches. If it is possible to close collimators at a number of σ comparable to the one of QCS magnets beam pipe, this would avoid too much losses in the interaction region, improving background conditions and stability of machine operations.

In table **??** horizontal dispersion at the location of horizontal collimators is given. This dispersion is used to calculate the beam size at each collimator location using equation (6.1), and values are reported in the last column of table **??**. The effect of dispersion on the beam size is particularly relevant for D02H3 in LER and for D12 and D09 horizontal collimators. The contribution of dispersion in the beam size for these collimators is between 30% and 40%. In all following tables showing collimators apertures, together with the absolute value in mm, the aperture will be written also in number of σ, where σ is calculated with equation (6.1).

As discussed in section 3.1.1, together with the aperture, another important point is the phase advance between a collimator and other lattice components, in particular the component with the smallest aperture, like the beam pipe at QCS magnets positions. If the phase advance $\Delta\mu$ between a collimator and a QCS magnet is a multiple of π, the collimator will be very effective in reducing losses at that QCS magnet position, if the normalized aperture of the two elements is similar. If the phase advance $\Delta\mu$ is not a multiple of π, then the collimator should be closed more to be effective on background reduction, but in this case losses on the collimator will increase, as well as the wake field generated at the movable jaws, with the consequence that beam lifetime and stability will be affected. In tables 6.2 and 6.3 horizontal and vertical tune advances are reported for all collimators installed in Phase 2 and for the narrowest points of SuperKEKB lattice, that are some of

collimator ID	Horizontal tune ν_x	Dispersion η_x (m)	Horizontal betatron function β_x (m)	Beam size σ_x (μm)
LER				
D02-H1 ([a])	42.30	-0.06081	13.71	175.8
D02-H2 ([a])	42.74	0.74871	7.07	580.4
D02-H3	43.54	-0.90974	120.62	853.7
D02-H4	44.23	-0.39453	10.46	333.8
D03-H1 ([a])	38.42	0.76771	28.97	633.7
D06-H1 ([a])	24.99	0.69543	24.25	573.4
D06-H3	26.22	0.69543	24.25	573.4
D06-H4	26.70	0.69542	24.25	573.4
QC1 - horizontal	44.33	-2.0×10^{-5}	12.91	164.6
HER				
D01-H3 ([a])	0.85	-0.34833	5.43	270.3
D01-H4	0.51	-0.26861	27.57	394.4
D01-H5	0.29	-0.05679	19.28	299.9
D12-H4	7.09	0.72017	39.73	623.9
D12-H3	7.58	0.72019	39.73	623.9
D12-H2	8.24	0.72017	39.73	623.9
D12-H1	8.73	0.72019	39.73	623.9
D09-H4	14.34	0.72017	39.73	623.9
D09-H3	14.83	0.72019	39.73	623.9
D09-H2	15.49	0.72017	39.73	623.9
D09-H1	15.98	0.72019	39.73	623.9
QC2 - horizontal	0.24	-1.6×10^{-3}	249.46	1071.2

Table 6.2: *Horizontal betatrone tune, dispersion, beta function and beam size for all horizontal collimators and for the narrowest QCS components.*
([a]) Collimators that were added in early Phase 3.

the QCS elements inside the interaction region (-4 m $< s <$ +4 m). The tune is defined as the phase of the betatron oscillation normalized to 2π: $\nu = \mu/2\pi$. So the condition obtained in equation (3.9) becomes:

$$\Delta\nu = \frac{\Delta\mu}{2\pi} \quad ; \quad \Delta\mu = n\pi \quad \longrightarrow \quad \Delta\nu = n\frac{1}{2} \tag{6.4}$$

which means that if the tune advance between a collimator and the QCS beam pipe in tables 6.2 and 6.3 is a multiple of a half integer, the collimator is in the optimal location to reduce background at the QCS location.

collimator ID	Vertical tune ν_y	Dispersion η_y (m)	Vertical betatron function β_y (m)	Beam size σ_y (μm)
LER				
D02-V1	44.93	-4.0×10^{-13}	21.57	21.3
D06-V2 ([a])	30.54	3.2×10^{-13}	19.24	20.1
QC1 - vertical	46.33	-1.2×10^{-4}	241.73	71.2
HER				
D01-V1	1.27	-1.0×10^{-12}	15.03	26.3
D12-V4	6.65	4.7×10^{-13}	19.44	29.9
D12-V3	7.67	-1.0×10^{-12}	15.47	26.7
D12-V2	8.79	-4.0×10^{-13}	15.47	26.7
D12-V1	9.91	6.9×10^{-13}	16.75	27.8
D09-V4	13.17	1.8×10^{-12}	13.17	27.7
D09-V3	14.29	3.0×10^{-13}	15.47	26.7
D09-V2	16.60	2.2×10^{-12}	19.44	29.9
D09-V1	18.74	1.0×10^{-13}	15.47	26.7
QC1 - vertical	0.24	-1.5×10^{-6}	438.98	142.1

Table 6.3: *Vertical betatrone tune, dispersion, beta function and beam size for all vertical collimators and for the narrowest QCS components.*
([a]) Collimators that were added in early Phase 3.

6.1.2 Results of the collimator study

For the first collimator study with simulation, the procedure described in section 5.4 has been used. As shown in table 6.4, for HER, a good background reduction was achieved already after the first round of optimization, while for LER backgrounds in the interaction region were above the 100 MHz limit, so a second iteration was necessary. In this case, the optimized setting obtained after the first round of simulations was used as the starting point of the second iteration, and collimators were individually closed in steps, watching the change in IR backgrounds. In the right part of table 6.4, the background levels achieved after the second interaction are shown. The final optimized collimators settings for LER and HER after the second iteration are reported in tables 6.5 and 6.6, under the "SAD optimized setting" columns, with apertures expressed in mm and in number of σ. The optimized collimator setting was used as the goal for the experimental collimator study described in the next section.

6.2 Collimator study during Phase 2 operation

At the end of Phase 2, as part of the plan for background studies, some time was dedicated by the machine group, together with Belle II and BEAST groups, to find

	Fully open		1st iteration		2nd iteration	
	LER	HER	LER	HER	LER	HER
IR losses						
Coulomb (MHz)	590	261	79	0.3	48.7	0.3
Brems (MHz)	1	4	1	0.8	0.9	0.8
Touschek (MHz)	50	225	51	4.6	41.1	4.6
Tot (MHz)	641	490	131	5.7	90.7	5.7
Lifetime (s)	41701	8055	927	5641	698	5641

Table 6.4: *Comparison between first and second iteration of the collimator study performed for Phase 2.*

a good collimators setting that would reduce as much as possible the background levels in the interaction region. Three night shifts of 8 hours each were devoted to collimators studies.

The procedure was somehow similar to the one used in simulations, with an initial collimator setting used as starting point and with collimators closed individually in steps, observing the background rates of BEAST detectors and beam lifetime. The first study was performed with LER horizontal collimators, that was filled with 100 mA distributed in 789 bunches. Every time the current dropped to 80 mA, an automatic injection was performed to restore the 100 mA current. Although a rough optimization of collimators was done during operations, to study systematically the behaviour of each horizontal collimator it was decided to set all of them at an aperture of 65 σ, the same aperture of the narrowest point in QC1. Starting from the collimator closest to the injection point, and moving toward the interaction region, collimators were individually closed in steps. Given that all collimators installed in LER were of the SuperKEKB type, in order to save time it was decided to close both movable jaws of a collimator at the same time. The movement of the collimators jaws was commanded by the operator when the current in the ring was around 85 mA. With the injection being performed at 80 mA, there was enough time for the jaws to reach the new position. During injection, the associated background could be observed, then after injection was completed, storage background was observed. The big difference with respect to the simulation study was the possibility of observing injection background and tip scattering from collimators heads, which are not implemented in the simulation.

In fig. 6.2 the optimization process of collimator D06H3 is shown. The red line on top is the LER current, while the green line on the bottom is the beam lifetime. In the middle, rates measured by some BEAST detectors (He_3, CLAWS, PLUME, diamonds) are shown. In the top part of the plot, the orange line represents the D06H3

collimator aperture for both movable jaws. LER current increase corresponds to an injection, and BEAST detectors rates increase accordingly showing the injection background. During beam storage, a decrease in BEAST detectors rates follows the decrease in LER current. Right before each injection, a step in the aperture of the collimator is visible and corresponds to the moment when the collimator jaws are closed. In the first steps, a decrease in BEAST detectors rates can be clearly observed, with no reduction in beam lifetime. Then background rates slightly continue to go down, but the beam lifetime is also reduced. As indicated in the plot, the optimal aperture that minimizes storage and injection background keeping high beam lifetime is ± 14.0 mm.

In Phase 2, only four horizontal collimators were installed for LER, but it took a full night shift to perform a complete optimization. At the end of the procedure, to observe the effect of the optimization, collimators were open to the initial setting, and then closed all together to the optimized setting. The reduction in the background level was between 13% and 21%, depending on which BEAST detector is considered, as shown in the plot in fig. 6.3. After a first round of optimization, the new optimized setting was used as a starting point to further close collimators, trying to keep lifetime as long as possible and injection background as low as possible. In particular, it was possible to further close collimator D06H3 from the previous optimal aperture of ± 14.0 mm to ± 11.5 mm, which is the final optimal value that is also reported in the right column of table 6.5.

As for the LER, the same procedure was applied for the collimator study for HER. The top current was 230 mA instead of 100 mA, because the HER lifetime was much longer than the LER one and background levels lower, so to appreciate changes and have reasonable waiting times between two injections, this was the choice on the current, with injection performed when the current dropped to 202 mA and collimators moved at 205 mA. The initial setting of collimators was chosen at an aperture of 35 σ, which is the aperture of the narrowest point in QC2. In the HER there were many horizontal collimators, but in sectors D09 and D12 all horizontal collimators were of KEKB type, so with only one movable jaw. To save time, KEKB type collimators were closed two at a time, choosing those collimators with the same phase advance. In fig. 6.4 the optimization steps for collimators D09H1 and D09H2 (not visible in the plot because the aperture was the same as for D09H1) is shown, similarly to what has been shown for D06H3 optimization in LER, with the optimized aperture being -10.0 mm, at which both storage and injection backgrounds decreased with respect to the initial aperture. Also for HER, at the end of the optimization, collimators were opened at the initial setting and then closed all together to see the effect of the optimization, as shown in fig. 6.5, and a reduction up to 45% was recorded by BEAST detectors, as well as a good 35% reduction in

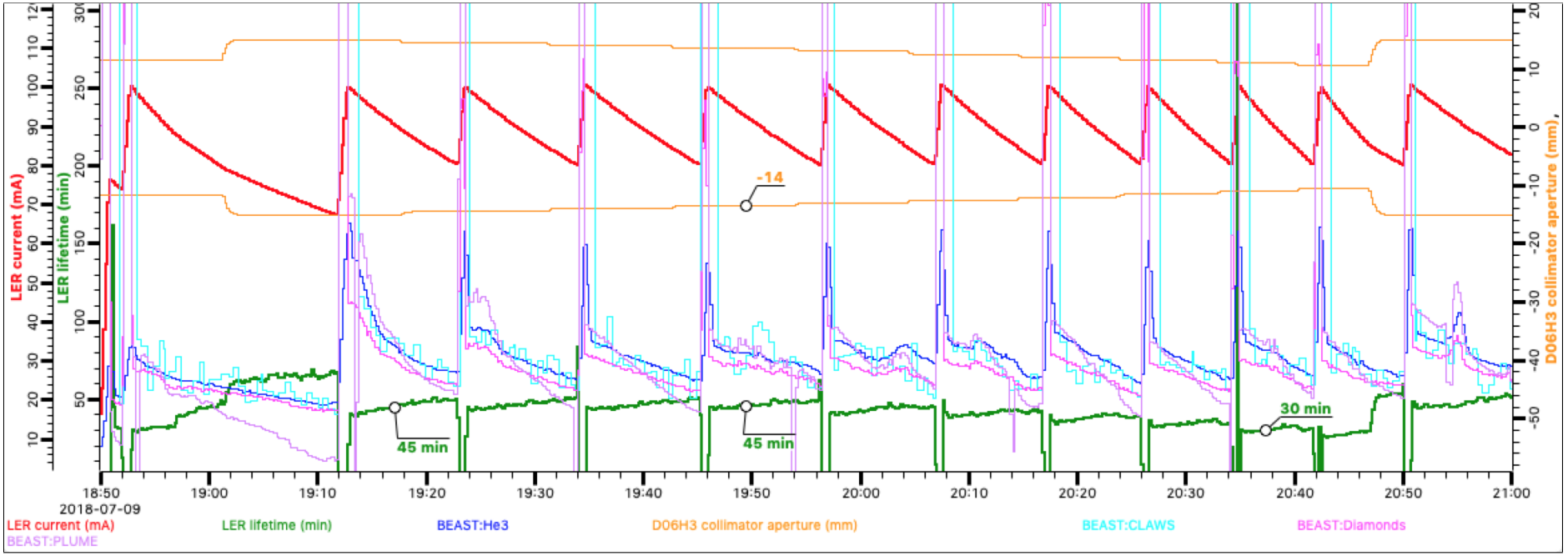

Figure 6.2: *Plot of some BEAST detectors variables during the LER collimators study of Phase 2. In the plot, the collimator D06H3 is closed gradually, and a decrease in background levels is observed, as well as a decrease in beam lifetime.*

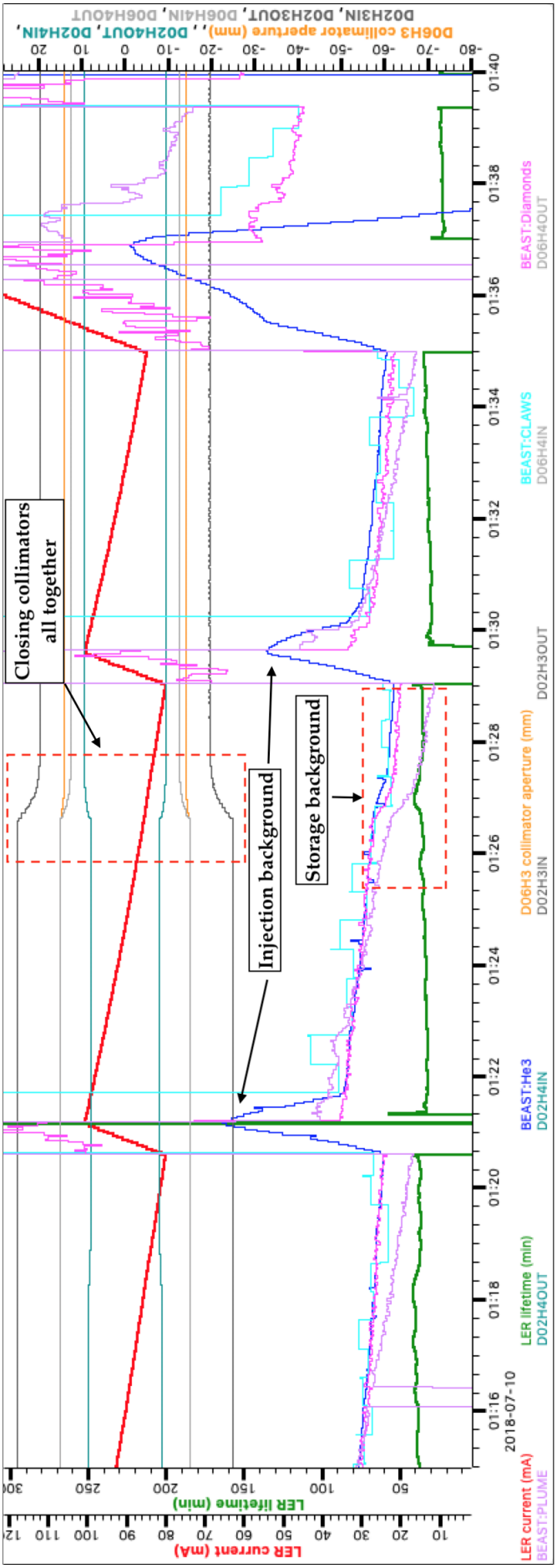

Figure 6.3: *Comparison between LER collimators settings at the beginning of the study and at the end of the study, after optimization. A background level reduction between 13% and 21% is observed in the BEAST detectors.*

LER	SAD optimized setting		Experimental setting	
collimator ID	Aperture (mm)	Aperture (σ)	Aperture (mm)	Aperture (σ)
D02-V1-TOP	2.0	94	N/A	N/A
D02-V1-BTM	2.0	94	N/A	N/A
D02-H3-OUT	23.0	27	19.5	23
D02-H3-IN	-21.0	25	-19.5	23
D02-H4-OUT	7.0	21	9.5	28
D02-H4-IN	-7.0	21	-9.5	28
D06-H3-OUT	12.0	21	11.5	20
D06-H3-IN	-13.0	23	-11.5	20
D06-H4-OUT	11.0	19	11.0	19
D06-H4-IN	-13.0	23	-11.0	19
QC1 - horizontal	10.5	64		
QC1 - vertical	13.5	189		

Table 6.5: *LER - Comparison between the optimized setting found with simulation and the experimental collimators configuration. "N/A" means that the collimator couldn't be optimized.*

injection background. Unfortunately, after the optimization of horizontal collimators there was no time left for the optimization of vertical collimators, only D12V1 was slightly closed and a good reduction of injection background was observed, but no further optimization was possible.

For both rings, the goal was to reach at least the collimators settings optimized with SAD simulation. The settings achieved during operations are reported in tables 6.5 and 6.6, under the "Experimental setting" columns. In LER, collimators in the D06 sector were set more or less at the same aperture obtained with SAD, while in the D02 sector the collimator closest to the IP, D02H4, was left wider because of injection background and D02H3 was closed more than in the SAD simulation. In HER collimators D01H5, D12H4 and D12H3 were set as in the simulation, while all other collimators in sectors D12 and D09 were closed much more than in simulation, because they were very sensitive to injection background, which is not considered in simulation. D01H4 could not be closed more than ± 18.0 mm because of a sudden increase in background levels and in losses at the near loss monitor, that in some cases triggered a beam abort due to too much losses. The reason was not well understood, and as it will be shown in the next chapter, also during early Phase 3 this collimator could not be closed as desired.

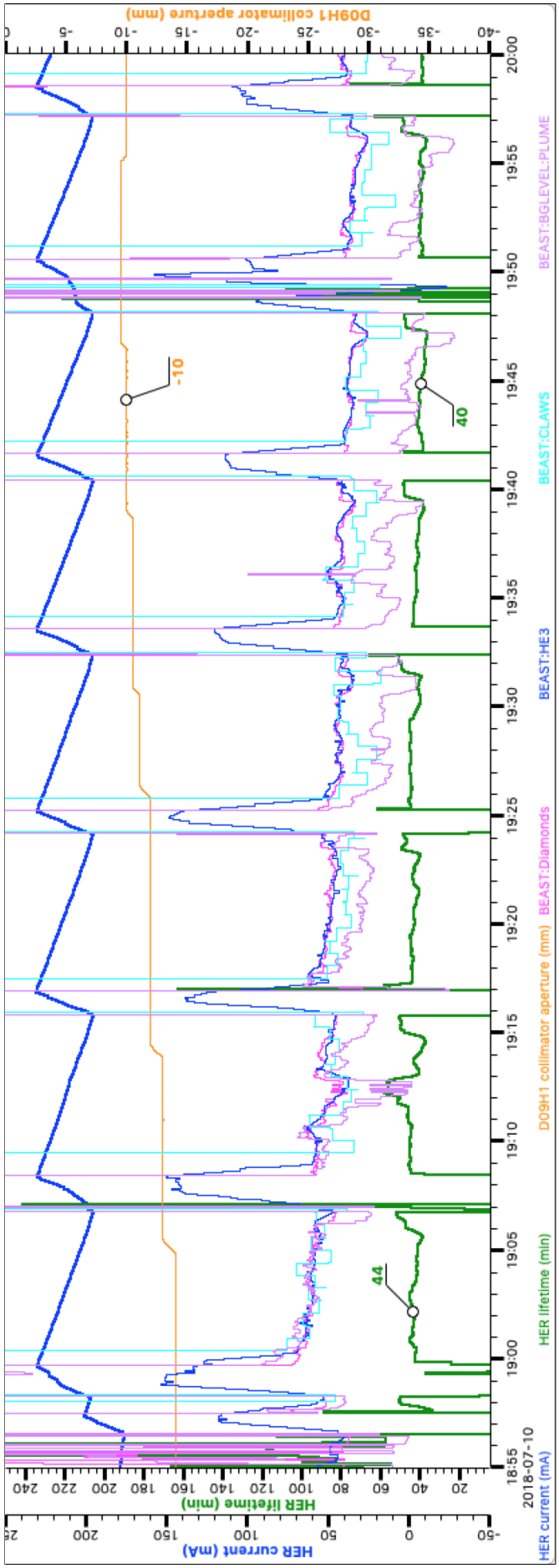

Figure 6.4: *During the HER collimators study of Phase 2, the collimator D09H1 is closed gradually together with D09H2 (not visible in the plot), and a decrease in background levels is observed, with a very small decrease in beam lifetime.*

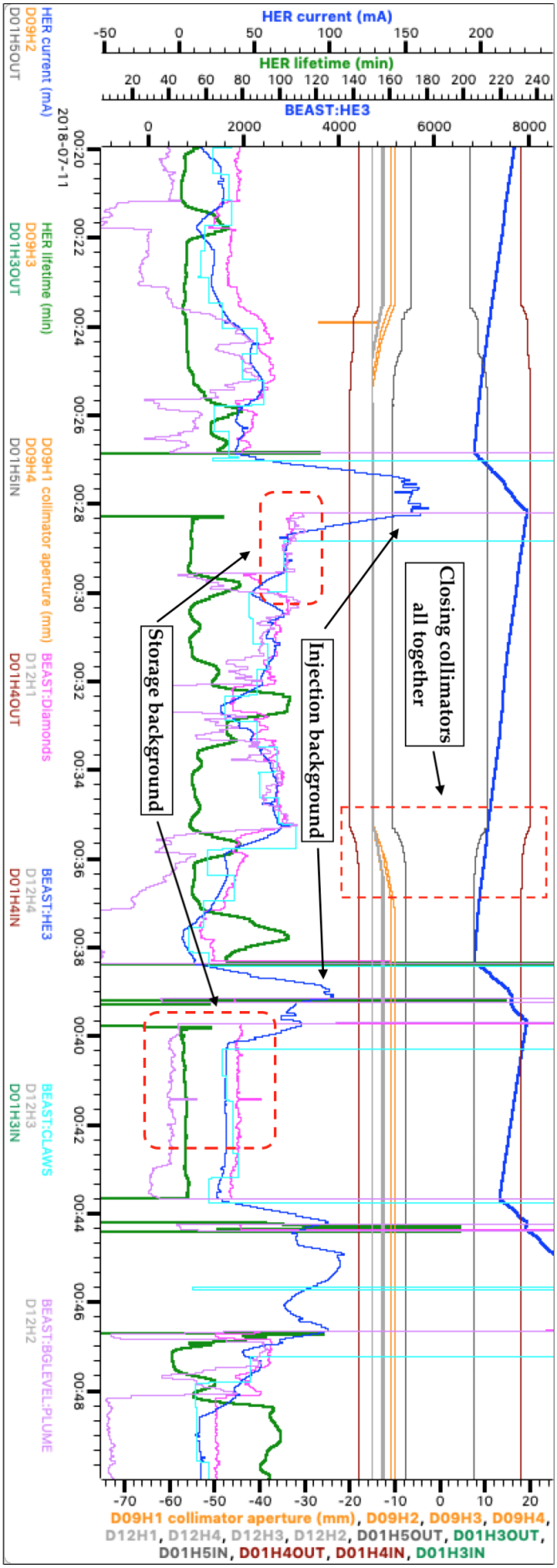

Figure 6.5: *Comparison between HER collimators settings at the beginning of the study and at the end of the study, after optimization. A background level reduction between 30% and 45% is observed in the BEAST detectors.*

HER	SAD optimized setting		Experimental setting	
collimator ID	Aperture (mm)	Aperture (σ)	Aperture (mm)	Aperture (σ)
D01-V1-TOP	2.0	76	N/A	N/A
D01-V1-BTM	-2.0	76	N/A	N/A
D01-H4-OUT	13.0	33	18.0	46
D01-H4-IN	-15.0	38	-18.0	46
D01-H5-OUT	8.0	27	7.5	25
D01-H5-IN	-8.0	27	-7.5	25
D12-V4-BTM	-2.5	84	N/A	N/A
D12-H4-IN	-15.0	24	-15.0	24
D12-V3-TOP	2.5	94	N/A	N/A
D12-H3-IN	-12.0	19	-13.0	21
D12-H2-IN	-19.0	30	-12.5	20
D12-V2-BTM	-2.5	94	N/A	N/A
D12-H1-IN	-17.0	27	-12.5	20
D12-V1-TOP	2.5	90	4.0	144
D09-V4-BTM	-2.5	90	N/A	N/A
D09-H4-IN	-20.0	32	-13.0	21
D09-V3-BTM	-2.5	94	N/A	N/A
D09-H3-IN	-16.0	26	-13.0	21
D09-H2-IN	-15.0	24	-11.0	18
D09-H1-IN	-15.0	24	-10.0	16
D09-V2-BTM	-2.5	84	N/A	N/A
D09-V1-BTM	-2.5	94	N/A	N/A
QC2 - horizontal	35.0	33		
QC1 - vertical	13.5	95		

Table 6.6: *HER - Comparison between the optimized setting found with simulation and the experimental collimators configuration. "N/A" means that the collimator couldn't be optimized.*

6.3 Background evaluation at the end of Phase 2

After collimators optimization, other background studies were performed in order to evaluate the background components. The first step was to make single beam studies and separate the two dominant single beam background sources, beam-gas Coulomb scattering and Touschek scattering. During these studies, only one beam was circulating in the machine with the nominal beam size, and data were recorded by BEAST and Belle II detectors. The optimized collimator setting found during the experimental collimator studies was used. The observable for the detectors, usually a rate of events, can be expressed as follows [52]:

$$Obs. = T\frac{I^2}{\sigma_y n_b} + BIPZ_{eff}^2 \tag{6.5}$$

Where T and B are the coefficients of the beam-gas and the Touschek contributions, P is the residual gas pressure in the beam pipe and Z_{eff} is the effective atomic number of the residual gas. The effective atomic number has been studied during Phase 1 using the residual gas analyzers (RGA) installed in the rings, and the results were consistent with the value $Z_{eff} = 7$ that was also assumed in simulation. Regarding pressure, SuperKEKB is equipped with cold cathode pressure gauges (CCG) installed approximately every 10 m to measure the pressure of residual gas in the beam pipe. Due to their proximity to vacuum pumps, the pressure measured by CCGs is actually lower than the one seen by the beams, so a correction is applied to the measured pressure. In particular, given that the total pressure can be considered as the sum of a dynamic pressure and a base pressure that remain in the beam pipe long after beams are not circulating anymore, the correction is applied only to the dynamic component, so the pressure seen by beams can be expressed as:

$$P_{beam} = A \cdot P_{CCG} - (A-1)P_0 \tag{6.6}$$

where P_{CCG} is the measured pressure, P_0 is the base pressure, A is 1.7 for LER and 3 for HER. After the first measurement of background rates was done, the beam size was changed twice, keeping the beam current and the number of bunches unchanged, so that only the Touschek component would change. Re-normalizing the observable rate, the previous equation can be written in such a way that data would lie on a straight line, whose intercept with the y-axis would give the B coefficient, while the slope would give the T coefficient:

$$\frac{Obs.}{IPZ_{eff}^2} = T\frac{I}{PZ_{eff}^2\sigma_y n_b} + B \tag{6.7}$$

BEAST and Belle II detectors participated to the background studies to evaluate

	Phase 2	
	LER	HER
B [10^4%/(mA·Pa)]	1.74	0.72
T [%·μm/(mA)^2]	0.075	0.023

Table 6.7: *B and T coefficients evaluated for SVD in Phase 2.*

	Phase 2 BG study	
	LER	HER
IR losses - Coulomb (MHz)	46.5	0.3
IR losses - Brems (MHz)	0.5	0.5
IR losses - Touschek (MHz)	20.0	4.1
IR losses - tot (MHz)	67.0	4.9
Lifetime - tot (s)	1692	6826

Table 6.8: *Background levels and lifetimes obtained with simulation of Phase 2 optics and the real collimators setting achieved during the experimental collimators study and used for background studies.*

single beam background components. For the SVD sub-detector the observable quantity was the occupancy of Layer 3 sensors. Re-normalizing SVD occupancy as shown in formula 6.7, the plots shown in fig. 6.6 were obtained. In Phase 2 only one SVD Layer 3 ladder was installed, so the occupancies were available only for two Layer 3 sensors. B and T coefficients for SVD, shown in table 6.7, were evaluated from the plots using data of the sensor where the background was higher. LER background dominates for both beam-gas and Touschek backgrounds with respect to HER, by a factor 2 and 3 respectively.

A SAD simulation was done with the collimator setting used during background studies, and background levels are shown in table 6.8. Also in the simulation LER beam-gas is the dominant component in both cases, but there is one order of magnitude difference between LER and HER backgrounds, which is different from what has been observed in data.

6.3.1 Data/MC ratios and background extrapolation

The SAD simulation of the background studies was used to run the full simulation, including the GEANT4 part, to get the simulated observable quantities for BEAST and Belle II detectors. In this way it was possible to compare data with simulation

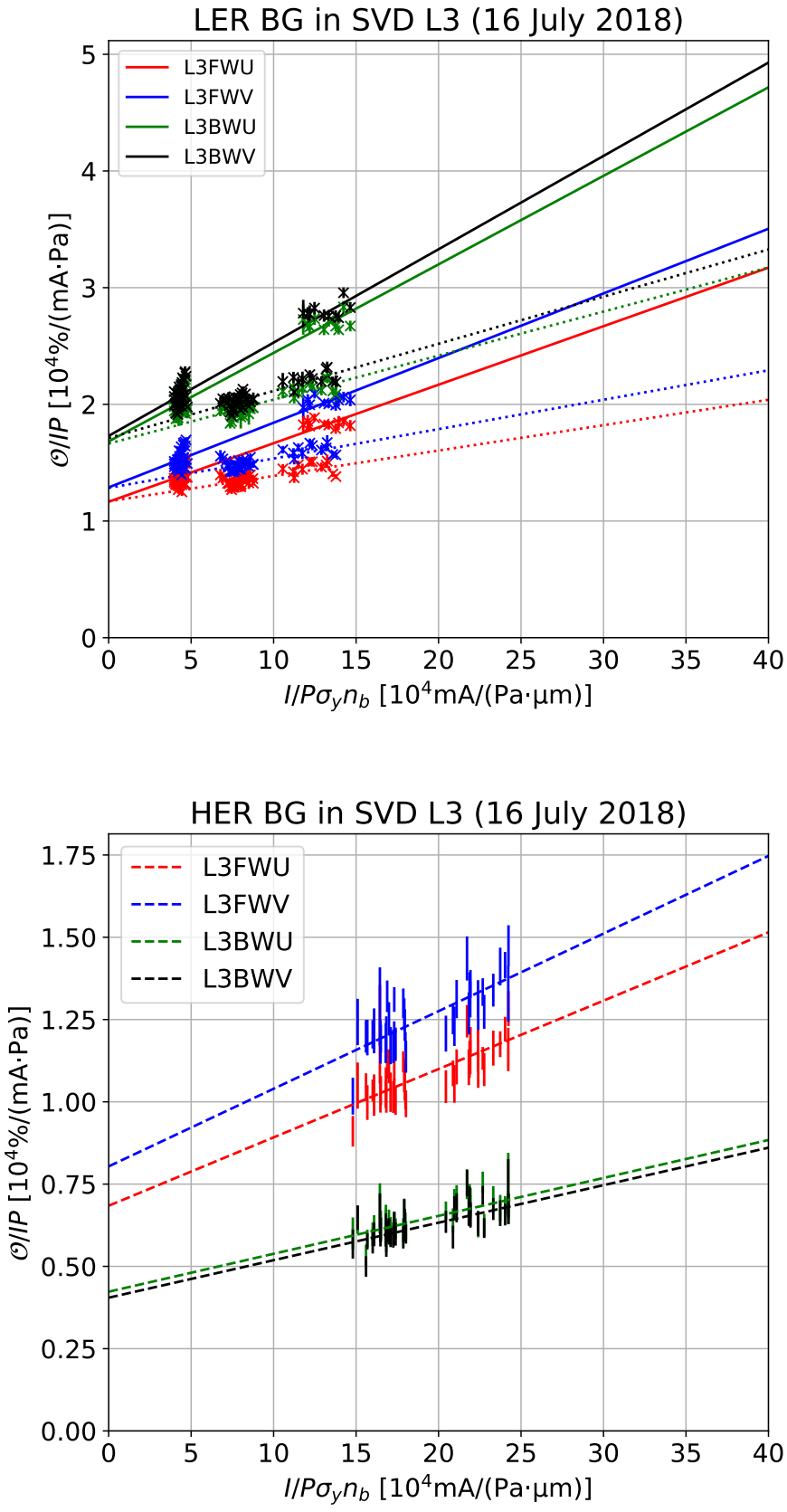

Figure 6.6: *Phase 2 background studies results for SVD. The observable is the occupancy for Layer 3 sensors. B and T coefficients were extracted from BWD sensors data.*

	Phase 3 MC occupancy (%)	Phase 2 "data/MC"	Phase 3 occupancy prediction (%)
HER beam-gas	0.008	600	4.8
HER Touschek	0.0008	1700	1.4
HER tot.			**6.2**
LER beam-gas	0.14	39	5.5
LER Touschek	0.24	4.6	1.1
LER tot.			**6.6**

Table 6.9: *Estimation of SVD occupancy for layer 3 sensors using the occupancy predicted by Phase 2 simulation and the "data/MC" factors calculated after background studies in Phase 2.*

and to get "data/simulation" ratios, called hereafter "data/MC" for abbreviation, that are useful on one side to understand how far is the simulation from representing the real system, and on the other side can be used to make an extrapolation of background levels to the final optics. In the second column of table 6.9, data/MC ratios calculated for SVD Layer 3 sensors occupancies are shown for each ring and for each background component. As all ratios are far from 1, it is clear that the simulation, at this stage, was not representing very well the system, suggesting that some actions should have been taken in order to improve simulation reliability.

The data/MC ratios were also used by SVD group to estimate the expected background levels for final Phase 3 optics and machine parameters, using the existing final Phase 3 simulation and applying to the simulated values of the occupancy the data/MC ratios just calculated. The extrapolation is shown in table 6.9: in the first column, simulated occupancies are shown for each ring and for each background source; these occupancy values are then multiplied by the Phase 2 data/MC ratios. The extrapolated values of each occupancy are shown in the rightmost column of the table. It looks clear that with these occupancies it would be impossible for SVD to run properly, even considering only single beam backgrounds, so some countermeasures must be taken into account to improve background conditions.

A different scaling was done for early Phase 3: given that the optics to be used in early Phase 3 was the same used for Phase 2 background studies, it was sufficient to scale the backgrounds to the machine parameters that were expected to be used in early Phase 3. For the VerteX Detector, and SVD in particular, the result of this extrapolation was that a reduction by a factor 2 was necessary in background levels to avoid detector performance degradation due to too high occupancy levels. However, it was already planned to install new collimators in both rings, so a reduction on background levels was somehow expected, but it was not studied nor quantified yet. Simulations were performed in order to understand

the impact of new collimators, and results are reported in the next chapter. The installation of the VerteX Detector was then considered safe and it took place in November 2018.

An estimation of luminosity background was tried during collision runs. To do so, Touschek and beam-gas background components previously measured must be subtracted to the overall background recorded by detectors. Unfortunately, machine conditions during collision runs turned out to be much different than during single beam background studies, meaning that Touschek and beam-gas components were different and they could not be properly subtracted from the overall background levels. Thus the estimation of luminosity background was quite difficult and meaningless, and it was postponed to Phase 3.

Chapter 7

Early Phase 3 collimator studies

7.1 Updates from Phase 2

7.1.1 New hardware components

During the shutdown between the end of Phase 2 and the start of Phase 3, in addition to the completion of the Belle II detector with the insertion of the full VerteX Detector, some collimators were installed in both rings. The added collimators are shown in fig. 7.1. One horizontal collimator was added in the Tsukuba straight section of the HER (sector D01), while the biggest modifications happened in the LER, where two horizontal collimators were added in the Tsukuba straight section (sector D02), one more was added in the D03 arc section, and one vertical collimator was added in the D06 arc section, close to the LER injection point. In addition, D06H4 collimator was moved to D06H1 position, because both D06H4 and D06H3 collimators were on the same betatron phase, so it was decided to move one of them to another position, where the tune advance was different. All new collimators were of the SuperKEKB type.

Inserting the full VXD, the BEAST detectors were moved out of the VXD volume, so a direct comparison between background levels with those detector was not possible. But the diamond system, that in Phase 2 consisted of only 8 sensors in the VXD volume around the beam pipe (4 on the backward side and 4 on the forward side), has been improved, adding 12 sensors around the SVD support cones and 8 sensors around the QCS bellows pipes. QCS bellows pipes sensors turned out to be very sensible to injection background and could separate the background source between LER and HER, because in that location the two beam pipes are already separated, so two sensors were positioned around the LER beam pipe and two were positioned around the HER beam pipe. Thus the diamond system has been used extensively to monitor injection and storage background levels in the interaction region during the early Phase 3 run.

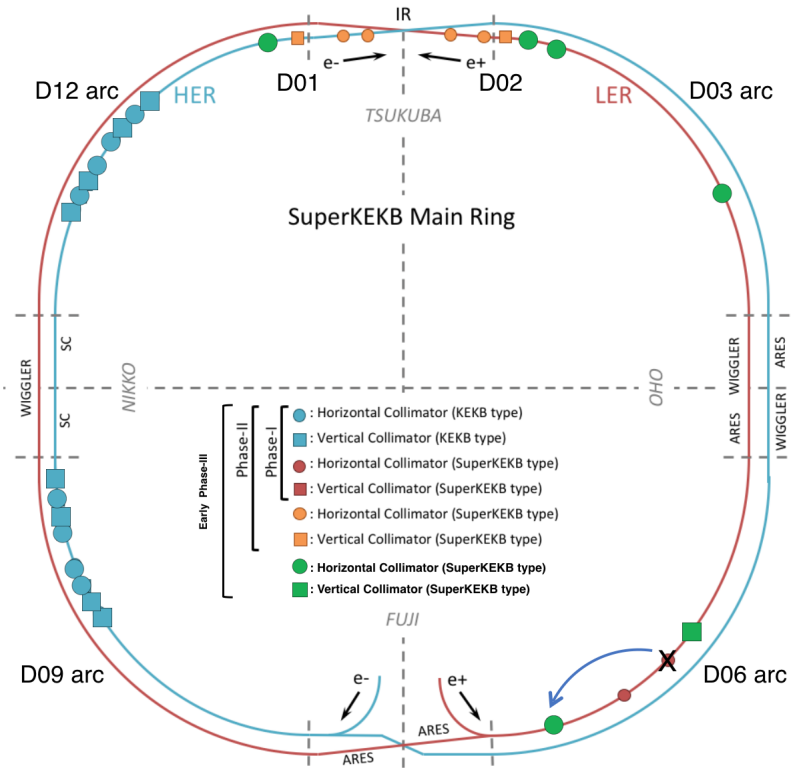

Figure 7.1: *Map of collimators installed in the spring run of Phase 3.*

7.1.2 Simulation update

The big discrepancy observed between data and simulation in Phase 2 background studies suggested to revise part of the simulation to spot possible inconsistencies between the simulated model and the real system. In particular, the GEANT4 model and the script that analyses the SAD output files to generate ROOT files were considered, and after a crosscheck with latest drawings of the interaction region, the following changes were implemented:

- The material of part of the beam pipe in the interaction region has been changed in the GEANT4 model, from tantalum to grade 316L stainless steel.
- In the GEANT4 geometry, an obsolete tungsten shield has been removed around the QCS of the forward region, while on the backward side another shield was added to the model.
- In the GEANT4 model, it was noted that the beam pipe geometry was not exactly corresponding to the latest CAD drawing, so some modifications that were done on the real beam pipe design were not considered. These modifications were implemented in GEANT4 in order to reduce the inconsistency.
- It was noted that there were some offsets in x or y directions in the real QCS beam pipe that were not considered in SAD. What can happen in this cases is

	Phase 2 "data/MC" old geometry	"updated/old" geometry	Phase 2 "data/MC" updated geometry
HER beam-gas	610	11.0	55
HER Touschek	1600	7.8	205
LER beam-gas	39	4.2	9.3
LER Touschek	4.6	3.0	1.5

Table 7.1: *Updated data/MC ratios after geometry updates in the simulation. The scaling factors are all reduced, and for LER they are closer to 1, meaning good agreement between background predictions and measurements.*

that if particle is lost in the SAD simulation and then passed to GEANT4, and the radial position of this particle is already beyond the GEANT4 model of the QCS beam pipe inner surface, then the interaction with beam pipe material is underestimated, and so will be the simulated background. To overcome this inconsistency, the script that analyses the SAD output files was modified in order to move those particles that are lost in the QCS region exactly where the inner surface of the QCS beam pipe is in the real system. With the additional improvement of the GEANT4 model, made similar to the real QCS geometry, this modification allowed a more realistic representation of the interaction between lost particles and the surrounding environment.

- The shape of the beam pipe in the SAD simulation is circular, because it's not possible to implement other geometries. A circular beam pipe is a good approximation along the ring, but it's not good in the QCS region, where the shape is elliptical, the physical aperture is small and losses are more probable. It was decided to translate the position of lost particles on an elliptical shape beam pipe and match the QCS beam pipe geometry implemented in GEANT4.

The Comparison between new and old geometry must be done after running the GEANT4 simulation, because the SAD output, in terms of loss rate of particles, is the same, even the changes described in the fourth point are actually reflected on the X-Y position of the loss particles that are passed to GEANT4. The comparison therefore depends on the sub-detector considered. For SVD, whose "data/MC" ratios have been calculated in section 6.3, factors between 3 and 11 are obtained for background levels, as shown in table 7.1. This means that the updated geometry really improved the predictions on backgrounds, and the discrepancy factors observed in table 6.9 can be partially or totally compensated, as for LER Touschek. Results on the new ratios between data and simulations for early Phase 3 will be reported in section 7.3.

Parameter	Units	LER	HER
β_x^*	mm	200	100
β_y^*	mm	3	3
ε_x	nm	1.7	4.6
ε_y	pm	17	46
n_b		1576	
I	mA	1200	1000
P	nTorr	1	

Table 7.2: *Parameters of early Phase 3 used for background simulations.*

7.2 Collimator study on simulation for early Phase 3

The first run of Phase 3, started on March 11th 2019, has been called "early Phase 3" run. The plan for early Phase 3 was to restart with the same optics used at the end of Phase 2, re-establish collisions as soon as possible, then start optimizing the machine and collect the first physics data, and possibly move to new optics by the end of the run in June. The machine was able to resume operations pretty quickly, with first collisions in Phase 3 that happened on March 26th. Unfortunately, after a few days a fire accident near the Linac building forced the machine to stop operations for four entire weeks, loosing precious time. The integrated luminosity at the end of the run was affected, with only 6.5 fb^{-1} collected, against the goal of 10 fb^{-1} that was set before the start of the run. The same optics was kept for the remaining part of the run, except the last week, when the machine group performed studies to go to a $\beta_x^* = 80$ mm and $\beta_y^* = 2$ mm optics.

Given that new collimators were installed between Phase 2 and early Phase 3, new simulations were done in order to understand their impact on the background levels. With the optics being the same, the only parameters that were changed were the total current, increased by a factor 4, and the number of bunches, increased by a factor 2, as summarized in table 7.2.

As in Phase 2, a simulated collimator study was performed in the same way described already in chapter 6.1, with the same strategy explained in section 5.4. The goal was still to keep the background rate in the interaction region below 100 MHz for each beam. For the HER collimator study, the experience during Phase 2 was used to put a constraint on the D01H4 collimator: during Phase 2, it was not possible to close this collimator as much as it was thought, for reasons not well understood. To make an optimization as much as possible close to reality, the aperture of D01H4 collimator was fixed at ± 15 mm. All the other collimators were

	Phase 2 BG study		Early Phase 3 optimized	
	LER	HER	LER	HER
IR losses - Coulomb (MHz)	186	1.2	28.6	0.4
IR losses - Brems (MHz)	2.0	2.0	0.9	1.1
IR losses - Touschek (MHz)	160	32.8	49.6	8.9
IR losses - tot (MHz)	348.0	36.0	79.1	10.4
Early Phase 3/Phase 2 ratio			0.23	0.29
Lifetimes (s)	909	3971	815	3564

Table 7.3: *Comparison between the simulation done with the experimental setting of Phase 2 background studies (scaled to beam parameters of early Phase 3) and the simulation done with the optimized setting for early Phase 3.*

individually closed in steps as usual, and an optimal collimator setting was found. The optimal collimators settings are shown in the "SAD Optimized setting" column of table 7.4 for LER and of table 7.5 for HER.

With these optimized settings, a full simulation was done, and was compared with the simulation done for Phase 2 BG study (same optics, collimator setting optimized during operations) to observe differences in the background levels. With a comparison between simulations it is possible to get expectations on the change in background levels. These expectations will be compared later with the background difference between Phase 2 and early Phase 3 data. A direct comparison of the rates was not possible due to the different beam parameters between the two simulations, so a scaling of results obtained for Phase 2 settings was necessary. Touschek background scales with I^2 and $1/n_b$, so given the factor 4 in the currents and the factor 2 in the number of bunches, to scale Touschek background rates to early Phase 3 parameters, the rates were multiplied by a factor 8. No scaling for the beam size was needed, since optics in the two studies were the same. For the two beam-gas background sources, instead, the dependence is limited to I, so only a factor 4 was necessary to scale background levels. The comparison between scaled Phase 2 rates and lifetimes and early Phase 3 ones is shown in table 7.3. As it can be seen, loss rate ratios between early Phase 3 optimized and Phase 2 BG study are **0.23 for LER** and **0.29 for HER** backgrounds, while lifetimes are almost unchanged. This is a comparison between a collimator setting that was actually used during Phase 2 and a setting for Phase 3 that works on simulation, so it was not obvious that the same reduction could be achieved during early Phase 3, but it was a first indication that new collimators could have a good impact on background reduction.

7.2.1 Loss position in the interaction region

Other indications can be extracted from simulation regarding the position of the losses in the interaction region. The losses can be plotted as a function of s for the three background sources, as shown in fig. 7.2. For LER, the highest losses are concentrated around $s = +1.2$ m and $s = -1.2$ m, which is consistent with the position of components with the smallest aperture in the ring (QCS). For the HER is a bit different, because the highest losses in the interaction region do not correspond to the location of the narrowest aperture of QCS, at $+3.0 < s < +2.8$, it looks like the highest losses are downstream the IP, in the interval at $-2.6 < s < -1.6$. It is also interesting to note that the highest losses are not coming close to the interaction point, at $|s| < 1.0$. The distribution of losses is important also for the interpretation of studies done on Phase 2 data. A study was performed on reconstructed vertices of events recorded by the Belle II detector during single beam studies: usually events are processed using a cut on the z-position of the reconstructed vertices, so that they must be close to the nominal position of the interaction point, but for this study the cut was not applied and vertices could be in any position within ± 0.8 m from the nominal position of the interaction point. The result of this study was the plot in fig. 7.3, that shows how reconstructed vertices are distributed in the region $|s| < 0.8$. From the plot, some "hot spots" are visible in different locations, depending if the beam is circulating in the LER or in the HER. The number of events observed in that region is somehow consistent with the SAD/GEANT4 simulation, that actually gives a rate of events slightly higher than what is observed. However, looking at the distribution of losses in fig. 7.2 it can be seen that the highest losses in the IR are coming outside of the region covered by the reconstructed vertices study, so the loss distribution as a function of s suggests that the higher contributions to beam background are coming from $|s| > 0.9$ for both beams. In fact, the positioning of additional shields is actually taken into consideration to mitigate background coming from $|s| > 1.0$.

7.3 Collimator study during early Phase 3 operation

The first experimental collimator study in Phase 3 started on April 3rd. This was the only collimator study done in April, because then operations were stopped for four weeks due to the fire accident. So the quantitative results of this study on HER were not particularly meaningful, but there was an important indication that was used for the next studies performed in May. In Phase 2 there was no time to make studies on vertical collimators, so some time was dedicated to the study

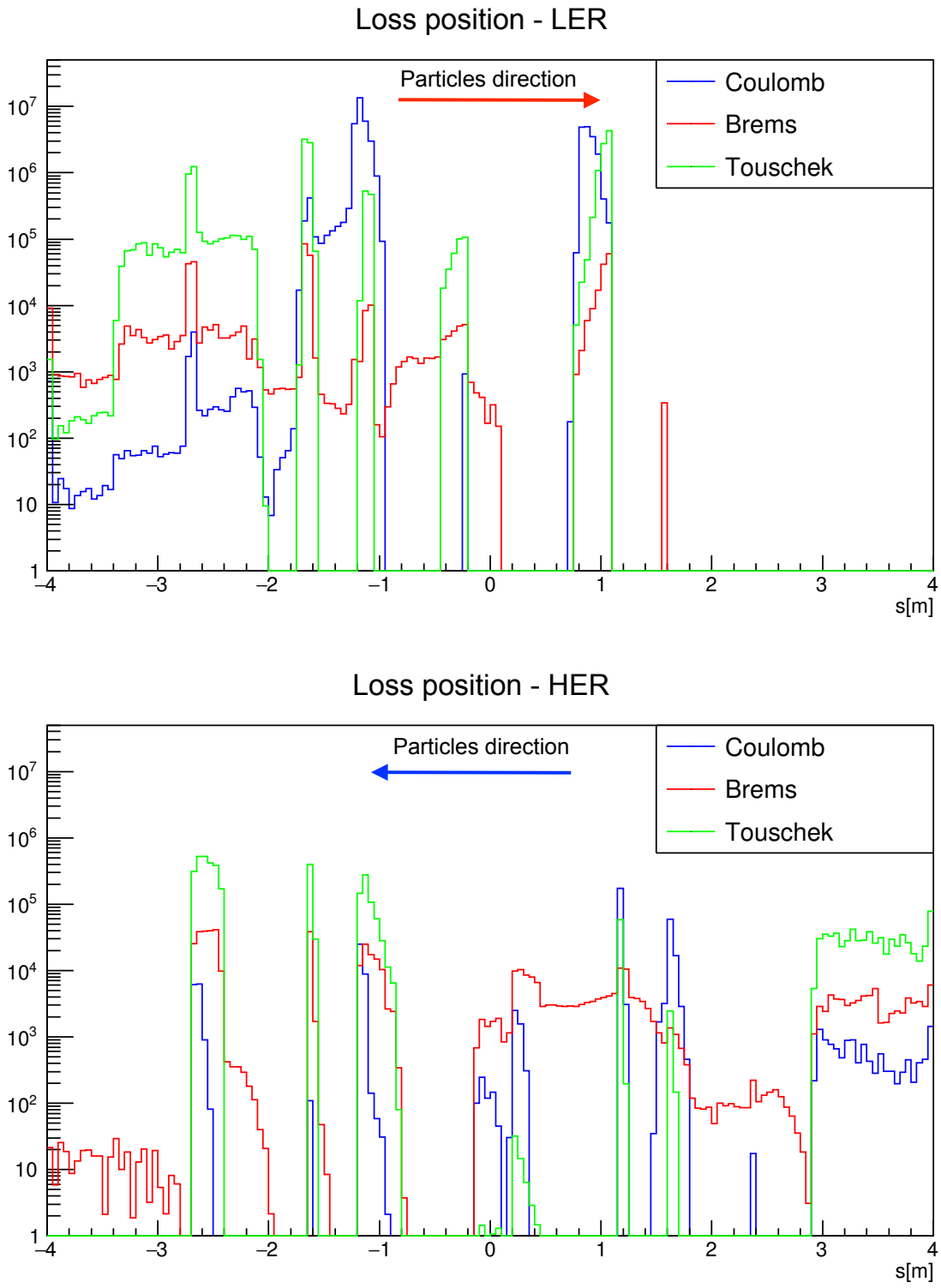

Figure 7.2: *Losses in the interaction region from SAD simulation as a function of s for the different background sources. Note that in LER plots, negative s corresponds to locations upstream the IP, while for HER is the opposite.*

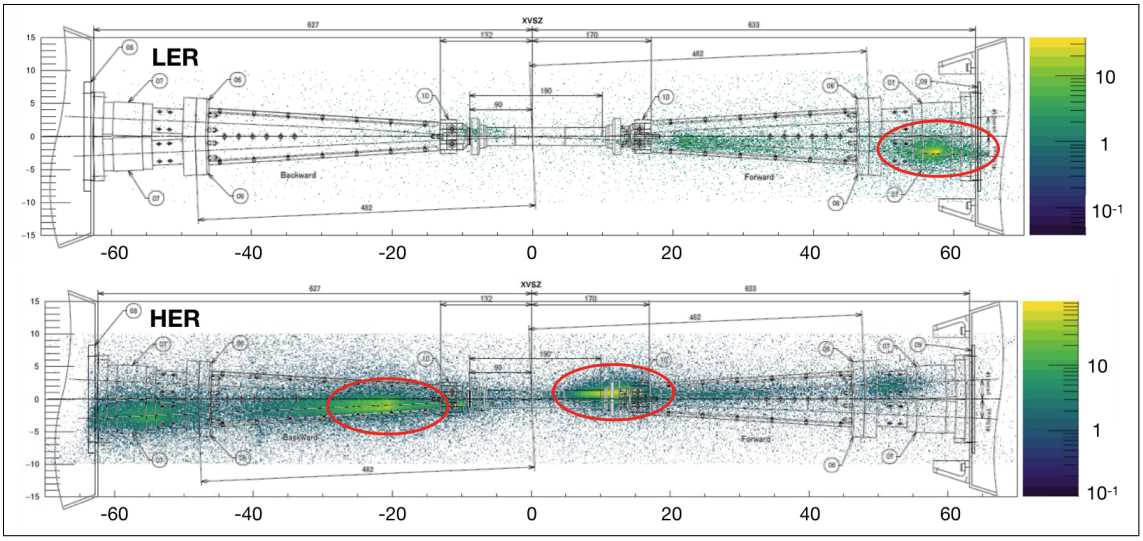

Figure 7.3: *Results of the vertices reconstruction study performed on single beam runs taken during Phase 2.*

of HER vertical collimators. Some of them were particularly effective on injection background, and it was possible, even closing them by small steps, to sensibly reduce that background, even if the effect on storage background was almost negligible. An example is shown in fig. 7.4, where it is clearly visible the effect of three vertical collimators in the injection background observed by diamond sensors. Although after the recovery from the fire accident the collimator study was started over due to different machine conditions, this result was important to consider the option of continuous injection, that was actually used from the middle of May for both rings: vertical collimators must be considered in the reduction of injection background, avoiding aborts triggered by loss monitors along the ring during injection.

When the machine recovered from the fire accident, collimators studies were performed for LER and HER after two days of extensive injection tuning, performed to decrease as much as possible injection background and allow to switch to continuous injection mode, that could have sensibly increased the integrated luminosity until the end of the run. These studies allowed a slightly different strategy for the collimator study: with the injection background significantly improved, collimators were closed in steps without injection being done between one step and the next. So only the changes in storage background were observed, with injection performed only after reaching the optimal value of a collimator, to verify that injection background has not become worse. During these collimators study, particular attention was given to those collimators that, before injection tuning, could not be closed because of injection background that was causing beam aborts from loss monitors. In this way, good storage background reduction, as well as additional injection background reduction, was achieved for both beams. The final steps in which collimators were open to the initial setting and then closed all together to the optimized setting are

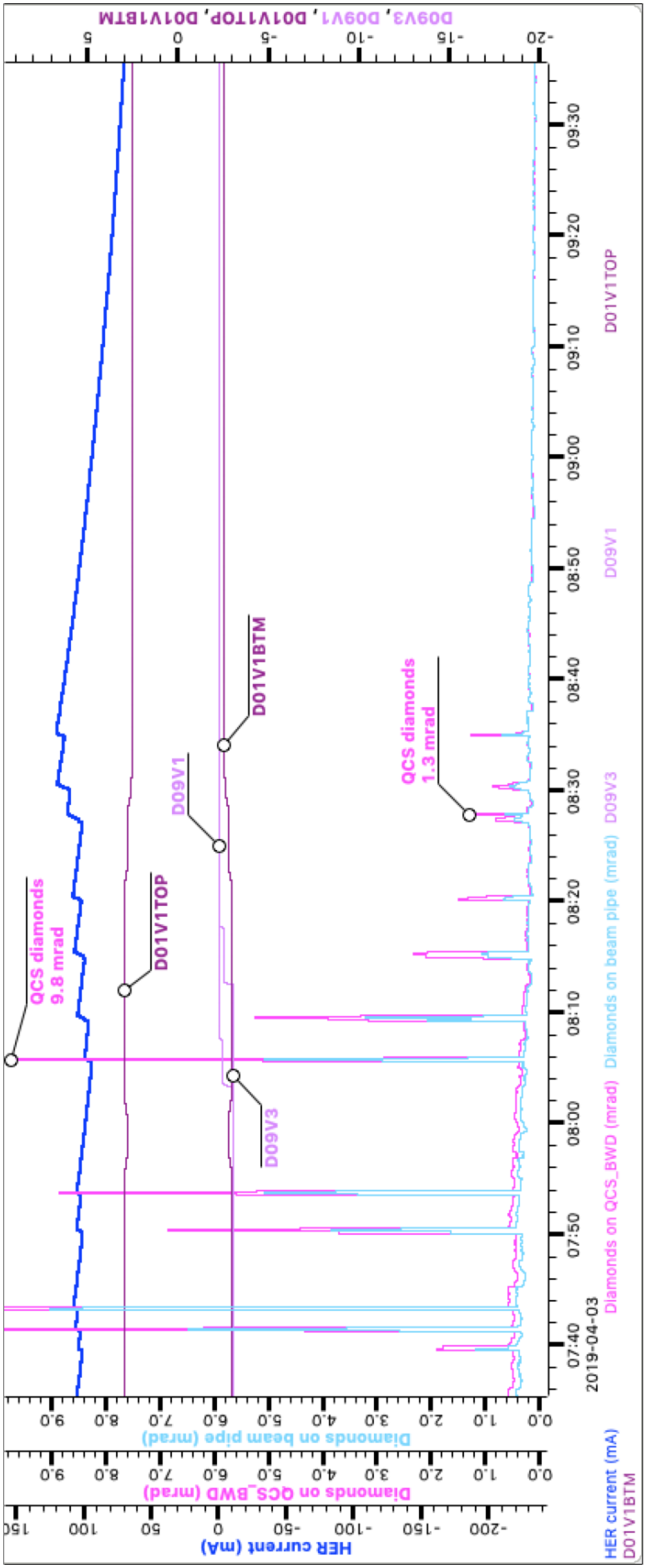

Figure 7.4: *Injection background during the first collimator study performed in Phase 3. A reduction of almost one order of magnitude can be achieved using vertical collimators.*

shown in fig. 7.5 for LER and in fig. 7.6 for HER. Storage background reduction between 15% and 20% was observed in LER, while a reduction between 40% and 60% was observed in HER. D01H4 collimator of HER has shown the same behaviour as in Phase 2, it was not possible to close it as much as planned, because background levels were increasing too much. It was still not understood if the increase was due to tip scattering or to other unknown reasons. The optimized settings achieved during operations are shown in table 7.4 for LER and in table 7.5 for HER.

For LER, probably thanks to the intensive injection studies performed before collimators optimization, the achieved setting was pretty close to the SAD optimized one for almost all collimators. For HER it was a bit different: collimators in sector D01 were set as in SAD optimization, except for D01H4 that, as in Phase 2, could not be closed due to increase in both storage and injection background. In the other sectors, collimators were far from the SAD optimized setting, but their apertures were all similar if expressed in σ, with horizontal collimators closed at $\sim 18\sigma_x$ and vertical collimators closed at $\sim 100\sigma_y$, with the only exception of D12V1 that caused severe lifetime drop when closed more than 160 σ_y.

Right after collimator studies, single beam background studies were performed, with a strategy similar to the one used in Phase 2. Also in this case beam-gas and Touschek components were evaluated taking data at different beam sizes and then fitting the re-normalized observable with a straight line, whose parameters represent the beam-gas and Touschek components. As for Phase 2, a full simulation was done with the same collimator setting used during the background studies, which is also the experimentally optimized collimator setting, in order to compare data with simulation predictions. Background rates obtained from the SAD output of this simulation are shown in table 7.6, and are compared with results of simulations of Phase 2 background studies and of optimized collimators setting for early Phase 3. The ratios between early Phase 3 and Phase 2 BG studies give an estimation of how much, according to simulation, single beam backgrounds should be reduced. Considering that optics used in the two simulations are the same, that losses are referred to the same machine parameters and that geometry updates have no effect on SAD losses, the reduction depends only on the effect of new collimators and how well they were optimized before the BG studies. These ratios are 0.24 for LER and 0.44 for HER. The result is very similar if columns 2 and 1 are compared, meaning that the optimized collimator setting found during early Phase 3 operation is as effective as the setting found in the simulated early Phase 3 collimators study.

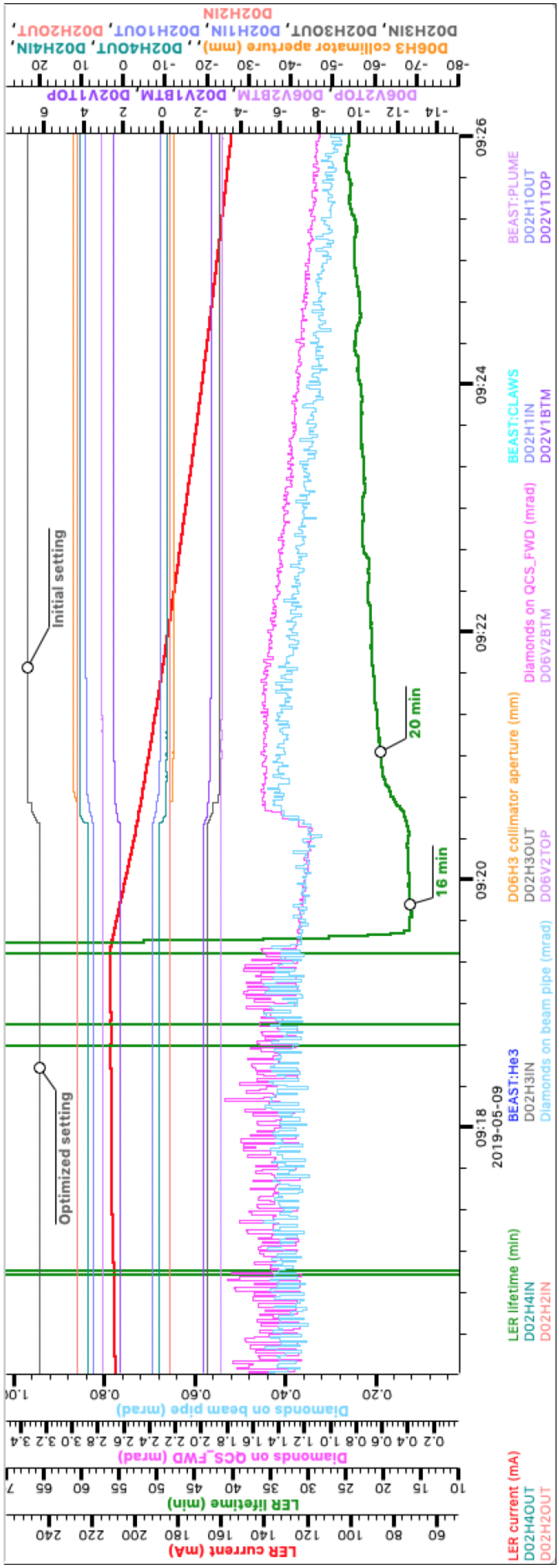

Figure 7.5: *Comparison between LER collimators settings at the beginning of the study and at the end of the study, after optimization. A background level reduction between 15% and 20% is observed with diamond detectors.*

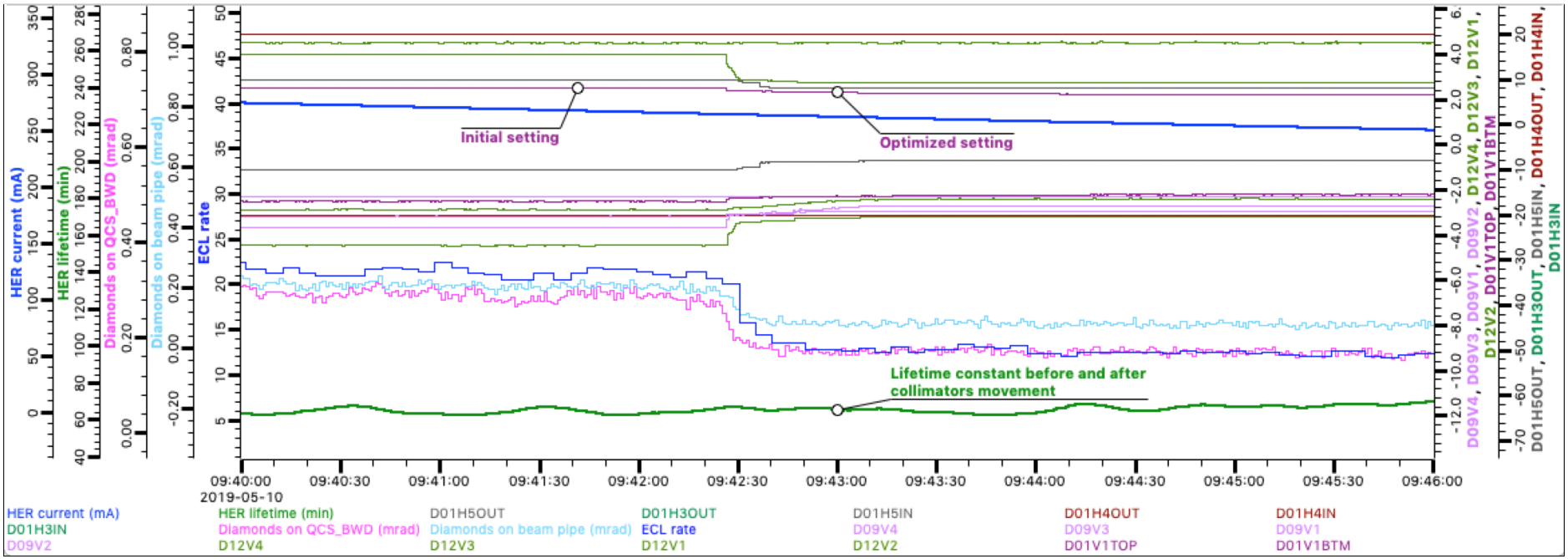

Figure 7.6: *Comparison between HER collimators settings at the beginning of the study and at the end of the study, after optimization. A background level reduction between 40% and 60% is observed with diamond and ECL detectors.*

LER	SAD Optimized setting		Experimental setting	
collimator ID	Aperture (mm)	Aperture (σ)	Aperture (mm)	Aperture (σ)
D02-V1-TOP	2.0	94	2.1	99
D02-V1-BTM	-2.0	94	-2.1	99
D02-H1-OUT	8.0	45	7.0	40
D02-H1-IN	-8.0	45	-7.0	40
D02-H2-OUT	9.0	16	11.0	19
D02-H2-IN	-9.0	16	-11.0	19
D02-H3-OUT	18.0	21	20.0	23
D02-H3-IN	-22.0	26	-20.0	23
D02-H4-OUT	8.0	24	8.5	25
D02-H4-IN	-8.0	24	-8.5	25
D03-H1-OUT	11.0	17	11.0	17
D03-H1-IN	-13.0	21	-11.0	17
D06-V2-TOP	2.0	100	3.0	149
D06-V2-BTM	-2.0	100	-3.0	149
D06-H1-OUT	10.5	18	11.0	19
D06-H1-IN	-9.0	16	-11.0	19
D06-H3-OUT	9.0	16	11.0	19
D06-H3-IN	-10.0	17	-11.0	19
QC1 - horizontal	10.5	64		
QC1 - vertical	13.5	189		

Table 7.4: *Comparison between the optimized setting found with simulation and the achieved collimators configuration.*

HER	SAD Optimized setting		Experimental setting	
collimator ID	Aperture (mm)	Aperture (σ)	Aperture (mm)	Aperture (σ)
D01-V1-TOP	2.0	76	2.4	91
D01-V1-BTM	-2.0	76	-2.4	91
D01-H3-OUT	7.0	26	7.0	26
D01-H3-IN	-7.0	26	-7.0	26
D01-H4-OUT	15.0	38	20.0	51
D01-H4-IN	-15.0	38	-20.0	51
D01-H5-OUT	8.0	27	8.0	27
D01-H5-IN	-8.0	27	-8.0	27
D12-V4-BTM	-2.0	67	-3.2	107
D12-H4-IN	-8.0	13	-12.4	20
D12-V3-TOP	2.0	75	2.7	101
D12-H3-IN	-8.0	13	-11.0	18
D12-H2-IN	-8.0	13	-11.0	18
D12-V2-BTM	-2.0	75	-2.4	90
D12-H1-IN	-8.0	13	-11.0	18
D12-V1-TOP	2.0	72	4.5	162
D09-V4-BTM	-2.0	72	-2.7	97
D09-H4-IN	-8.0	13	-11.0	18
D09-V3-BTM	-2.0	75	-3.0	86
D09-H3-IN	-8.0	13	-11.0	18
D09-H2-IN	-9.0	14	-11.5	18
D09-H1-IN	-9.0	14	-10.5	17
D09-V2-BTM	-2.0	67	-2.9	97
D09-V1-BTM	-2.0	75	-2.3	86
QC2 - horizontal	35.0	33		
QC1 - vertical	13.5	95		

Table 7.5: *Comparison between the optimized setting found with simulation and the achieved collimators configuration.*

IR losses	Phase 2 BG study		early Phase 3 optimized		early Phase 3 BG study	
	LER	HER	LER	HER	LER	HER
Coulomb (MHz)	186	1.2	28.6	0.4	44.2	4.3
Brems (MHz)	2.0	2.0	0.9	1.1	0.8	1.2
Touschek (MHz)	160	32.8	49.6	8.9	37.6	10.3
Tot (MHz)	348.0	36.0	79.1	10.4	82.6	15.8
Early Phase 3/Phase 2 ratio			0.23	0.29	0.24	0.44

Table 7.6: *Background levels and lifetimes obtained with simulation of early Phase 3 optics and the real collimators setting achieved during the experimental collimators study and used for background studies.*

7.3.1 Data analysis of early Phase 3 BG studies

New "data/MC" factors for SVD have been calculated for early Phase 3, and results are shown in table 7.7, where the factors obtained in Phase 2 have been re-scaled with the geometry update factors of table 7.1, because in the simulation of Phase 2, geometry updates were not yet implemented.

Comparing the "data/MC" factors between early Phase 3 and Phase 2 shown in the table, they are more or less the same for LER and lower for HER beam-gas, but they are much higher for HER Touschek. The explanation has not been fully understood, although there are some hypotheses that can at least partially explain the facts. One possibility is that collimators in the simulation are perfect absorbers: a particle, during tracking in SAD, can be at a radius smaller than the collimator aperture, and in this case it continues travelling toward the next lattice slice without any effect, or it can be at a radius larger than the collimator aperture, and in this case the tracking is stopped and the particles is considered lost. No secondary particles are generated, and no tip scattering is considered. During operations in Phase 2 and early Phase 3 there was evidence of tip scattering, that in some cases prevented to close more some collimators. If we add to this limitation the big number of collimators used in the HER, we can probably assume that the HER background may be underestimated. Another effect has been noted running simulations for new optics to be used from the Fall 2019 run, that will be briefly discussed in chapter 8: with new optics there is a big increase in HER Touschek background, higher than the increase in LER, so another possibility is that the underestimation of HER Touschek component comes from the simulated early Phase 3 optics, for reasons to be investigated. This will be clear once background studies will be performed with new optics and results will be compared with simulations.

Other Belle II sub-detectors did analyses on background studies. Those sub-

	early Phase 3 occupancy (%)		early Phase 3	Phase 2
	data	MC	"data/MC"	"data/MC"
HER beam-gas	0.0256	0.0016	16	55
HER Touschek	0.0256	1.6×10^{-5}	1600	205
LER beam-gas	0.1440	0.012	12	9.3
LER Touschek	0.0242	0.022	1.1	1.5

Table 7.7: *Estimation of "data/MC" factors using SVD occupancy for layer 3 sensors. In the last column, the scaling factors obtained in Phase 2, scaled for the geometry update already shown in table 7.1, are reported for a comparison.*

	Phase 2		Early Phase 3	
	LER	HER	LER	HER
B [10^4%/(mA·Pa)]	1.74	0.72	0.42	0.24
T [%·μm/(mA)^2]	0.075	0.023	0.167	0.009

Table 7.8: *B and T coefficients evaluated for SVD in Phase 2.*

detectors that compared Phase 2 and early Phase 3 data agree that background levels decreased in early Phase 3. The CDC in particular saw much lower background than in Phase 2. PXD and TOP groups also agree on the LER beam-gas component being the dominant one.

To estimate if and how much backgrounds have decreased in early Phase 3 with respect to Phase 2, the first step was to re-calculate the Touschek and beam-gas components from the re-normalized observables. Plots used for SVD are shown in fig. 7.7 for LER and HER, referring to background studies performed for LER and HER on May 14th and May 12th respectively. In these plots, two data samples are shown, "fill pattern" and "beam size", which are referred to two different ways of changing the Touschek background component. As shown in equation (6.7), the Touschek component of the observable depends on the number of bunches n_b and on the vertical beam size σ_y, so changing one of these two parameter changes the Touschek component of the single beam background. In early Phase 3 background studies, the Touschek component has been changed in two different ways, therefore two data samples were obtained and are both shown in the plots of fig. 7.7.

New B and T coefficients have been extracted also from early Phase 3 data and are shown in table 7.8, together with the coefficients obtained in Phase 2. To compare the background components between Phase 2 and early Phase 3, the observable (in this case SVD occupancy for Layer 3 sensors) must be calculated

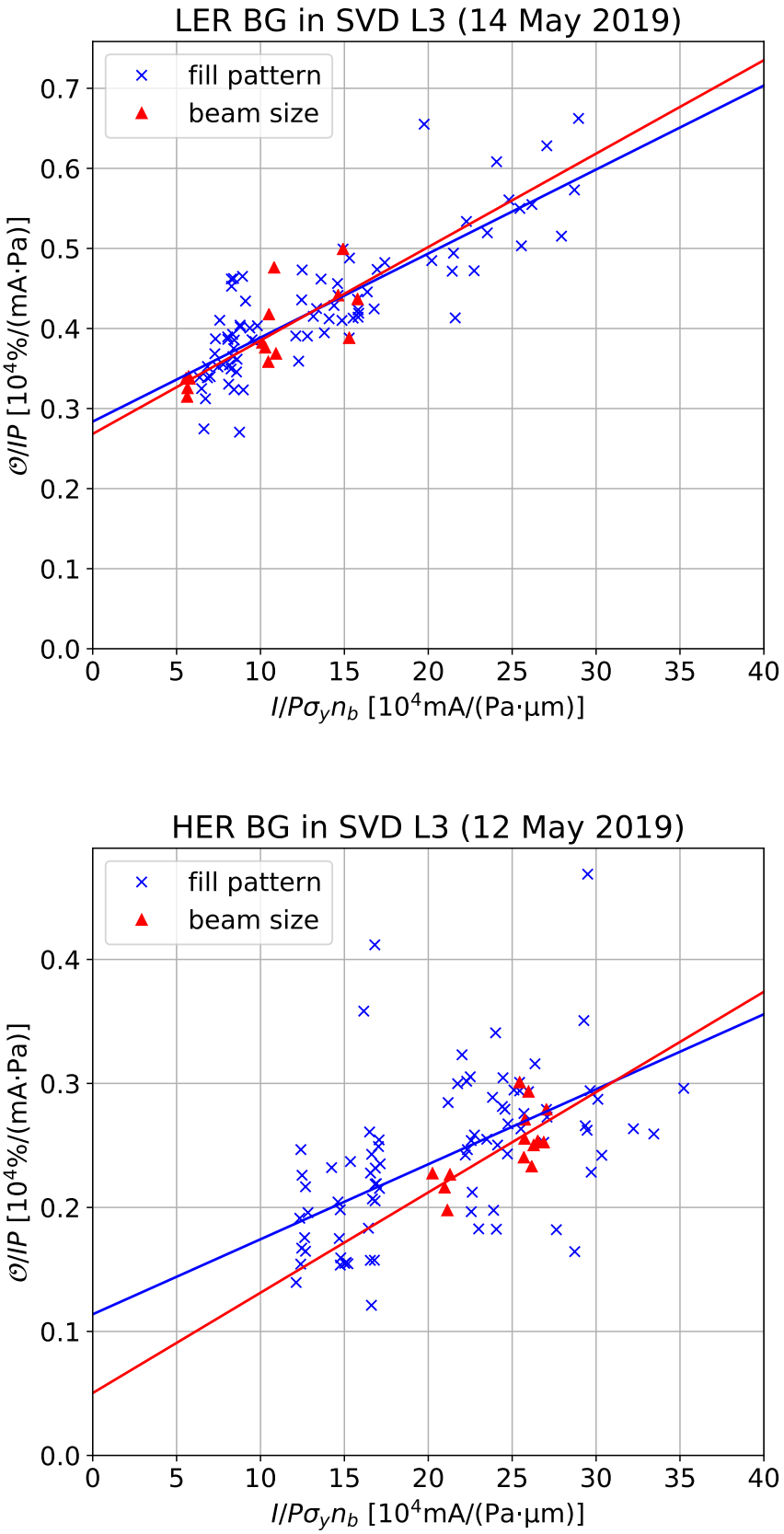

Figure 7.7: *Early Phase 3 background studies results for SVD. LER and HER data and fits are shown.*

BG source	Phase 2 occupancy (%)	Early Phase 3 occupancy (%)	Early Phase 3/Phase 2 ratio
LER beam-gas	0.5	0.14	0.28
LER Touschek	0.09	0.02	0.22
LER tot.	0.59	0.16	**0.27**
HER beam-gas	0.06	0.02	0.33
HER Touschek	0.05	0.02	0.40
HER tot.	0.11	0.04	**0.36**

Table 7.9: *SVD Layer 3 occupancy obtained with B and T coefficients calculated for Phase 2 and early Phase 3.*

at the same machine parameters. In this case, the following parameters have been used:

- LER: I = 350 mA; $\sigma_y = 130\mu$m, $P_{beam} = 9.55 \times 10^{-8}$ Pa, $n_b = 789$
- HER: I = 320 mA; $\sigma_y = 60\mu$m, $P_{beam} = 2.6 \times 10^{-8}$ Pa, $n_b = 789$

With these parameters, occupancy values for SVD Layer 3 sensors were calculated and are shown in table 7.9. First and second columns show the occupancies for Phase 2 and early Phase 3 respectively, while the third column shows the difference between second and first column. Comparing the "LER tot." and "HER tot." ratios with the expected reductions obtained in table 7.6 it can be seen that the background reduction achieved in early Phase 3 is consistent with the expectations coming from the collimator study done for early Phase 3.

7.4 Background extrapolation to Phase 3

New "data/MC" factors obtained for early Phase 3 and shown in table 7.7 can be used for a new extrapolation of the observables at SuperKEKB design parameters, exactly as it was done at the end of section 6.3. To do so, an additional step is needed, because the simulation used to calculate the "data/MC" ratios in early Phase 3 contains the geometry updates, that are not considered in the old MC used for the extrapolation at the end of Phase 2. Thus the new extrapolated value for the SVD Layer 3 occupancy would be given by:

$$Occ.(\%) = Phase3\_MC\_occ.(\%) \times G4\_factors \times data/MC \tag{7.1}$$

where $G4\_factors$ are accounting for the updated geometry implemented in early Phase 3 simulations, and $data/MC$ is the early Phase 3 "data/MC" of table 7.7. New predictions for the occupancies of SVD Layer 3 sensors are shown in table 7.10.

Source	Phase 3 MC occupancy (%)	G4_factors	Early Phase 3 "data/MC"	Phase 3 occupancy prediction (%)
HER beam-gas	0.0036	11	16	0.63
HER Touschek	0.0003	7.8	1600	4.1
HER tot.	0.0039			**4.7**
LER beam-gas	0.066	4.2	12	3.3
LER Touschek	0.11	3.0	1.1	0.36
LER tot.	0.176			**3.7**

Table 7.10

With improved "data/MC" ratios, the predictions are slightly better than at the end of Phase 2, but still it looks clear that the background conditions must be anyway improved while approaching final currents and optics. This way of extrapolating the background to design Phase 3 optics is not the only possible one, but so far has been considered the most reliable one.

Another way of extrapolating the background conditions to final Phase 3 parameters would be to simply take the observable quantities and scale them to the final machine parameters. However, this technique does not take into account two factors:

- The number of collimators installed is not the final one, so the extrapolation would overestimate the background levels, and then it's not easy to quantify how much backgrounds would be overestimated;
- Reducing the β_y^* at the IP, the vertical beta function would increase near QCS components, increasing the beam size in these locations, and therefore increasing the beam-gas component of the backgrounds. But it's not trivial to consider this effect in the scaling towards final machine parameters.

What has been proved between Phase 2 and early Phase 3 so far is the effectiveness of additional collimators installed between the two runs. There are still some locations where collimators could be installed, but budget limitations and the necessary time to produce and install collimators limit the number of new collimators that can be installed in the next years. So it is essential to find the best position where new collimators should be installed, to maximise the background reduction in the next runs. One way to find the best position for collimators is the simulation with the next optics that will be used, and then with the final Phase 3 optics, adding one or more collimators at a time and see which one is more effective for background reduction. This would give the machine group indications on where next collimators

should be installed, and how many of them should be installed. These studies for the optics to be used in the Fall run of 2019 and for final Phase 3 parameters already started, and the first results are presented in the next chapter.

Chapter 8

Final Phase 3 collimator studies

8.1 Collimator study on simulation for Fall 2019 run

The SAD background simulation can be useful to predict the effectiveness of additional collimators, suggesting the best location to install them. In SuperKEKB there are some locations along the rings where collimators could be installed, and these locations are already marked in the simulation with a collimator element. When running simulations, collimators can be easily added in these locations. In 2020, during the short Winter shutdown, the installation of one vertical collimator is planned, but there are two possible locations to install it, so the simulation was used to study the effect of an additional collimator in both locations. The optics used for these simulations is the one used at the very end of the early Phase 3 run, that should be the one to be used at the beginning of the Fall 2019 run. Parameters of the optics and machine parameters used for this study are summarized in table 8.1.

The first step of the study is to find the optimized collimators setting with the actual set of collimators installed, with the same strategy described in section 5.4. The simulation with the optimized collimators setting will be the baseline for the background levels. The optimal aperture of the collimators to be installed is found with all other collimators open, closing them individually in steps. Finally, each additional collimator is added to the optimized collimators setting previously found and is set to its optimal aperture. A simulation is run for each additional collimator and results on background levels are compared to the baseline. For this study there are two possible locations where one vertical collimator could be installed, D06V1 and D03V1. Once the baseline was found optimizing collimators used in early Phase 3, the additional collimators were also optimized and individually added to the baseline set of collimators. Results of background levels obtained for the three

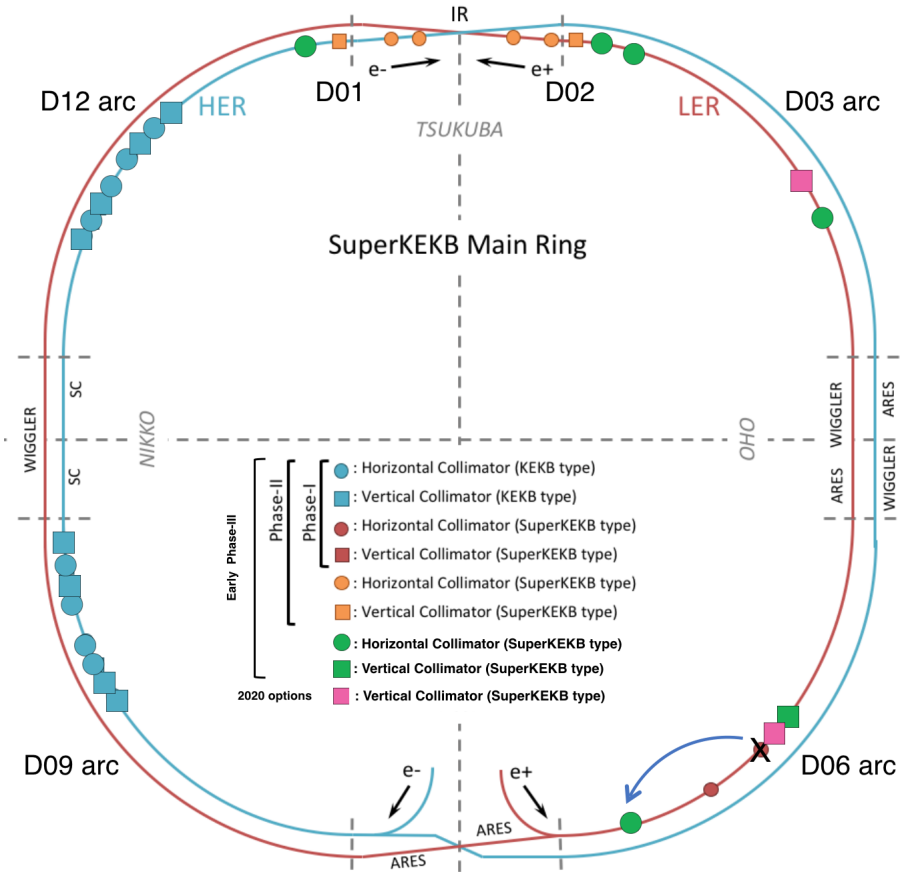

Figure 8.1: *Map of collimators with possible collimators to be installed in 2020 in LER.*

Parameter	Units	LER	HER
β_x^*	mm	80	80
β_y^*	mm	2	2
ε_x	nm	1.7	4.6
ε_y	pm	17	46
n_b		1576 (*)	
I	mA	1200	1000
P	nTorr	1	

Table 8.1: *Parameters foreseen for simulations of Fall 2019 optics.*
(*) At the beginning of the Fall 2019 run it was decided to change the fill pattern adding a second abort gap, so the machine actually runs with 1489 bunches.

IR losses	Early Phase 3 optimized	Phase 3 BG study	2x80 optimized	2x80 + D06V1	2x80 + D03V1
LER		2019/05/14			
Coulomb (MHz)	28.6	44.2	124	52.6	123
Brems (MHz)	0.9	0.8	1.1	1.1	1.1
Touschek (MHz)	49.6	37.6	52.4	33.9	33.9
Tot (MHz)	79.1	82.6	177.5	87.6	158
Lifetime (s)	815	831	1419	1363	1419
HER		2019/05/12			
Coulomb (MHz)	0.4	4.3	3.8		
Brems (MHz)	1.1	1.2	0.9		
Touschek (MHz)	8.9	10.3	52.7		
Tot (MHz)	10.4	15.8	57.4		
Lifetime (s)	3564	5085	3533		

Table 8.2: *Results of the collimator study for 2 mm x 80 mm optics. LER results include additional collimators that could be installed during winter 2019 short shutdown.*

different simulations are shown in table 8.2. The optimized collimators apertures are shown in table 8.3 for LER and in table 8.4 for HER.

From table 8.2 a significative reduction of total background levels by a factor 2 with respect to the baseline can be observed in the simulation where the D06V1 collimator is added. D03V1 collimator is not as effective as D06V1, the reason being the β_y value at the collimator location, which is higher for D06V1: at the optimal aperture of ± 3 mm, D06V1 has an aperture of 84 σ, while D03V1, even if closed down to the limit of ± 2 mm, has an aperture of 106 σ. This consideration, verified with simulation, makes collimator D06V1 the best choice for the next installation.

8.2 Collimator study on final Phase 3 parameters

A similar study as the one presented in the previous section can be extended to the final SuperKEKB optics and machine parameters, considering all other possible locations where collimators can be installed to build a "priority list" of collimators to be installed. This would give an indication to the machine group on which collimator can be installed before the others. For the HER, the way of doing such a study is the same as it was done in the previous section, because there are only two additional collimators that could be installed, so just which one should be installed first has to be decided. For the LER it's different, because potentially there are six additional collimators, so the procedure should be used to decide the installation

LER	SAD Optimised setting	
collimator ID	Aperture (mm)	Aperture (σ)
D02-V1-TOP	2.0	106
D02-V1-BTM	-2.0	106
D02-H1-OUT	9.0	39
D02-H1-IN	-8.0	35
D02-H2-OUT	13.0	23
D02-H2-IN	-13.0	23
D02-H3-OUT	20.0	26
D02-H3-IN	-19.0	25
D02-H4-OUT	9.0	25
D02-H4-IN	-12.0	33
D03-V1-TOP (**)	2.0	106
D03-V1-BTM (**)	-2.0	106
D03-H1-OUT	14.0	22
D03-H1-IN	-20.0	32
D06-V1-TOP (*)	3.0	84
D06-V1-BTM (*)	-3.0	84
D06-V2-TOP	2.0	100
D06-V2-BTM	-2.0	100
D06-H1-OUT	13.0	23
D06-H1-IN	-11.0	19
D06-H3-OUT	12.0	21
D06-H3-IN	-15.0	16
QC1 - horizontal	10.5	41
QC1 - vertical	13.5	155

Table 8.3: *Optimized LER collimators setting for 2 mm x 80 mm optics. Collimators marked with (*) and (**) are the two options that were studied in simulation.*

HER	SAD Optimised setting	
collimator ID	Aperture (mm)	Aperture (σ)
D01-V1-TOP	2.4	73
D01-V1-BTM	-2.4	73
D01-H3-OUT	7.0	25
D01-H3-IN	-7.0	25
D01-H4-OUT	15.0	42
D01-H4-IN	-15.0	42
D01-H5-OUT	8.0	24
D01-H5-IN	-8.0	24
D12-V4-BTM	-2.5	84
D12-H4-IN	-8.0	13
D12-V3-TOP	2.5	94
D12-H3-IN	-8.0	13
D12-H2-IN	-8.0	13
D12-V2-BTM	-2.5	94
D12-H1-IN	-8.0	13
D12-V1-TOP	2.5	90
D09-V4-BTM	-2.5	90
D09-H4-IN	-8.5	14
D09-V3-BTM	-2.5	90
D09-H3-IN	-8.5	14
D09-H2-IN	-9.0	14
D09-H1-IN	-9.0	14
D09-V2-BTM	-2.5	84
D09-V1-BTM	-2.5	94
QC2 - horizontal	35.0	29
QC1 - vertical	13.5	78

Table 8.4: *Optimized HER collimators setting for 2 mm x 80 mm optics.*

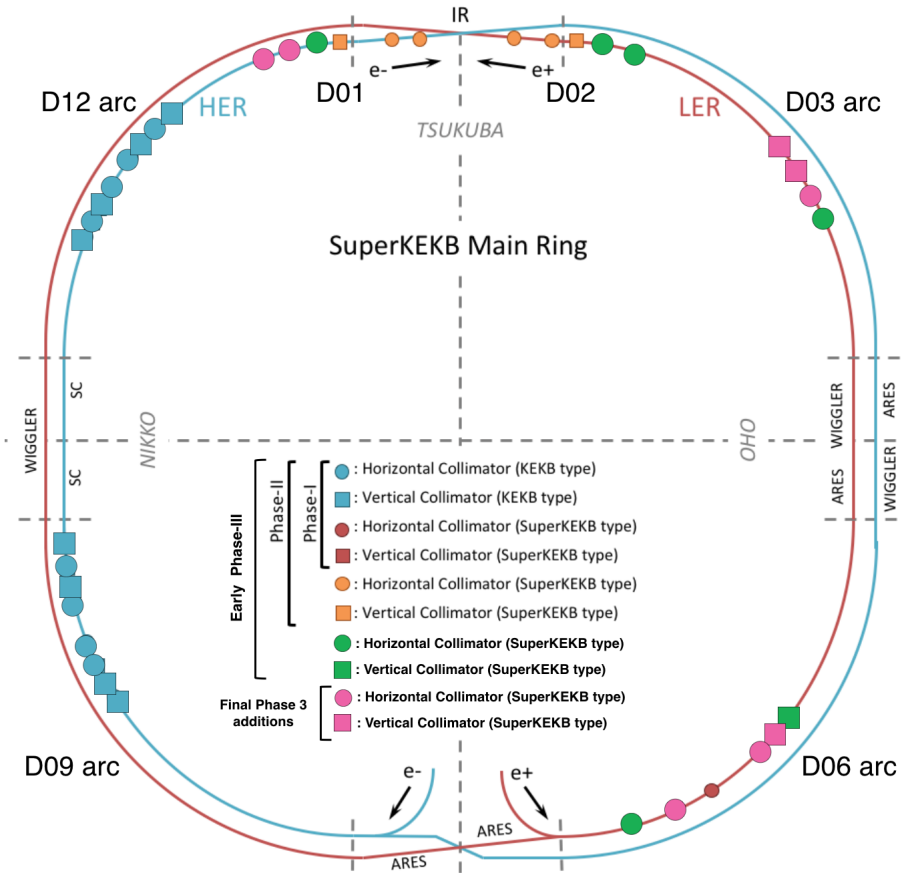

Figure 8.2: *Final map of collimators that could be installed in Phase 3.*

order of collimators. A map with all additional locations where collimators can be installed is shown in fig. 8.2. With the high levels of background expected at final Phase 3 optics and parameters, the strategies used so far for collimator optimization and to decide which additional collimator should be installed must be improved, because the effect of other collimators in the lattice cannot be neglected anymore. A better strategy for collimator optimization will be proposed in section 8.2.1, while for collimators to be installed, a possible new strategy would be:

1. Make the collimator study for final Phase 3 machine optics and parameters, with collimators currently installed, and find the optimal setting that minimizes losses in the interaction region. This configuration is considered as the baseline.

2. With the optimized setting, add individually each additional collimator, optimize its aperture and see how losses are reduced with respect to the baseline, keeping losses on the collimator below 100 GHz, which is considered as the safety limit of the collimator to avoid damage.

3. Decide which collimator should be installed first, then add this collimator to the existing collimators set to update the baseline simulation, and then repeat point 2 with remaining collimators to be added.

4. Iterate the procedure until the choice for the second last collimator to be installed is taken.

Steps 2 and 3 require a lot of simulation time, it's an iterative procedure that, every time a collimator is added to previous ones, requires an update of collimators configuration. For these reasons, the study on LER additional collimators has been divided into a preliminary step in which, using the actual strategy for apertures optimization, all collimators are evaluated at the first iteration of the described procedure, to have an idea on the installation order of collimators to be added; then a more systematical study will be conducted after adding the first collimator, updating the baseline with the added collimator and then proceeding with steps 2 and 3 until the decision on the second last collimator to be installed can be taken. Given the results presented in the last section, it can be assumed that the first collimator that will be installed in LER will be D06V1, so this collimator has been included already in the baseline for this study. The main parameters used for the final optics simulation of Phase 3 are summarised in table 8.5. The results of the preliminary step are reported in this work, while the second step is currently ongoing and will be completed in the next months.

In table 8.6 the results for the preliminary step of the study are reported for LER and HER. HER is a simple case with only two additional collimators, and

Parameter	Units	LER	HER
β_x^*	mm	32	25
β_y^*	mm	0.27	0.30
ε_x	nm	3.2	4.6
ε_y	pm	8.64	12.9
n_b		2500	
I	mA	3600	2600
P	nTorr	1	

Table 8.5: *Main SuperKEKB design parameters for SAD simulation.*

from the results of the study it seems that the best choice would be to install first collimator D01H1 and then D01H2, because the first one minimizes the losses in the interaction region more than the other one. Looking at the absolute values of the losses in the interaction region for LER and HER, it is clear that LER losses are much higher, so it looks like priority has to be given to LER collimators. However, the background studies done during operations and the very high "data/MC" ratios obtained so far and reported in chapter 7 suggest that HER background may not be so much lower than LER one, so the possibility of installing a horizontal collimator in HER must be taken into account, considering background levels that will be evaluated in the next runs. For LER, after including D06V1 collimator, the other two vertical collimator have a small impact only on beam-gas Coulomb losses, while between horizontal collimators the most effective seems to be D03H2, that can reduce Touschek losses, but losses on the collimator are already exceeding a bit the safety limit. The other two horizontal collimators cannot help in reducing losses at this stage. In general it seems that adding collimators at their optimal aperture is not improving background levels that much. This means that to further reduce background in the IR, collimators should be closed more than their optimal point, at the expenses of lifetime. This would also increase losses on each collimator, with the risk of exceeding the safety limit of 100 GHz. Losses on collimators thus become an additional parameter to be considered in the optimization process. Finding the optimal collimator setting with the procedure used so far would be ineffective, and improvements must be made in the optimization strategy. Optimal collimators apertures obtained in the preliminary step of this study are reported in table 8.7 for LER and in table 8.8 for HER.

8.2.1 Possible collimator optimization strategy for Phase 3

Absolute values of IR losses in LER reported in table 8.6 are pretty high, beyond the limit of 100 MHz. This is not surprising, since collimators are not all together

	IR losses (MHz)			Lifetimes (s)			Collimator losses
	C	B	T	C	B	T	(GHz)
LER							
baseline	636	2.6	675	1740	171008	388	
D03H2	621	2.6	430	1740	171008	388	103
D03V1	609	2.6	675	1740	171008	388	2.5
D03V2	574	2.6	675	1740	171008	388	6
D06H2	636	2.6	675	1741	171137	388	4
D06H4	635	2.6	675	1741	171137	388	47
HER							
baseline	21	1.9	14	2717	152169	808	
D01H1	18	1.8	0.0	2717	152169	808	10
D01H2	11	1.9	14	2717	152169	808	20

Table 8.6: *IR losses and lifetimes for simulations with additional collimators for final Phase 3. D06V1 is already included in the baseline configuration.*

included in the simulation. However, there are existing Phase 3 simulations, with all collimators included, in which IR losses are still too high, around 300 MHz. One way of solving the problem would be to close collimators even beyond their optimal aperture, at the expenses of beam lifetime, but LER lifetime is already very small at design optics, of the order of a few minutes, so reducing it even more would be impractical for machine operation. As anticipated in section 5.4 and in the last section, the collimators optimization procedure used so far is not enough for simulations with final Phase 3 optics and parameters, where background levels are very high. Improvements to the procedure should be found in order to find a better background reduction without affecting beam lifetime. A possible way to find the optimal collimators setting could be:

1. Start from the fully open configuration and optimize the first collimator, which would be the most upstream one with respect to the IP.

2. Include the optimized collimator in a new baseline that is used to optimize the second collimator.

3. Repeat the procedure until the last collimator.

4. Make a full simulation with the optimized collimators setting to evaluate IR losses. If the result is not enough, start over using as a starting point the optimized collimator setting.

In this way, collimators are not considered independently one from each other and the effect of the upstream collimators will allow a better optimization of the downstream

LER	SAD Optimised setting	
collimator ID	Aperture (mm)	Aperture (σ)
D02-V1-TOP	2.4	77
D02-V1-BTM	-2.3	74
D02-H1-OUT	8.5	14
D02-H1-IN	-8.5	14
D02-H2-OUT	11.5	17
D02-H2-IN	-11.5	17
D02-H3-OUT	15.0	19
D02-H3-IN	-14.5	18
D02-H4-OUT	8.0	16
D02-H4-IN	-8.5	17
D03-H1-OUT	13.5	19
D03-H1-IN	-14.0	20
D03-H2-OUT (*)	12.0	16
D03-H2-IN (*)	-12.0	16
D03-V1-TOP (*)	2.0	165
D03-V1-BTM (*)	-2.0	165
D03-V2-TOP (*)	2.0	165
D03-V2-BTM (*)	-2.0	165
D06-V1-TOP (*)	2.5	109
D06-V1-BTM (*)	-2.5	109
D06-V2-TOP	2.0	155
D06-V2-BTM	-2.0	155
D06-H1-OUT	12.5	20
D06-H1-IN	-11.5	18
D06-H2-OUT (*)	10.0	16
D06-H2-IN (*)	-10.0	16
D06-H3-OUT	10.0	16
D06-H3-IN	-10.0	16
D06-H4-OUT (*)	10.0	16
D06-H4-IN (*)	-10.0	16
QC1 - horizontal	10.5	21
QC1 - vertical	13.5	241

Table 8.7: *Optimized LER collimators setting for SuperKEKB design optics and parameters.*
Marked collimators are the ones yet to be installed.

HER	SAD Optimised setting	
collimator ID	Aperture (mm)	Aperture (σ)
D01-V1-TOP	2.3	52
D01-V1-BTM	-2.3	52
D01-H1-OUT (*)	7.0	12
D01-H1-IN (*)	-7.0	12
D01-H2-OUT (*)	8.0	10
D01-H2-IN (*)	-8.0	10
D01-H3-OUT	7.0	20
D01-H3-IN	-7.0	20
D01-H4-OUT	7.0	28
D01-H4-IN	-7.0	28
D01-H5-OUT	8.0	14
D01-H5-IN	-8.0	14
D12-V4-BTM	-2.0	126
D12-H4-IN	-7.5	12
D12-V3-TOP	2.0	142
D12-H3-IN	-7.5	12
D12-H2-IN	-7.5	12
D12-V2-BTM	-2.0	142
D12-H1-IN	-7.5	12
D12-V1-TOP	2.0	136
D09-V4-BTM	-2.0	136
D09-H4-IN	-7.5	12
D09-V3-BTM	-2.0	142
D09-H3-IN	-7.5	12
D09-H2-IN	-7.5	12
D09-H1-IN	-7.5	12
D09-V2-BTM	-2.0	126
D09-V1-BTM	-2.0	142
QC2 - horizontal	35.0	16
QC1 - vertical	13.5	30

Table 8.8: *Optimized HER collimators setting for SuperKEKB design optics and parameters.*
Marked collimators are the ones yet to be installed.

ones. In this process, the operator should keep in mind that losses on collimators have the safety limit of 100 GHz, so losses should be distributed among collimators that have the same betatron phase to avoid that losses on one of them go beyond the safety limit. In addition, also TMCI limits discussed in section 3.4.2 (apertures of 8 mm for horizontal collimators and 2 mm for vertical ones in LER, 7 mm and 2 mm for horizontal and vertical collimators respectively for HER) must be considered: even if losses on a collimator are not particularly high, if the collimator aperture is at the TMCI limit, it cannot be closed more. This new optimization procedure is slower than the one described in section 5.4 because collimators must be optimized in series, and requires also a higher number of simulations, but it can give better results. The effectiveness of this procedure should be studied soon, in order to have the results in time, before final Phase 3 optics will be used.

Another possible improvement in the optimization procedure could be obtained re-thinking the SAD simulation: instead of running a simulation for each collimator setting, it would be more efficient to run the simulation once, tracking particles along each ring, and then optimize collimators aperture with a specific code that uses the results from the SAD simulation to find the optimal collimators setting. This possibility has some technical difficulties that must be overcome before being used. Such a possibility is currently under study and evaluation by the background group.

Conclusions

Since the start of SuperKEKB operations, simulations have been used to perform studies on collimators and to simulate the same conditions used for background studies.

First simulated collimators studies were done at the beginning of Phase 2 to get an optimal setting that was used as a reference during operation, when collimators studies were performed on the real system and a reduction of background was successfully achieved for both rings. Using the optimal setting obtained during operation, simulations were done to be compared with data. From the comparison, the background group found that "data/MC" ratios for Phase 2 were too high, suggesting that improvements were needed on the simulation to make it more reliable. Some modifications were done on the GEANT4 simulation and on the output of SAD simulation, and the comparison between the updated and old geometry showed that the modifications improved the reliability of the simulation, also for early Phase 3, where for LER and HER beam-gas "data/MC" ratios were acceptable, making the extrapolation of background levels to final Phase 3 optics more reliable. However HER Touschek "data/MC" ratio increased substantially and it's three orders of magnitude far from unity, meaning that there is still something not well under control in the simulation, maybe due to those processes that cannot be implemented in the simulation, such as tip scattering or showers produced in collimators heads, or due to other reasons that should be further investigated. Moreover, first simulation studies done for early Phase 3 showed a potential background reduction of $\approx$70-75% for both beams, which was a crucial information for the installation of the full VerteX Detector in November 2018.

Despite the high "data/MC" ratios that keep the simulation far from a reliable representation of the real machine, the reduction of background levels between Phase 2 and early Phase 3 simulations seems in agreement with the reduction observed in data, at least considering the overall losses in the interaction region for each beam. This result must be confirmed with further studies at different optics, starting already with the Fall 2019 run, when the optics used for the collimator study described in section 8.1 will be used.

The studies performed on collimators between Phase 2 and early Phase 3, on

simulations and on data, demonstrated that collimators can be very effective against machine induced background. More collimators will be installed in the next years of operation, but not all together and a priority list must be prepared to install first the most effective collimators. A first study on the next optics that will be used in Fall 2019 suggests that the best position for the next collimator installation in LER, to be done during 2020 Winter shutdown, is D06V1. For final Phase 3 optics, a more systematic study should be conducted not only to understand which collimators are more effective, but also to optimize in the best possible way collimators apertures, distributing losses between collimators to avoid damages on them due to high energy deposit on collimators heads, and avoiding TMCI aperture limits. First results on a preliminary step of the study have been presented, while the full study is in progress and should give results before final Phase 3 optics will be used.

Bibliography

[1] Bevan, A.J., Golob, B., Mannel, T. et al., *The Physics of the B Factories*, Eur. Phys. J. C (2014) 74: 3026. https://doi.org/10.1140/epjc/s10052-014-3026-9

[2] T. KEK, *KEKB B-Factory Design Report*, KEK-REPORT-95-7, August 1995.

[3] A. Abashian et al., Belle Collaboration, *The Belle Detector*, Nuclear Instruments and Methods in Physics Research A 479 (2002) 117-232

[4] T. Abe et al., Belle II Collaboration, *Belle II Technical Design Report*, ArXiv e-prints (2010) , arXiv:1011.0352.

[5] *http://www-superkekb.kek.jp/documents.html*

[6] Y. Ohnishi et al., *Accelerator Design at SuperKEKB*, Prog. Theor. Exp. Phys. 2013, 2013, 03A011, DOI:10.1093/ptep/pts083

[7] K. Akai, K. Furukawa, H. Koiso *SuperKEKB Collider*, Nuclear Instruments and Methods in Physics Research Section A, vol. 479, pp. 188-199, 2018, DOI:10.1016/j.nima.2018.08.017

[8] P. Raimondi, D. N. Shatilov, M. Zobov, *Beam-Beam Issues for Colliding Schemes with Large Piwinski Angle and Crabbed Waist*, LNF-07/003 (IR), arXiv:physics/0702033

[9] *SuperB: A High-Luminosity Asymmetric e^+ e^- Super Flavor Factory. Conceptual Design Report*, INFN/AE-07/2, SLAC-R-856, LAL 07-15, March 2007, https://arxiv.org/pdf/0709.0451.pdf

[10] L. Vitale, *The Monitoring System of the Belle II Vertex Detector*, PoS Vertex2016, 2017, DOI:10.22323/1.287.0051

[11] A. W. Chao, K. H. Mess, M. Tigner, F. Zimmermann, *Handbook of Accelerator Physics and Engineering*, World Scientific, 2012

[12] R. Sugahara, T. Kawamoto, M. Masuzawa, *Sextupole magnets with variable tilting angle for SuperKEKB*, IEEE Trans. Applied Superconductivity 26 (4), 2016, DOI:10.1109/TASC.2016.2541697

[13] T. Oki, N. Tokuda, T. Adachi, N. Ohuchi, S. Nakamura, *Full scale prototype power supply for SuperKEKB final focus superconducting magnets*, IEEE Trans. Applied Superconductivity 26 (4), 2016, 0601404, DOI:10.1109/TASC.2016.2523058

[14] G. Rumolo, F. Zimmermann, *Theory and Simulation of the Electron Cloud Instability*, SL/AP CERN, Geneva, Switzerland, 2001

[15] F. Zimmermann, *The electron cloud instability: Summary of measurements and understanding*, PAC 2001. Proceedings of the 2001, 666 - 670 vol.1, DOI:10.1109/PAC.2001.987600

[16] Y. Suetsugu, M. Shirai, M. Ohtsuka, *Application of MO-type vacuum flange to beam duct for high current accelerators*, J. Vac. Sci. Technol. A23, 2005, p.1721, DOI:10.1116/1.2101808

[17] Y. Suetsugu, K. Kanazawa, K. Shibata, T. Ishibashi, H. Hisamatsu, M. Shirai, S. Terui, ?Results and problems in the construction phase of the SuperKEKB vacuum system?, J. Vac. Sci. Technol. A34, 2016, 021605, DOI:10.1116/1.4942455

[18] Y. Suetsugu, K. Kanazawa, K. Shibata, T. Ishibashi, H. Hisamatsu, M. Shirai, S. Terui, *Construction status of the SuperKEKB vacuum system*, Vacuum 121, 2015, 238?244, DOI:10.1016/j.vacuum.2014.12.010

[19] Y. Suetsugu, K. Shibata, T. Ishibashi, K. Kanazawa, M. Shirai, S. Terui, H. Hisamatsu, *First commissioning of the SuperKEKB vacuum system*, Phys. Rev. Accel. Beams 19, 2016, 121001, DOI:10.1103/PhysRevAccelBeams.19.121001

[20] M. Tobiyama, J.W. Flanagan, *Bunch by Bunch Feedback System for SuperKEKB Rings*, in Proceedings of the 13th Annual Meeting of Part. Accel. Society of Japan, 2016, p.144, https://www.pasj.jp/web_publish/pasj2016/proceedings/PDF/TUOM/TUOM06.pdf

[21] J.W. Flanagan, M. Arinaga, H. Fukuma, H. Ikeda, A. Lyndaker, D.P. Peterson, N. Rider, *High-power tests at CesrTA of X-ray optics elements for SuperKEKB*, in Proceedings of IBIC2013, 2013, p.844, https://jacow.org/ibic2013/papers/wepf15.pdf

[22] E. Luckwald, G. Bonvicini, D. Cinabro, *Measurement of colliding beam parameters with wide angle beamstrahlung*, Phys. Rev. E59, 1999, p.4584, DOI:10.1103/PhysRevE.59.4584

[23] Y. Funakoshi et al., *Interaction point orbit feedback system at SuperKEKB*, in Proceedings of IPAC2015, 2015, p.921, DOI:10.18429/JACoW- IPAC2015-MOPHA054

[24] *Experimental Physics and Industrial Control System*, https://epics.anl.gov/

[25] S. Sasaki, A. Akiyama, M. Iwasaki, T. Naito, T.T. Nakamura, *Upgrade of abort trigger system for SuperKEKB*, in Proceedings of ICALEPCS2015, 2015, p.417, DOI:10.18429/JACoW-ICALEPCS2015-MOPGF141

[26] C. La Licata on behalf of the BEAST II collaboration, *Radiation Monitoring with Diamond Sensors for the Belle-II Vertex Detector*, Proceedings of International Conference on Technology and Instrumentation in Particle Physics 2017. TIPP 2017. Springer Proceedings in Physics, vol 213. DOI:10.1007/978-981-13-1316-5_70

[27] L. Vitale et al., [Belle-II SVD Collaboration], *The Monitoring System of the Belle II Vertex Detector*, PoS Vertex 2016, 051 (2017). DOI:10.22323/1.287.0051

[28] T. Kageyama et al., *The ARES cavity for KEK B-factory*, EPAC 96, Conf. Proc. C 960610, 2008 (1996)

[29] T. Tajima et al., *The superconducting cavity system for KEKB*, Proceedings of the 1999 Particle Accelerator Conference, New York, 1999

[30] Y. Morita, K. Akai, T. Furuya, A. Kabe, S. Mitunobu, M. Nishiwaki, *Developments of horizontal high pressure rinsing for SuperKEKB SRF cavities*, in Proceedings of SRF2015, 2015, p.443, https://jacow.org/srf2015/papers/mopb116.pdf

[31] P. Collier, *Synchrotron phase space injection into LEP*, CERN-SL-95-50OP (June 1995)

[32] P.A.P. Nghiem, N. Chauvin, W. Simeoni, Jr. and D. Uriot, *Core-Halo Issues for a Very High Intensity Beams*, Laser and Particle Beams, 32(1), pp. 109-118. DOI:10.1017/S0263034613001055

[33] T. Trenkler, J. B. Jeanneret, *The principles of two stage betatron and momentum collimation in circular accelerators*, Particle Accelerators, 1995, Vol. 50, pp. 287-311

[34] M. Ferrario, M. Migliorati, L. Palumbo, *Wakefields and Instabilities in Linear Accelerators*, Accelerator Physics, arXiv:1601.05216, DOI:10.5170/CERN-2014-009.357

[35] *New Post-Linac Collimation System for the Next Linear Collider*, NLC Post-Linac Collimation Task Force, LCC-Note-0052, 21-Feb-2001

[36] X. E. Lin, D. H. Whittum, *Image Current Heating On Metal Surface Due To Charged Bunches*, SLAC-PUB-8393 (2000).

[37] Y. Suetsugu, T. Kageyama, K. Shibata, T. Sanami, *Latest movable mask system for KEKB*

[38] T. Ishibashi, S. Terui, Y. Suetsugu, *Low impedance movable collimators for SuperKEKB*

[39] The GdfidL Electromagnetic Field Simulator, http://www.gdfidl.de

[40] A. W. Chao, K. H. Mess, M. Tigner, F. Zimmermann, *Handbook of Accelerator Physics and Engineering*, World Scientific, 2012, pp. 263-265

[41] H. Wiedemann *Particle Accelerator Physics*, Springer-Verlag, 1993, pp 300-317, ISBN 3-540-56550-7

[42] A. Piwinski, *The Touschek effect in strong focusing storage rings*, DESY 98-179, 1998, arXiv:physics/9903034

[43] H. J. Bhabha, *The scattering of positrons by electrons with exchange on Dirac's theory of the positron*, 154, Proc. R. Soc. Lond. A, http://doi.org/10.1098/rspa.1936.0046

[44] S. Agostinelli et al., *GEANT4: A Simulation toolkit*, NIM, A506, 250?303 (2003), DOI:10.1016/S0168-9002(03)01368-8

[45] J. Allison et al., *Geant4 developments and applications*, IEEE Trans. Nucl. Sci., 53, 270 (2006), DOI:10.1109/TNS.2006.869826.

[46] Strategic Accelerator Design, http://acc-physics.kek.jp/SAD

[47] K.Hirata, *An introduction to SAD*, Second Advanced ICFA Beam Dynamics Workshop, CERN 88-04 (1988).

[48] T. Kuhr, C. Pulvermacher, M. Ritter, T. Hauth, N. Braun, *The Belle II Core Software*, Computing and Software for Big Science, 2018, DOI:10.1007/s41781-018-0017-9

[49] A. W. Chao, K. H. Mess, M. Tigner, F. Zimmermann, *Handbook of Accelerator Physics and Engineering*, World Scientific, 2012, pp. 266-267

[50] A. W. Chao, K. H. Mess, M. Tigner, F. Zimmermann, *Handbook of Accelerator Physics and Engineering*, World Scientific, 2012, p. 238

[51] W. Heitler, *The Quantum Theory of Radiation*, Clarendon Press, Oxford, 1960

[52] P.M. Lewis et al. *First measurements of beam backgrounds at SuperKEKB*, NIM, Volume 914, 2019, pp. 69-144, DOI:10.1016/j.nima.2018.05.071.